Mechanistic insights into nanobubble dynamics

ナグ, サルタック

https://hdl.handle.net/2324/4784609

出版情報：Kyushu University, 2021, 博士（工学）, 課程博士
バージョン：
権利関係：

Mechanistic Insights into Nanobubble Dynamics

Sarthak Nag

2022.01

九州大学

The work in this thesis was carried out at the Graduate School of Engineering of the Kyushu University. This work was financially supported by the Japan Society for the Promotion of Science (JSPS) Grants-in-Aid for Scientific Research (KAKENHI) program grant number JP20J13061 and the Japan Science and Technology Agency - Core Research for Evolutional Science and Technology (JST-CREST) project grant number JPMJCR18I1.

Title in Japanese Language:
ナノバブルの動的挙動に関する研究

Author’s Name in Japanese Language:
ナグ　サルタック

Graduate School of Engineering, Kyushu University,
744 Motooka, Nishi-ku, Fukuoka 819-0395, Japan

Mechanistic Insights into Nanobubble Dynamics

Sarthak Nag

Department of Mechanical Engineering
Graduate School of Engineering
Kyushu University, Japan

This dissertation is submitted to obtain the degree of

Doctor of Philosophy (Engineering)

博士 (工学)

January 2022

To my parents,
mumma ji and papa ji

Abstract

Nanobubbles are the nanoscale gaseous or vapor domains enclosed by liquid interface or liquid-solid interfaces. Recent advancements in nano-fabrication instrumentation capabilities have revealed behavioral oddities with bubbles and gas cavities at the nanoscale. Therefore, the present course of the research related to nanobubbles is to understand the fundamentals of their existence and physical characteristics, so that their application can be expanded to domains related to thermal management of electronics, efficient phase change, medical healthcare, and various others. Previously, several researchers have devoted efforts towards understanding the counterintuitive stability and longevity of surface nanobubbles. However, most of the existing studies do not reveal the dynamic behavior of the surface nanobubbles, and the gas transport at nanoscale.

Therefore, this thesis is focused on studying the dynamic behavior of surface nanobubbles by directly visualizing these nanoscopic species using in-situ liquid-phase electron microscopy. Liquid phase electron microscopy is a direct observation technique which allows the observation of the fluids with high spatial and temporal resolution. Thus far, the major understanding about surface nanobubbles and their behavior have been revealed using atomic force microscopy, which inherently has a low temporal resolution. The ability to directly visualize surface nanobubbles at real-time scales has the potential to reveal their dynamics and provides the opportunity to comprehend their oddities and other physical characteristics. Therefore, this thesis aims at augmenting the understanding of surface nanobubbles by adding the dynamic component.

The first study in this thesis focuses on gaining insights into the nanobubbles' behavior and their interfacial dynamics. Firstly, addressing the probabilistic nature of surface nanobubble nucleation in previously reported liquid phase electron microscopy experiments, a new methodology is devised which allows to nucleate nanobubbles in user defined size and number density bands. Next, an interacting nanobubbles' pair having radii less than 50 nm is studied which reveals the unique pull-push dynamics these nanobubbles undergo. Interestingly, freely growing-shrinking nanobubble and pinned nanobubble are observed at identical experimental conditions, suggesting the possibility of multiple nanobubble stabilization theories and pathways. The study also reveals that a freely growing-shrinking nanobubble induces anisotropic depinning in the three-phase contact line of a strongly pinned neighboring nanobubble.

In the second study, the focus is on the coalescence phenomenon in surface nanobubbles. The findings suggest that the merging of closely positioned surface nanobubbles is initiated by gradual localized changes in the physical properties of the region between the adjoining nanobubbles' interfaces. More precisely, the merging of the stable nanobubbles is initiated by the deposition of gas molecules and the formation of a thin gas layer. In addition, the merging of multiple surface nanobubbles and gas layer formation dynamics is also discussed in this study. Further, the kinetics of deposition and formation of the thin film is found to be majorly governed by the degree of oversaturation in the liquid.

At last, as a demonstration of surface nanobubbles' functionality, a novel methodology to fabricate soft line features from surface nanobubbles is illustrated. The highly focused electron beam from the TEM is used to generate localized oversaturation in the liquid film whereas the TEM's trackball is used to facilitate sample-electron beam relative motion. The features of nanobubbles having width less than 300 nm are achieved using this methodology, which are proposed to have applications in bubble-assisted nanofabrication techniques. The results also reveal the stability of nanobubble patterns, both temporally and in flow.

Overall, the studies included in this thesis will potentially pave the way for a better understanding of nanobubbles and gas transport phenomenon at nanoscale.

Contents

ABSTRACT .... **I**

CONTENTS .... **III**

NOMENCLATURE .... **V**

CHAPTER 1 INTRODUCTION **1**

1.1 NANOFLUIDICS 3
  1.1.1 Nanobubbles *4*
1.2 SURFACE NANOBUBBLES 7
  1.2.1 Introduction and historical overview *7*
  1.2.2 Tools for characterizing surface nanobubbles *9*
  1.2.3 Liquid-phase electron microscopy *13*
  1.2.4 Nanobubbles dynamics *17*
  1.2.5 Applications of nanobubbles *22*
1.3 RESEARCH OBJECTIVES 26
1.4 OUTLINE AND SCOPE OF THESIS 26

CHAPTER 2 NANOBUBBLES AND THEIR RELATED INTERPLAY **29**

2.1 BACKGROUND 30
2.2 EXPERIMENTAL METHODS AND PROCEDURES 32
  2.2.1 Experimental equipment *32*
  2.2.2 Imaging and analysis *34*
2.3 RESULTS AND DISCUSSIONS 36
  2.3.1 Nanobubble nucleation strategy *36*
  2.3.2 Experimental observation *39*
  2.3.3 Anisotropic depinning in nanobubbles *46*
  2.3.4 Weakened repulsions and coalescence *50*
2.4 SUMMARY 53

CHAPTER 3 NANOBUBBLE COALESCENCE **55**

3.1 BACKGROUND 56
3.2 EXPERIMENTAL EQUIPMENT AND METHODS 57
  3.2.1 Experimental equipment *57*
  3.2.2 Imaging and analysis *59*
3.3 RESULTS AND DISCUSSIONS 60
  3.3.1 Nanobubble observation in liquid cell *60*
  3.3.2 Insights on varying intensity between the bubbles *63*

3.3.3 Proposed mechanism for the formation of the thin gas layer 67
3.3.4 Effect of gas saturation on gas-layer initiated merging 69
3.3.5 Evolution of multiple merging nanobubbles 70
3.4 SUMMARY 72

CHAPTER 4 NANOBUBBLE PATTERNING 75

4.1 BACKGROUND 76
4.2 EXPERIMENTAL EQUIPMENT 78
4.3 RESULTS AND DISCUSSIONS 78
4.3.1 Nucleation and pattern formation 78
4.3.2 Patterning capability 80
4.3.3 Stability of nanobubble patterns 81
4.3.4 Proposed applications 83
4.4 SUMMARY 84

CHAPTER 5 CONCLUSIONS AND OUTLOOK 87

5.1 CONCLUSIONS 88
5.2 FUTURE RESEARCH DIRECTIONS 89
5.2.1 Immediate research direction 89
5.2.2 Additional recommendations 90

LIST OF FIGURES 91

LIST OF TABLES 99

SUPPLEMENTARY INFORMATION 101

BIBLIOGRAPHY 113

ACKNOWLEDGEMENT 125

Nomenclature

Acronyms

AFM	*atomic force microscope*
e-beam	*electron beam*
e-chip	*environmental chip*
EDL	*electric double layer*
CA	*contact angle*
CNT	*carbon nanotube*
fps	*frames per second*
GLC	*graphene liquid cell*
IQR	*interquartile range*
LPEM	*liquid-phase electron microscopy*
MD	*molecular dynamics*
nb	*nanobubble*
OM	*optical microscopy*
SEM	*scanning electron microscope*
SiN_x	*silicon nitride*
SiN_x-LC	*silicon nitride liquid cell*
S/N	*signal to noise*
STM	*scanning tunneling microscope*
STXM	*scanning transmission X-ray microscopy*
TEM	*transmission electron microscope*
vdW	*van der Waals*

Physical quantities*

A	*area*	m^2
atm	*atmospheric pressure*	Pa

c	*gas concentration*	kg/m^3 *of solution*
h	*height*	m
L	*lateral extension*	m
P	*perimeter*	m
r	*radius*	m
s	*supersaturation ratio*	—
t	*time*	s
σ	*standard deviation*	—
ρ	*density*	kg/m^3
θ	*contact angle*	*degrees*
ϑ	*sensitivity threshold*	—
ζ	*oversaturation*	—
γ	*surface tension*	N/m
$\varnothing$	*diameter*	m
φ	*ionic concentration*	M

**SI Units*

— = *dimensionless*

Subscripts

c	*critical*
e	*equilibrium*
g	*gas*
s	*solubility*
0	*initial*
∞	*far field*
$+$	*spinodal*

1

Introduction

"Order arise from chaos."

Ilya Prigogine
The Nobel Prize in Chemistry 1977

"There is Plenty of Room at the Bottom" [1]

Although pinpointing the precise roots of nanotechnology is still debatable, *Richard Feynman* in his famous talk at the dinner of the annual meeting of the American Physical Society held at the California Institute of Technology in 1959, gave an idea of manipulating and controlling the events on a very small scale, and practically miniaturing the size. In the same talk, he discussed the miniaturization of electronic circuits: having wires 10-100 atoms in diameter or circuits just a few angstroms wide. He even forecasted the amazing opportunities and domains going "small" would create. However, the true realization of his ideas and the development in nanotechnology began in the early 1980s when the researchers from IBM *Gerd Binnig* and *Heinrich Rohrer* invented Scanning Tunneling Microscope *(STM)* which helped in imaging atoms and molecules. They even won the 1986 Nobel Prize in Physics for this invention, sharing it with *Ernst Ruska*: the pioneering researcher who first developed electron optics and electron microscopy in 1931. The citation of their Nobel Prize read as:[2]

The Nobel Prize in Physics 1986 was divided, one half awarded to Ernst Ruska "for his fundamental work in electron optics, and for the design of the first electron microscope", the other half jointly to Gerd Binnig and Heinrich Rohrer "for their design of the scanning tunneling microscope."

Surprisingly, it took nearly 55 years to recognize the impact which direct observation at the nanoscale using transmission electron microscope (TEM) would create. Long story short: researchers and the world began to realize the importance of manipulating atoms and molecules and controlling their behavior for numerous prospective applications. Fast forward to 2021 and the world is experiencing a rapid pace in technological advancements and innovations, and the capabilities, which were once a distant dream, are now possible and can be realized with much simpler approach. The domain of *nanotechnology* is going through unprecedented advancements and is contributing massively towards the health sector, water purification, photovoltaics, sustainable energy, nano transistors, nano-functionalized nutrition, coating materials: thermal control and stealth, and numerous more. The researchers merely required less than 6 months to nanoengineer mRNA-based vaccines for the ongoing Covid-19 pandemic whose socio-economic benefit is beyond any numbers is an excellent example of the progress and possibilities in the domain of nanotechnology. At the same time, we hear advancements in nanofabrication where IBM has developed a 2 nm node (~ 6 atoms) on a 300 mm wafer for the next-generation electronics. All these advancements fuel the human curiosity to look deeper into the matter for exotic applications fruitful for improving the fundamental quality of human life. In addition, the much unexpected non-classical behavior of matter at nanoscales, and the enhanced functionalities of the interfaces (higher surface area to volume ratio) has fascinated the researchers to look for the key behavior and fundamentals that will be decisive in controlling or manipulating the much larger phenomenon while looking deeper into the small scales and for creating new avenues in science and technology.

1.1 Nanofluidics

Nanofluidics is the extension of the study of fluidics down to nanometer scale, however, for distinction and clarity, the fluidic phenomenon having a typical characteristic dimension of 100 nm or less is considered in the classical nanofluidics. The typical length scales of interactions at the nanoscale are shown in **Figure 1.1**(A).[3] In comparison to the much read and understood domain of solid-state physics, nanofluidics is mostly an "*unrealized but developing*" domain as much of its progress have been in the past decade or so.[4] As a fact, it is so new that even the popular word processing software considers

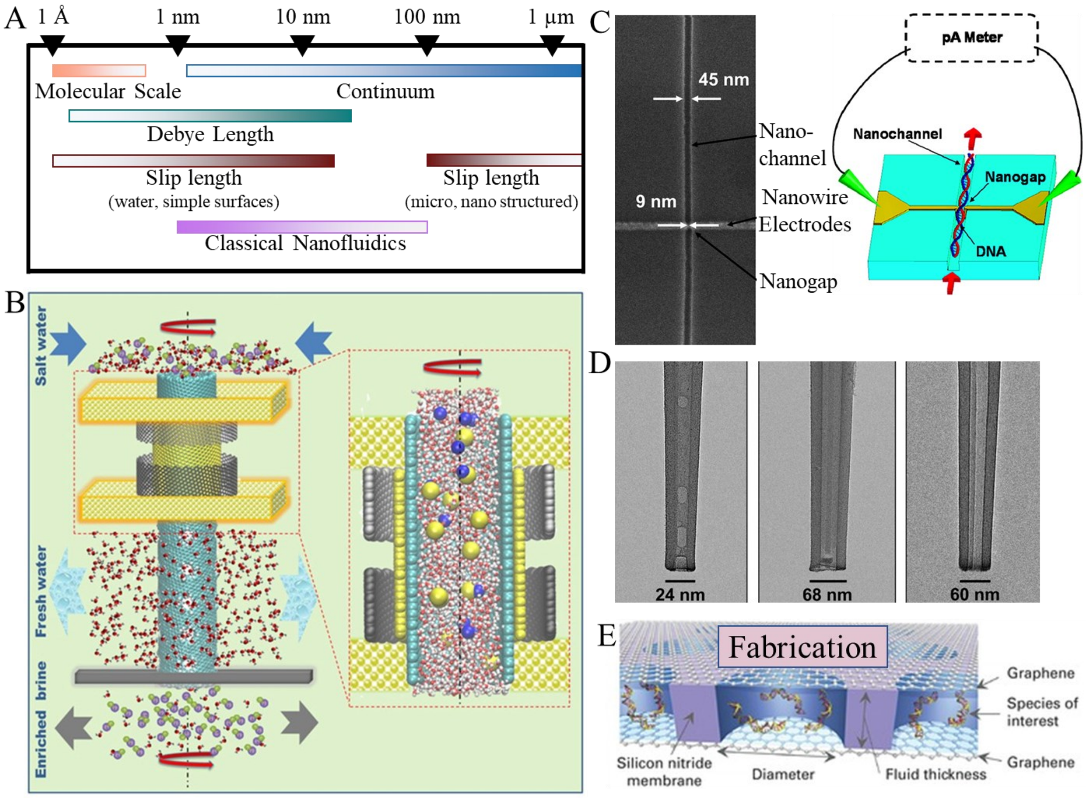

Figure 1.1 Nanofluidics. (A) Various length scales at play in nanofluidics. Image adapted from [3] Copyright © Royal Society of Chemistry. (B) Illustration of the design concept of the rotating CNT membrane filter and its desalination mechanism. Image adapted from [6] Copyright © Nature. (C) Top view of a nanogap detector without top sealing plate along with the schematic for DNA detector. Image adapted from [7] Copyright © American Chemical Society. (D) Nanobubble-plugged nanopipette, nanobubble-free nanopipette, and air-filled nanopipette. Image adapted from [8] Copyright © Science. (E) Fabrication of 2nd generation graphene liquid cell (GLC) for nanoscale experiments. Image adapted from [9] Copyright © Cambridge university press.

the word *"nanofluidics"* as misspelled. Due to the length scales comparable to the dimensions of the atoms, and the dominating surface effects ($\propto l^2/l^3$), nanofluidics is a rich domain in terms of forces acting at nanometer scales, as it is the convolution of electrostatic effects (*Debye length*), mingled with the molecular mean free paths, critical nucleation radii of species, thermal capillary effects, and many more surface effects acting at the nanoscale.[5]

The fact which has led to the emergence of the nanofluidics domain in the last decade or so is the advancements in fabrication technology coupled with enhanced instrumentation capabilities and the fluidic oddities at the nanoscale observed in the early experiments. The capability to fabricate tailored low dimensional materials such as nanopores, 1-D nanotubes, 2-D materials, nanoscale heterogeneous structures, 2-D slits, etc. has been instrumental in encapsulating nanoscale fluids to study the nanofluidics. Moreover, the gained capabilities in the photolithography process for fabricating nanometer-scale flow channels, or the thin-film deposition methods, etc. along with the visualization techniques, such as super-resolution imaging or direct observation of nanoscale phenomenon has helped in realizing the *exotic* fluid phenomenon at the nanoscale. Intriguingly, such discoveries have unveiled several anomalies, such as ultrafast transport in carbon channels (*The bizarre water-carbon couple*),[4] or low dielectric constant of confined water, or size effects in ionic transport (*selective transport*), etc. which has brought in a series of disruptive technologies for ionic filtration (**Figure 1.1**(B)),[6] DNA sequencing **Figure 1.1**(C),[7] energy conversion, solving water-energy nexus, multiphase fluid (**Figure 1.1**(D)),[8] ion-selective ultrafast fluid transport, point-of-care applications, and phase-change. However, despite the popularity and recent developments in fabrication capabilities (**Figure 1.1**(E)),[9] there is a huge scope to understand its fundamentals and propose applications that require specialized fabrication techniques, advanced instrumentation, and elaborative studies.

1.1.1 Nanobubbles

In simplistic terms, a bubble is defined as a gaseous or vapor (*or a mixture of both*) domain enclosed by a liquid interface. They hold importance in major industrial operations: electricity generation in thermal plants, manufacturing and production industry, food processing industry, thermal management of electronics, and many more. Bubbles have always been thermodynamically unstable as their formation demands the creation of an interface whose energy cost is given by the surface tension.[10] Bubbles are also unstable for their size. When the gas inside the bubble is in equilibrium with the gas dissolved in the liquid, the bubbles are expected to maintain their size. However, this condition is usually impossible to meet due to the enormous Laplace pressure of bubbles. For a bubble having a 1 mm radius, the excess Laplace pressure is mere 0.0014 atm, but as the size of the bubble reduces to, let's say, 1 μm, the excess pressure inside a small bubble should be ~1.5 atm, which is substantially high. This will, or rather should render a very short life to the small-scale bubbles. *Paul Epstein*

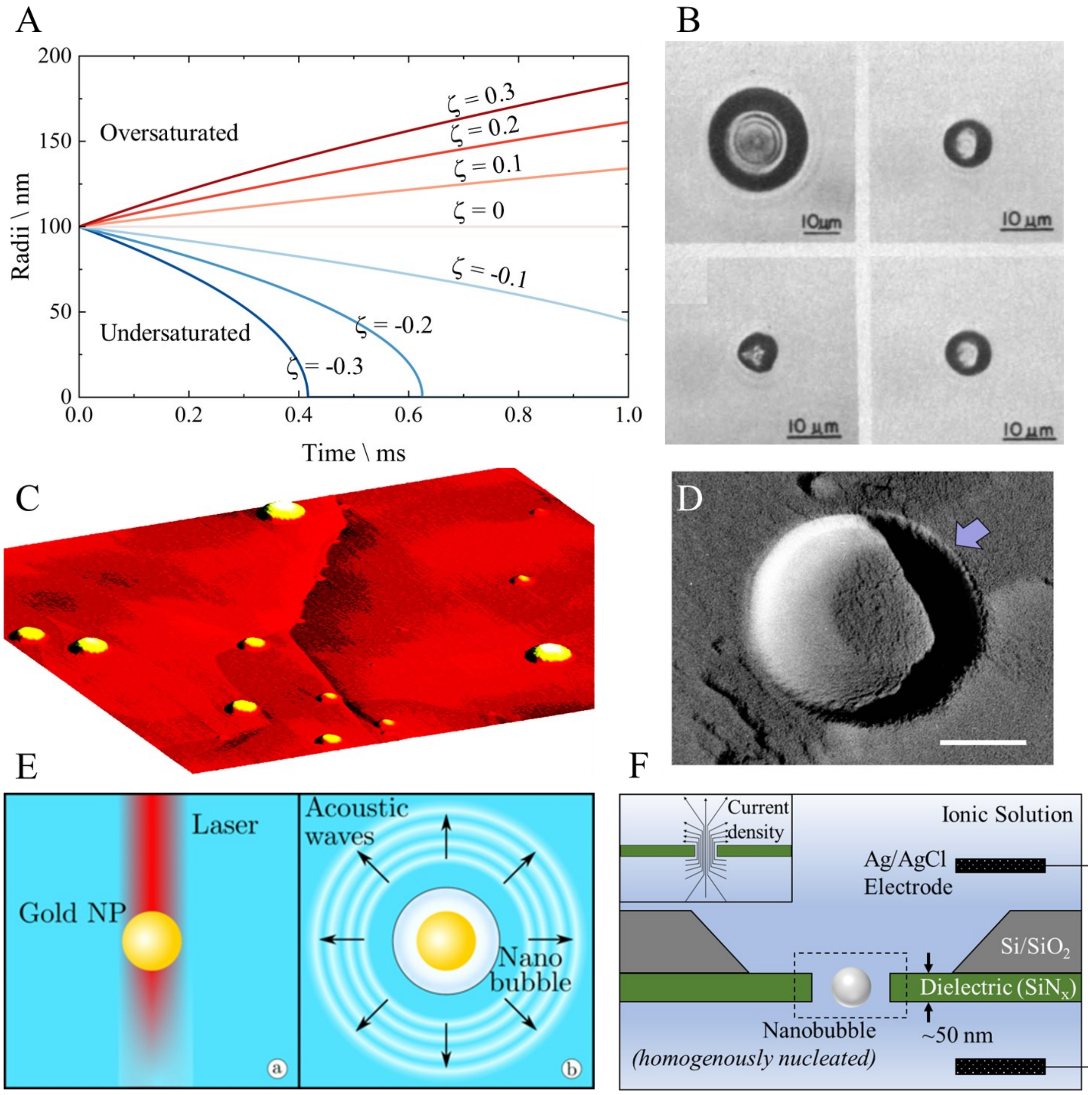

Figure 1.2 (A) Behaviour of the 100 nm air bubble in water at various oversaturation (ζ) conditions, using Epstein-Plesset formulation.[11] (B) Bubbles formed in sea water stable for 22 hours. Image adapted from [13] Copyright © Science. (C) Surface gas nanobubbles. Image scale: 2 μm × 2 μm × 40 nm. Image adapted from [18] Copyright © American Physical Society. (D) Bulk nanobubble imaged using TEM freeze fracture replica method. Scale bar 100 nm. Image adapted from [17] Copyright © MDPI. (E) Illustration for the generation a transient vapor plasmonic nanobubble. Image adapted from [16] Copyright © American Physical Society. (F) Vapor nanobubble nucleated in a nanopore using Joule's heating.

and *Milton Plesset* gave the mathematical relation for the expansion and dissolution of the bubbles in liquid via diffusion, i.e., bubble growth in an oversaturated solution and bubble dissolving in an undersaturated solution.[11] If the same mathematical expression is applied to an air bubble in water having an initial radius of 100 nm, it would either shrink or grow depending on the oversaturation condition, as shown in **Figure 1.2**(A), and it would be impossible for bubbles of this size to exist or be stable. Yet, stable bubbles smaller than 1 µm have been observed experimentally and are known *as nanobubbles*. This is where the curiosity towards such nanoscopic gaseous domains began.

Nanobubbles are the nanoscale gaseous domains or cavities, found either in the bulk liquid or at the liquid-solid interface. Fundamentally, they should not exist owing to the abnormally high internal pressure and short lifetimes. Despite that, nanobubbles have been observed to be stable for days in the past. The very first evidence of the bubbles having a size less than 1 µm was found in fossilized form, coated with organic matter in the East African Rift Lake: *Kivu*, first reported in 1973.[12] It was proposed that such coated spheres may be significant in the development of early life.[10,12] Later, in 1981, researchers from *Dalhousie University Canada* demonstrated bulk bubbles of size less than 1 µm in seawater, stabilized by the presence of physically absorbed substances, as shown in **Figure 1.2**(B).[13] They also found that the bubbles were responsive to the small negative and positive changes in pressure and demonstrated their longevity for up to 22 hours. These works were probably the first ones to observe nanobubbles, although nowhere did they use the word "nanobubbles". Since then, hundreds of works reported the existence of nanobubbles, even though their presence has been highly debated.

Nanobubbles can be distinguished based on their constituents: gas or vapor; or on basis of their position of existence: in bulk or at the surface; or in the combination of both distinguishing factors. Therefore, there have been gas nanobubbles: both surface (**Figure 1.2**(C)) and bulk (**Figure 1.2**(D)); and vapor nanobubbles: both surface and bulk. Vapor nanobubbles, in general, are transient and usually exist in ns time scales, which makes their direct observation impossible with the current visualization capability. Vapor nanobubbles are formed transiently in a superheated environment and are proposed to have applications in harnessing solar energy, two-phase cooling, energy conversion, etc. As put forward by Thome and coworkers[14] and conceptualized by Paul and coworkers,[15] the vapor nanobubble could be used in the two-phase cooling of next-generation nanoscale transistors. However, due to the short-lived nature of such bubbles, it has been impossible to understand the dynamic nature of such bubbles from the application point of view by observing them directly. Mostly, researchers have been using plasmonic nanoparticles excited by lasers (**Figure 1.2**(E)) and joule's heating technique (**Figure 1.2**(F)) to nucleate such transient bubbles,[16] and pulse sensing techniques[15] to observe and study such transient nanobubbles. On the other hand, gas bubbles, both bulk[17] and surface[18], possess high longevity which makes them favorable to be observed "directly" using numerous visualization techniques. They also possess high functionalities such as nanoscale surface cleaning capability, water purification, nucleate boiling, etc. which makes it worthwhile to study their behavior, but more importantly, these can also be used to understand the gas phase behavior at the nanoscale which can be extrapolated to understand the dynamics of all nanobubbles, vapor or gas, in general.

1.2 Surface Nanobubbles

1.2.1 Introduction and historical overview

Surface nanobubbles, also known as interfacial bubbles, are the nanoscale gaseous domains present at the liquid-surface interfaces, having a size in the order of 1-100 nm. They have attracted attention from the researchers because their long life is up to 9-10 orders of magnitude longer than predicted, which challenges the existing understanding of bubbles' stability. Moreover, nanobubbles exhibit very low contact angles (measured from the gas side) due to the line tension and modification of Young's equation, which is in contrast to the contact angles exhibited by the solid-gas pair at the macroscale. Amazingly, the nanobubbles are even stable in aqueous solutions and do not get affected by the pH changes of their nucleating liquid. Owing to the unresolved questions and mystery on their existence and stability, the past three decades have seen extensive research about surface nanobubbles. **Figure 1.3**(A) gives the recap of the few major events in the field of surface nanobubbles that has helped in the understanding of their existence and characteristics. The initial speculations on the existence of surface nanobubbles were made by *Parker*, *Claesson*, and *Attard* in 1994 as an explanation for the strong attractive forces beyond the effect of electrostatic or dispersion forces.[10,19,20] They measured the force as a function of separation between two hydrophobic surfaces and observed various jumps in the force magnitude as shown in **Figure 1.3**(B), which they hypothesized to be due to the bridging nanobubbles when two surfaces are brought together. This was followed by some criticism and questioned due to the Laplace pressure bubble catastrophe, which would render under-a-second lifetime to such nanoscale gaseous domains.[21]

However, six years after the initial claims, the first images of the nanobubbles were captured by the *Japanese* researchers using atomic force microscope (AFM),[22] as shown in **Figure 1.3**(C), which suggested the clear relationship between the existence of nanobubbles and long-range hydrophobic attractive forces.[10,22] The nanobubbles were later observed to be long-lived, super-stable even at extreme negative pressures, exhibit contact angles unique to the microscopic scale, and indifferent to any changes in salt type or pH of the nucleating medium.[23,24] Since, the existence of the surface nanobubbles was confirmed now, next came the attempts to purpose the mechanisms imparting stability to nanobubbles.[25] Various stabilization theories were proposed by researchers; some popular ones being the dynamic equilibrium theory (2008),[26,27] the contamination theory (2009),[28] and the contact line pinning (2013).[29,30] Brief revisit to these theories suggests that the contamination theory claimed that the omnipresent layers of contamination at the liquid-gas interface reduces the bubble's internal pressure, thus reducing the gas diffusing out of

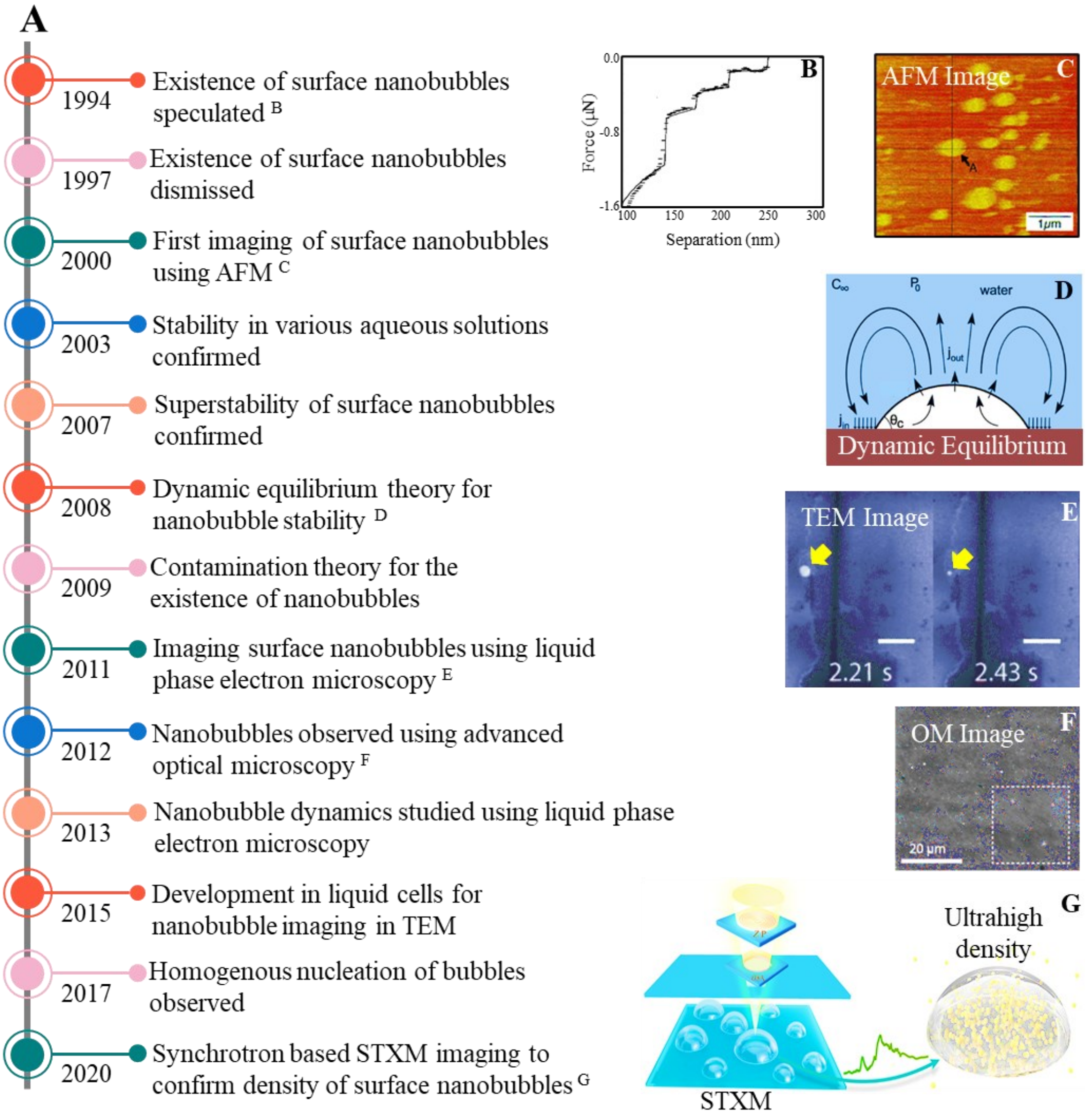

Figure 1.3 (A) Timeline of the major events in the surface nanobubbles' research. (B) The first speculation of surface nanobubbles in 1994 due to step-like features in the force-separation curve measured between two hydrophobic surfaces. Image adapted from [20] Copyright © American Chemical Society. (C) One of the first image of surface nanobubbles acquired using AFM. Image adapted from [22,39] Copyright © American Chemical Society. (D) Dynamic equilibrium theories: one of the earlier theories used to define the stability of nanobubbles. Image adapted from [26] Copyright © American Physical Society. (E) Image of a collapsing nanobubbles using in-situ liquid phase electron microscopy. Image adapted from [31] Copyright © IOP Science. (F) TIRF-Optical microscope applied to observe surface nanobubbles of radius 135 nm and above. Image adapted from [33] Copyright © American Physical Society. (G) Synchrotron based STXM systems used to understand the density of surface nanobubbles. Image adapted from [38] Copyright © American Chemical Society.

the bubble and imparting stability to surface nanobubbles. The dynamic equilibrium theory suggested that the presence of continuous equilibrium between the influx and outflux across the liquid-gas interface, as shown in **Figure 1.3**(D), whereas the contact line pinning theory suggested that the nanobubble's contact line is strongly pinned due to omnipresent heterogeneities present at the solid surface which is responsible for nanobubble stability.

The development of imaging techniques followed which not only provided alternatives to AFM imaging but also made the characterization of bubbles straightforward. With the advancement in nanofabrication techniques, TEM, for the first time was utilized to observe the growth and collapse of vapor nanobubble with unprecedented spatial and temporal resolutions applied for nanobubble observation at that time, as shown in **Figure 1.3**(E).[31] At the same time, "advanced" forms of optical microscopy, such as total internal reflection fluorescence (TIRF) imaging, was also able to confirm the existence of nanobubbles in the absence of undulations caused by AFM tip or electron beam effects as shown in **Figure 1.3**(G), although the spatial resolutions achieved were far inferior to that of TEM or AFM.[32,33] The studies concerning the dynamics of nanobubbles using in-situ liquid-phase electron microscopy soon followed, using both the silicon nitride liquid cells (SiN_x-LCs) and graphene liquid cells (GLCs). The studies so far have showcased the capability of in-situ liquid-phase electron microscopy in delineating the dynamics of nanobubbles such as Ostwald ripening,[34] diffusive shieldings,[35] gas transport between bubbles,[36] ultrafast gas transport,[37], etc. More recently, researchers studied the properties of the gas phase in the nanobubbles using synchrotron-based scanning transmission X-ray microscopy (STXM) systems and found the existence of a very dense gas state, instead of ideal gas.[38]

1.2.2 Tools for characterizing surface nanobubbles

The observation of surface nanobubbles requires advanced instrumentation and fabrication techniques to visualize them and anticipate their characteristics. AFM was used to capture the first image of surface nanobubbles,[22,39] and so far, has been the most popular instrument to characterize nanobubbles. In the meantime, other tools such as TEM, SEM, optical microscope, and other spectroscopy techniques have also gained popularity for the imaging of nanobubbles.

AFM raster scans the topography of the surface with atomic resolutions, using a tip having angstrom scale cone tip diameter positioned at one end of a cantilever and the deflections in the cantilever gives the measure of the surface topography.[40] **Figure 1.4**(A) shows the schematic diagram for imaging nanobubbles using AFM.[41] It can provide atomic-scale resolutions even in a liquid environment which comes in very handy to capture surface nanobubbles. Moreover, since it is a scanning probe technique, it can provide the three-dimensional topography of the surface nanobubbles, which no other

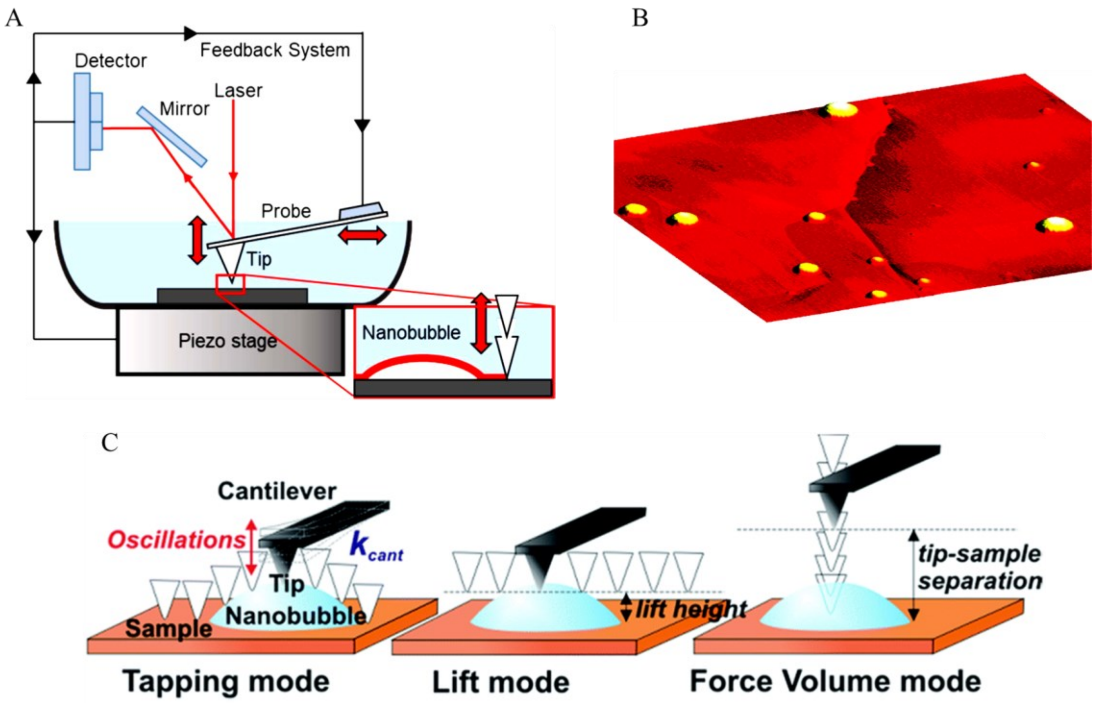

Figure 1.4 Characterising nanobubbles using AFM. (A) Schematic for the imaging of nanobubbles using AFM. Image adapted from [41]. (B) AFM image of the surface nanobubbles captured on HOPG substrate. Image scale 2 µm × 2 µm × 40 nm. Image adapted from [18] Copyright © American Chemical Society. (C) AFM-tip nanobubble interaction leading to ambiguous characterisation at different operating modes of AFM. Images adapted from [44] Copyright © Royal Society of Chemistry.

instrument is capable of.[42] **Figure 1.4**(B) shows the representative image of nanobubbles acquired on the highly oriented pyrolytic graphite (HOPG) substrate using AFM.[18] AFM can be used in different modes to study the topography of surface nanobubbles: contact mode, tapping mode, and non-contact mode: frequency modulation mode and amplitude modulation mode are some of them. For nanobubbles, tapping mode and non-contact mode are the most popular imaging mode because of their reduced lateral forces which are advantageous for imaging soft matter. In general, the nanobubbles are nucleated on a hydrophobic surface by using the popular solvent exchange method. AFM has helped a lot in understanding the intrinsic characteristics of the nanobubbles, such as, their contact angles, 3-D profiles, as well as their longevity, in-fact, most of the pioneering studies on the subject of surface nanobubbles has been carried using the AFM, and therefore much of the theories are based on the results from the AFM.[43] However, the AFM tip-nanobubble interactions may sometimes lead to ambiguous characteristics of the nanobubbles, depending on the surface characteristics of the AFM tip as well as the operation mode used for imaging, as depicted in **Figure 1.4**(C).[43,44]

Additionally, AFM has a temporal resolution on the scale of a few tens of seconds, which does not reveal the dynamic characteristics of the nanobubbles.

Optical microscopy (OM), or advanced forms of optical microscopy, is another tool for observing nanobubbles.[23,32,33] There were several speculations about surface nanobubbles being nucleated due to the perturbations caused by the AFM tip, which were settled by the OM imaging of surface nanobubbles nucleated using the solvent exchange method. The advantage of using OM is its non-intrusiveness and high temporal resolutions. It is, however, limited by the spatial resolution and its inability to capture the three-dimensional

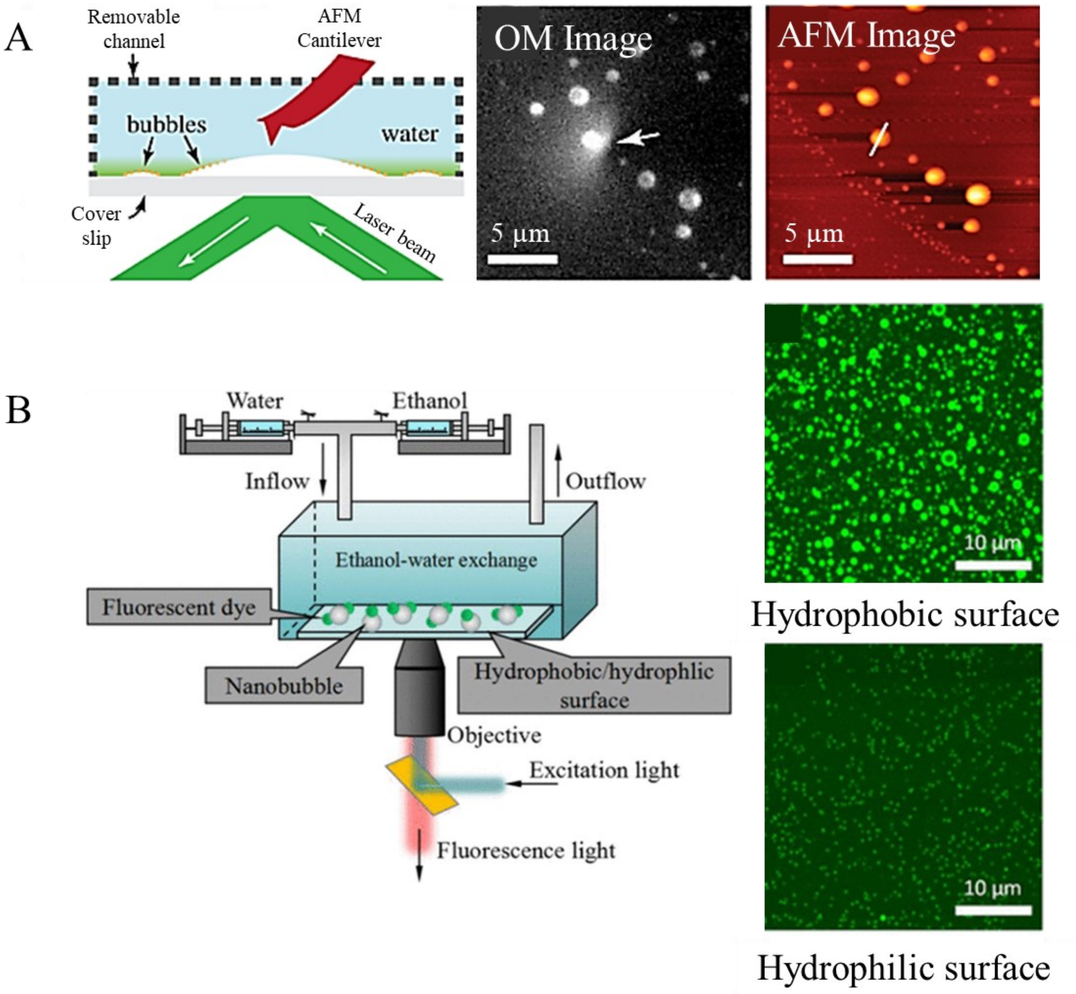

Figure 1.5 Optical microscopy of nanobubbles. (A) Simultaneous microscopy (AFM+OM) of nanobubbles nucleated by solvent exchange within a removable channel, along with the OM image and AFM image of the same feature. Images adapted from [46] Copyright © American Physical Society. (B) Setup for the laser scanning confocal microscopy and the nanobubbles observed at the hydrophilic and hydrophobic surfaces nucleated using ethanol-water exchange method. Images adapted from [45] Copyright © American Chemical Society.

topography. To overcome its spatial resolution limit, various advanced forms of OM such as interference enhanced reflection microscopy,[32] attenuated total internal reflection microscopy,[33] high-resolution fluorescence microscopy, laser scanning confocal microscopy,[45] etc. are being used to characterize nanobubbles. A recent conjugation of AFM with optical microscopy, as shown in **Figure 1.5**(A), is promising as the probe can be used to manipulate the nanobubbles whose dynamics can be captured in real-time using advanced optical microscopy.[46] **Figure 1.5**(B) shows the schematic for the laser scanning confocal microscopy used to capture surface nanobubbles nucleated using the ethanol-water exchange method on the hydrophobic and hydrophilic surface, which is hardly confirmed using the AFM.[45] However, the minimum size of the nanobubbles captured using these OM techniques remains above 100 nm.

Scanning transmission X-ray microscopy (STXM), a more exotic experimentation technique using synchrotron-based facilities for studying the surface nanobubbles provides spatial resolution better than the OM. However, the most important characteristic which STXM is capable of revealing is the properties of gas-phase present inside the nanobubble. This capability was first revealed in 2013 when the researchers using STXM observed stable nanobubbles of SF$_6$ and Ne.[47] **Figure 1.6**(A) shows the schematic diagram of the STXM system along with the SF$_6$ nanobubbles nucleated on the SiN$_x$ membrane.[47] Later in 2020, the same research group was able to confirm the

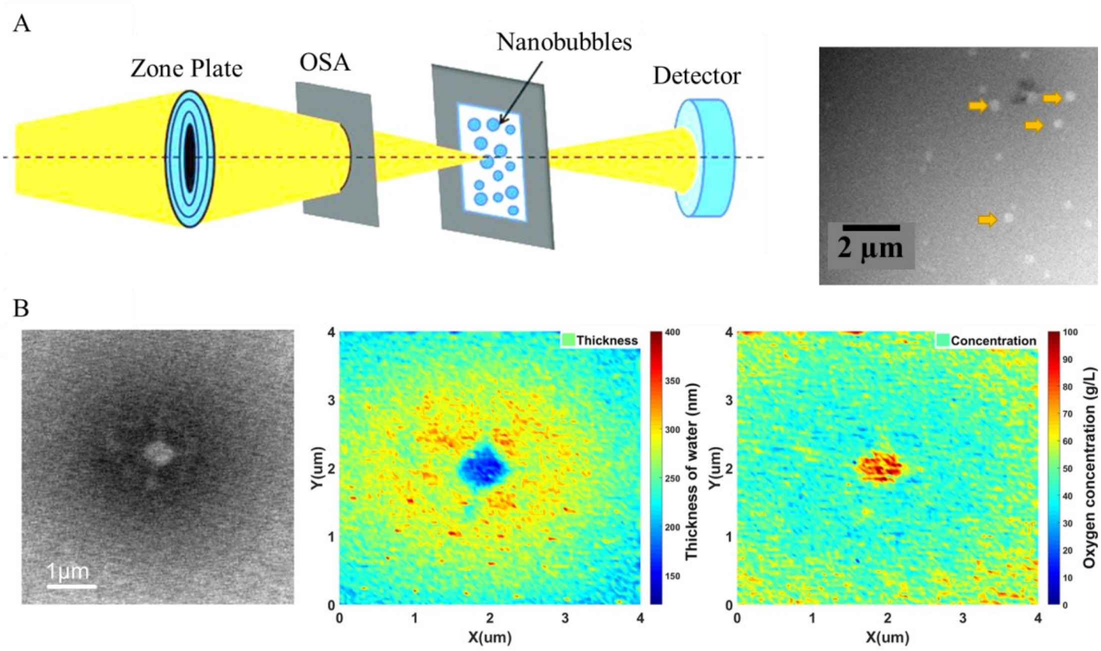

Figure 1.6 STXM imaging of surface nanobubbles. (A) Schematic of the configuration of zone-plate-based STXM, and the SF6 nanobubbles imaged using it. Image adapted from [47] Copyright © International Union of Crystallography. (B) Oxygen oversaturation in water and the gas concentration distribution map at 540 eV. Image adapted from [38] Copyright © American Chemical Society.

presence of condensed gas phase inside nanobubbles with density in the range of 100-250 kg/m^3, which is at least 100 times higher than the oxygen gas at 1 bar and 300 K.[38] **Figure 1.6**(B) shows the oxygen oversaturation in water and the gas concentration distribution map at 540 eV. Although this was qualitatively revealed in one of the AFM studies,[48] of the STXM results provided a concrete quantitative experimental verification of the existence of such a phase. Moreover, the STXM also revealed that the existence of nanobubbles at extreme oversaturation is a universal phenomenon, irrespective of the gas type. In another study, the STXM provided direct proof of the presence of a stable cloud of oxygen around a diatomite particle, thus reassuring the existence of interfacial nanobubbles.[49]

Liquid phase electron microscopy is another technique to study the surface nanobubbles dynamics, which provides the highest temporal and spatial resolutions for observing nanobubbles. A detailed explanation of this technique is given in the following section: **Liquid-phase electron microscopy**.

1.2.3 Liquid-phase electron microscopy

Since the first electron microscope was ever built, researchers were particularly interested to observe the wet samples for biological applications or material science with high spatial resolution.[50,51] Although the successive improvements in the environmental chambers at that time facilitated the observation of wet samples,[52] the spatial resolution was only marginally better than optical microscopes. A few decades ahead, the development and advancements in thin-film technology and nanofabrication have reinstated the researchers' interest to observe and control the phenomenon at molecular and atomic levels, such as the evolution of crystals at nanoscales,[53] self-assembly of nanoparticles,[54] liquid-solid interactions,[55] chemical reactions,[56] and many more. For example, the latest fabrication techniques provide so much control over the phenomenon that it is even possible to observe, in-situ crystal nucleation of NaCl from the parent solution, via the self-organization of atoms, and its lattice with an astonishing precision of 1Å using a solution encapsulated in a vibrating conical CNT.[57]

Conventionally, the observation of liquids (having high vapor pressure) in TEM is impossible in the standard configuration. Electrons, the illumination source, have a very short wavelength, and they lose their kinetic energy due to multiple collisions with the gas molecules while traveling through the ambient. Therefore, ultra-high vacuum in the TEM column is necessary, which renders incompatibility to the liquids for their direct observation in the TEM.[51,58] Hence, liquids are required to be embedded inside solid structures or casings, which serve the purpose of acting as a physical barrier between the TEM vacuum column and the specimen. However, for the sake of high spatial resolution, the solid used to encapsulate liquids must be atomically thin to facilitate the transmission of electrons without absorbing much of their energy. This is where the advancement in nanofabrication and thin-film technology has helped the development of liquid cells. The ease with which thin membranes, made either from graphitic materials or SiO_x or SiN_x, can be fabricated or deposited on the base substrate materials have allowed facile methods to encapsulate liquids at pressures much higher[59] than the vacuum column.

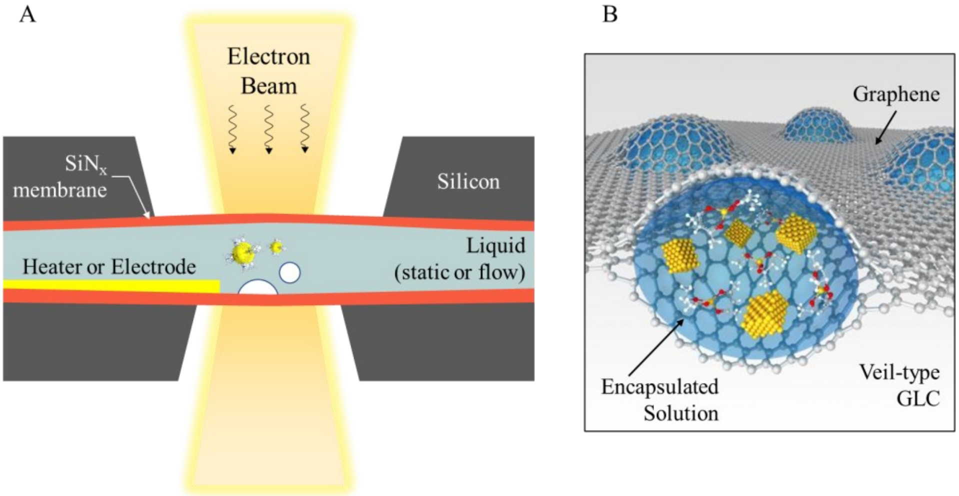

Figure 1.7 Schematic representation of (A) SiNx-LC, and (B) GLC. SiNx-LC offers better control over the liquid thickness and offers the possibility to accommodate MEMS devices, such as electrodes or heaters. GLC, on the other hand, offer higher spatial resolution. Image adapted from [61] Copyright © Royal Society of Chemistry.

Liquid phase electron microscopy is now seen as a powerful technique allowing the high spatial and temporal resolution imaging of dynamic phenomenon in liquids.[60] **Figure 1.7** shows the schematic of the two most common types of liquid cells used in the LPEM domain. The difference between these liquid cells is the type of membrane materials: graphene and SiN_x. The graphene liquid cells (GLCs), due to the atomic level thickness of graphene provide the highest spatial resolution for imaging,[61][62] however, lacks control on the liquid film thickness. Moreover, it is nearly impossible to allow flow through the GLCs or refill the GLCs during the experiments in case of drying or leakages. GLCs are also more susceptible to damages caused by the electron beams and are generally functional for observations lasting shorter durations, usually lasting a few minutes. On the other hand, SiN_x-LCs provide better control over the liquid film thickness as the spacer height between the SiN_x membranes can be customized as per the experimental demands. The reason for their popularity is the ease with which these liquid cells can be fabricated due to advancing fabrication methodologies, their homogenous thickness, and robust design. Moreover, it has other advantages over GLCs, such as it allows the flow of liquids, integration of MEMS devices such as electrodes or heaters etc., which increases the functionality and scope of experimental capabilities. Due to the higher thickness (~10^1 nm) of the SiN_x membrane, the susceptibility to damage due to the electron beam is generally low and the specimen can be observed for long durations. Moreover, the pressure inside the SiN_x-LCs can be controlled, thus facilitating better controllability over the specimen and the investigated processes, which is the case of GLCs is speculated to be very high due to the strong van der Waals attractions between graphene layers.[59] **Table 1.1** tabulates the major advantages and disadvantages of GLCs and SiN_x-LCs.

The fabrication of GLCs is complicated and the probability of successful encapsulation of liquid between the two layers of graphene depends on factors such as quality of graphene, transfer process used to suspend graphene onto the TEM grid, sample droplet size, and most importantly, the dexterity of hands while fabricating the liquid cell. GLCs are generally preferred for cases where high spatial resolution is required, such as in self-assembly processes,[63] or interaction of nanoparticles with soft-matter,[64] etc. However, to capture the dynamic process of nanobubbles whose minimum size is usually in the range of tens of nanometers, the spatial resolution achieved using SiN_x-LCs is sufficient and acceptable for most cases. **Figure 1.8** shows the TEM images of nanobubbles captured using both SiN_x-LC and GLC.

Table 1.1 Comparison of characteristics of GLCs and SiN_x-LCs

	GLC	**SiN_x-LC**
Spatial resolution	< 1 nm	≥ 2 nm
Thickness	Random (~ 10 nm)	Controllable
Liquid volume	Low, but Difficult to control	High, but controllable
Flow	Incapable	Capable
MEMS integration	Not possible	Possible
Pressure	Depends on graphene vdW forces and column vacuum	Controllable
Susceptibility to Damage	High	Low
Encapsulation efficiency	Skill based (usually low)	High
Operating Cost	Low	High

As discussed in the previous section, different observation methods deploy different techniques for nanobubble nucleation. In the case of LPEM, the nanobubbles are nucleated in-situ due to the interaction between the electrons and the water molecules, and the successive agglomerations of the produced gaseous molecules on the solid surface. This process is called Radiolysis of water, which is discussed in detail while defining the **Nanobubble nucleation strategy** in **Chapter 2**. In SiN_x-LCs, it is comparatively straightforward to nucleate multiple bubbles, as compared to the nucleation in the water pockets of GLCs, which, for most cases, only hold a single nanobubble, thus making it not the ideal choice to study nanobubble interactions and dynamics. As shown in **Figure 1.8**(A), the nanobubbles nucleated due to the radiolysis process can be observed as the regions having brighter intensity in contrast to the liquid. Moreover, multiple bubbles are present which is ideal to study the interactions between the nanobubbles or their dynamic interplay. In the case of GLCs, a single nanobubble may expand and cover most of the water-pocket (liquid region), which usually suppresses further nucleation, hence making the nanobubble immobile and difficult to study nanobubble dynamics.

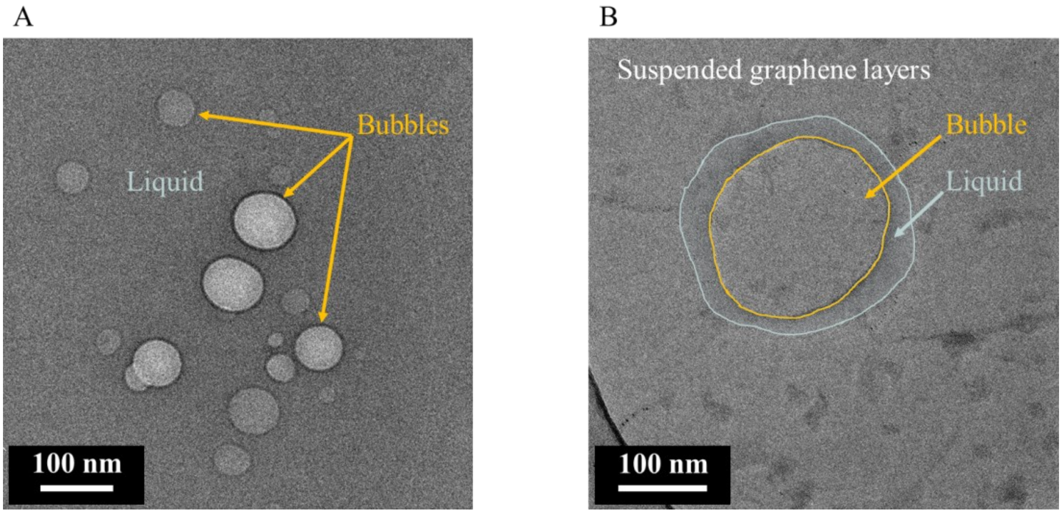

Figure 1.8 TEM image of nanobubbles captured using (A) SiN_x-LC; and (B) GLC.

In TEM, the sample is studied in presence of electron beams which influences the inherent characteristics of the sample and studied phenomenon. Beam-sample interactions during the TEM observation either results in some dynamic processes or some destructive irreversible processes.[65] In fact, in LPEM, the oversaturation of gaseous molecules produced by the electron beam is solely responsible for the nanobubble nucleation. Electron beam also changes the composition of the liquid, alters its pH,[66] and caused charging of windows.[67] Therefore, it is difficult to understand the inherent characteristics of the nanobubbles by TEM only, and the results obtained using other experimental techniques, such as AFM, STXM, etc., and numerical simulations should be used in conjugation with the TEM results to develop an overall understanding of the nanobubbles. The major advantages and disadvantages of the LPEM and the techniques discussed in the previous section is provided in **Table 1.2**. Nonetheless, LPEM is an excellent and the only technique that allows the observation of nanobubbles with such high spatial and temporal resolutions, and the capability to observe the dynamic phenomenon of nanobubbles, even in "beam altered liquid", can provide useful insights towards the much-debated stability and longevity of nanobubbles.

1.2.4 Nanobubbles dynamics

In 1950, Epstein and Plesset gave a theory on the growth and shrinking of bulk bubbles where the far-field gas concentration and gas solubility were important factors in defining the bubble dynamics.[11] Their theory was applied to nanoscale bubbles by Ljunggren and Eriksson in 1997, where they confirmed the difficulty in speculating the existence of nanobubbles beyond microseconds time scales.[21] Although both these theories and their calculations involved bulk bubbles (or nanobubbles), they have been applied to surface nanobubbles by replacing the radius term with the radius of curvature and changing the imposed boundary conditions. Nonetheless, these formulations have acted as the benchmark for questioning the longevity of nanobubbles.

Table 1.2 Comparison of various experimentation capabilities of techniques used for observing surface nanobubbles

	AFM	OM	STXM	LPEM
Spatial Resolution	~ 1 nm	~ 1 µm	~ 100 nm	< 1 nm
Temporal Resolution	~ (O)10^1 s	Real time	~ (O)10^1 s	~ 10 ms
Experimentation Cost	Medium	Medium	High	High
Advantage	3-D profile	Non-intrusive	Gas state	High spatial and temporal resolution

Oversaturation ($\zeta = {}^{c_\infty}/_{c_s} - 1$; c_∞ is the liquid-gas concentration and c_s is the gas solubility) is postulated as an important parameter for the existence and stability of nanobubbles. Even so, the Laplace pressure, which varies inversely with the bubble size, is expected to press out nanobubbles against any oversaturation, and therefore, rendering them a small lifetime.[21,68] However, the dynamics and gas transport are only considered to exist in the near field of surface nanobubbles,[68] and the air diffusion in the liquid is the rate-limiting process for the bubble shrinkage and growth.[68] As the liquid is in oversaturated condition during the existence of nanobubbles, the contact line pinning is believed to provide stability to these gaseous domains, which has also been verified experimentally.[30,31] The noteworthy point about pinning is that the Laplace pressure decreases as the volume of the bubble decrease, and since the contact area remains constant, the contact angle also decreases. Lohse and Zhang derived the relation for the rate of change of contact angle (θ) as:[68]

$$\frac{d\theta}{dt} = -\frac{4D}{L^2}\frac{c_s}{\rho_g}(1+\cos\theta)^2 f(\theta)\left[\frac{L_c}{L}\sin\theta - \zeta\right]$$

where D is the diffusion constant, L is the lateral extension of the nanobubble, ρ_g is the gas density and L_c is the critical lateral extension ($L_c = 4\sigma/P_0 = 2.84\ \mu m$). For clarity, the parameters are shown in **Figure 1.9**(A). For any $-1 < \zeta < 0$, the rate of change of contact angle will be negative, hence, no bubble can exist in the undersaturation conditions. However, for any $\zeta > 0$, a stable equilibrium exists for:

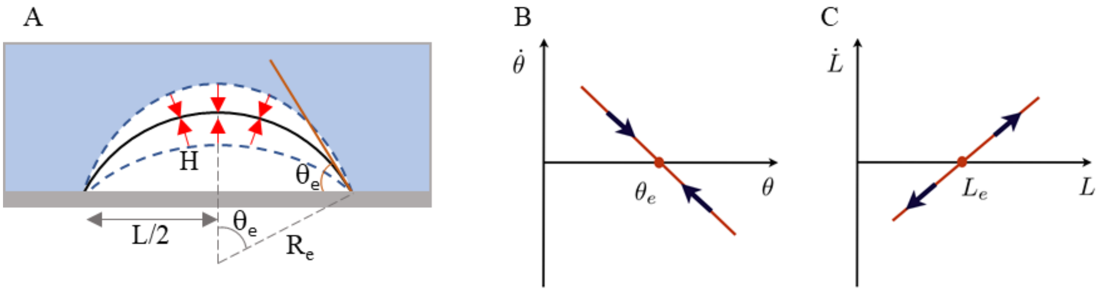

Figure 1.9 (A) Schematic of the pinned surface nanobubble. As $\theta > \theta_e$, the nanobubble shrinks, and $\theta < \theta_e$, the nanobubble grows. (B) Stable equilibrium θ_e for pinned surface nanobubble. (C) Unstable equilibrium L_e for unpinned nanobubble. Image adapted from [68] Copyright © American Physical Society.

$$\sin\theta_e = \zeta\frac{L}{L_c}$$

Therefore, the pinned surface bubbles with $\theta > \theta_e$ shrink (radius increases) and for $\theta < \theta_e$, the bubble will grow (radius decreases), as shown in **Figure 1.9**(A,B). The unpinned surface nanobubbles, however, have an unstable equilibrium and are pressed out for $L < L_e$ due to the Laplace pressure and grow for $L > L_e$ until the bubble detachment due to oversaturation, as shown in **Figure 1.9**(C). For pinned nanobubbles, the balance is although established due to the competitiveness between the Laplace pressure (outflux) and the gas oversaturation (influx). The same result can also be expressed in the universal term, excluding θ_e as:

$$R_e = \frac{L_c}{2\zeta}$$

where R_e is the equilibrium radius of curvature. It is rewarding to note that the relation R_e/L_c is a universal independent of gas type, temperature, substrate,

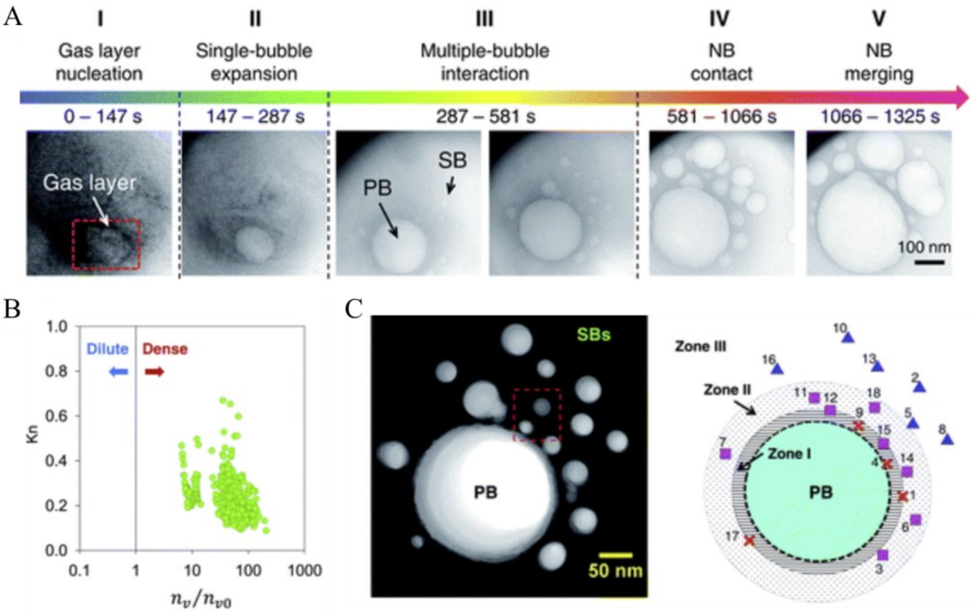

Figure 1.10 (A) Growth dynamics of a NB cluster stimulated via electron-beam radiolysis. (B) Scatter plot of the Knudsen number versus the density number ratio shows the dense nanobubbles. (C) Position-dependent growth of satellite nanobubbles. Image adapted from [35] Copyright © Royal Society of Chemistry.

or the nucleating liquid type, and only depends on the oversaturation parameter.

The prospect of direct observation of nanobubbles provides information on the phenomenon which happens at the real-time scales but remains unveiled using the AFM.[70] Moreover, the mechanisms of nanobubble dynamics, such as their growth, shrinkage, and interactions among neighboring nanobubbles, have not been well understood. There have been few efforts from researchers where they have applied LPEM to observe nanobubbles at real-time scales for dynamic studies. Huang and coworkers studied the generation and growth dynamics of surface nanobubbles nucleated by the radiolysis of KLH protein using a SiN_x-LC based LPEM.[35] Their study showcased the initial gas layer nucleation and its evolution to nanobubble followed by growth and multiple-bubble interaction, as shown in **Figure 1.10**(A). Their results also showed that the nanobubbles are made of dense Knudsen type gas because of the high inner pressure and have a large number density compared to that under STP conditions, as shown in **Figure 1.10**(B). Their study also reported that the dynamics of the smaller nanobubbles (satellite bubbles) were significantly influenced by the neighboring larger nanobubble (parent bubble). Moreover, their results showed that the nanobubbles having low separation had higher growth rates. They proposed the shielding effect of nanobubbles that prevented the dissolution of nanobubbles in the liquid, as depicted in **Figure 1.10**(C).

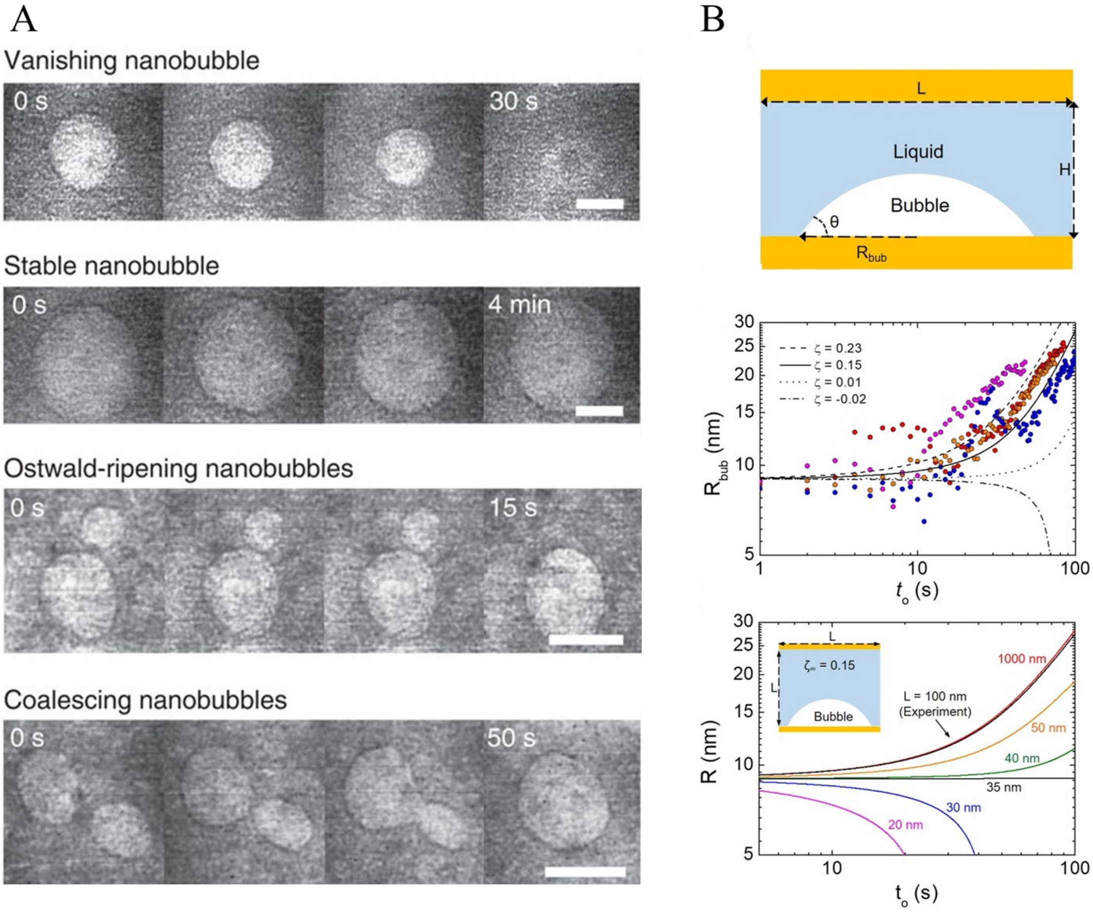

Figure 1.11 (A) TEM images showing vanishing and stable nanobubbles and the Ostwald ripening and coalescence process in nanobubbles. Scale bar 5 nm. Image adapted from [37] Copyright © Nature Springer. (B) (top) Schematic of the nanobubble system confined within the rectangular box. (middle) Temporal evolution of the radius of the nanobubble obtained by solving the model developed in their work. (bottom) Temporal growth of nanobubble with initial radius 9 nm confined in the finite volume of the system, with length varying from 1000 nm to 20 nm. Image adapted from [71] Copyright © Nature Springer.

To facilitate the study of smaller nanobubbles, Shin and coworkers used GLC to study the growth dynamics and gas transport mechanisms of nanobubbles.[37] They studied nanobubbles having diameters ranging between 5-15 nm, and found that the critical radius of nanobubble to be 5.5-7.1 nm. As shown in **Figure 1.11**(A), they also observed vanishing nanobubbles, stable nanobubbles, and other dynamic phenomena such as Ostwald-ripening and coalescing nanobubbles, which are difficult to observe using other visualization techniques. Interestingly, they observed the direct unhydrated gas transport mechanisms in nanobubbles that are facilitated through the ultrathin water membrane between two nanobubbles. In a similar study using GLC, Kim et al. studied the initial growth dynamics of 10 nm nanobubbles.[71] They studied the temporal growth of nucleated nanobubbles and modified the classical diffusion theory by considering the finite size of the confined system of GLC. They introduced the ζ parameter in the diffusively controlled growth of gas nanobubbles, suggesting nanobubble growth for positive ζ, as shown in **Figure 1.11**(B). They concluded that the characteristic length of the liquid body in the GLC is a critical factor in nanobubble growth, if and when, the size of nanobubble is comparable to the encapsulated liquid. Their study also showed that the gas concentration in the liquid reduces as the dissolved gases in the liquid transfer to the nanobubbles, which in return affect the growth dynamics of the nanobubbles.

In contrast to the thinner GLCs, SiN_x-LCs have two nucleating surfaces (windows) available for heterogenous nucleation, hence it is important to understand the relative positioning of nanobubbles for a better understanding of the nanoscale phenomenon and interactions. Tomo et al. developed a visualization strategy deploying the focus plane of the image which can be varied to determine the relative position of the nanobubbles using the Fresnel fringes formed around the nanobubbles (**Figure 1.12**(A)).[34] They used this

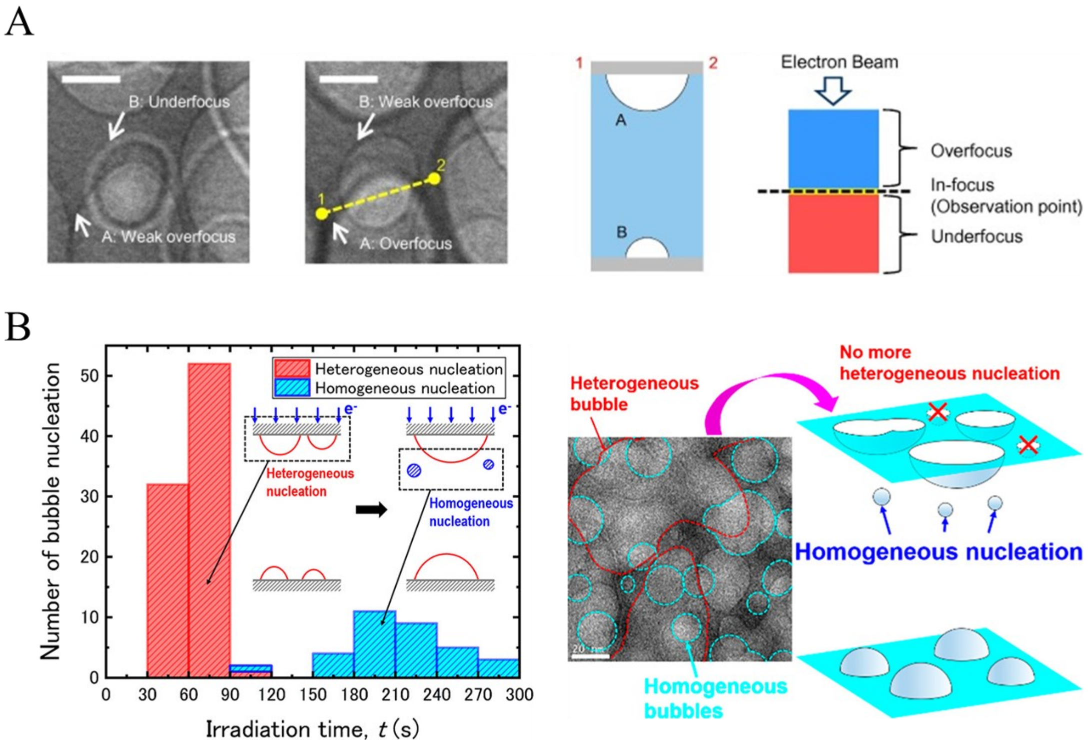

Figure 1.12 (A) Fresnel fringe method to determine the relative position of the bubble by varying the in-focus plane. Image adapted from [34] Copyright © Elsevier. (B) Heterogeneous and homogeneous nucleation in the upstream side of the electron beam observed. Image adapted from [72] Copyright © American Chemical Society.

strategy to locate the preferred nucleating surfaces in the SiN_x-LC and the initial growth of nanobubbles. Interestingly, they observed the homogenous nucleation of nanobubbles, which itself is a very unique phenomenon.[72] They found that the homogenous nucleation is preferred after prolonged irradiation of the electron beam due to the Ostwald ripening and lower surface tension due to the generation of ions and radicals favor the homogenous nucleation (**Figure 1.12**(B)). A recent LPEM study of the nanobubble dynamics in the soluble surfactant solution shows that the gas transport frequently occurs without interfaces merging, while a narrow distance is maintained between the interfaces of interacting surfactant-laden nanobubbles.[73] Additionally, their study showed several other phenomena, such as direct gas transport between two nanobubbles, followed by the nanobubble merging. Interestingly, the study also showed interface relaxation processes for nanobubbles and the gas-liquid interface deformations.

1.2.5 Applications of nanobubbles

1.2.5.1 Role in liquid vapor phase change

Liquid vapor phase change is a ubiquitous physical process, relevant to both industry and nature, and has wide applications ranging from generation of electricity to thermal management of high-power density electronics.[74] Nearly 60% of the world's electricity, directly or indirectly, depends on the water to steam conversion,[75] and any improvements, such as the early incipience of boiling or better control over boiling, will lead to efficiency improvements in power plants. The liquid-vapor phase change is also relevant for adequate electronics device performance and reliability as it is important for the thermal management of high-power density electronics. The field of information and communication technology (ICT) is expected to grow to more than double of its present size in next 10 years, where the data centers will be the leading gainers in terms of growth in ICT domain.[76] Generally, a conventional data center gobbles up nearly 40% of its energy requirement to sustain its cooling requirements and thermal management of devices,[77] and therefore, the challenge is to minimize the energy requirement for their cooling. Moreover, the feature sizes of transistors are shrinking and fabrication is becoming more intricate (**Figure 1.13**(A)), which strongly indicates that future electronics components will need to have micro/nanoscale embedded cooling channels (**Figure 1.13**(A)) in order to achieve size/weight reduction targets and for efficient thermal management by keeping the junction temperature in check. Therefore, to keep up with this pace, it is essential to understand phase change phenomenon at the smallest scales and look for techniques to enhance it.

Previously, there has been few studies which associates early onset of nucleate boiling to the presence of nanobubbles. For example, Cavichhi and Avedisian heated a thin metal film impulsively using two consecutive heating pulses to infer the presence of nanobubbles and concluded that the transient vapor nanobubbles formed after the collapse of bubble nucleated during the first pulse leads to the early incipience of second bubbles, much below the nucleation temperatures, as shown in **Figure 1.13**(B).[78] Since then, there has been numerous studies suggesting that liquid boiling often occurs at lower supersaturation than expected, and most of the times, gas tapped in the cavities or nanobubbles are considered responsible for such behavior by serving as nuclei for bubbles. In a previously reported analytical study, it was concluded that the metastable nanobubbles nucleate the liquid-to-vapor transition by serving as an intermediate phase, as shown in **Figure 1.13**(C).[79] Hence, nanobubbles has the tendency to act as the nuclei for vapor bubbles and therefore, are critical for the early incipience of boiling. Moreover, as the electronic scales are shrinking, the nanobubbles present on the surface are expected to affect the flow dynamics, which makes them more important.

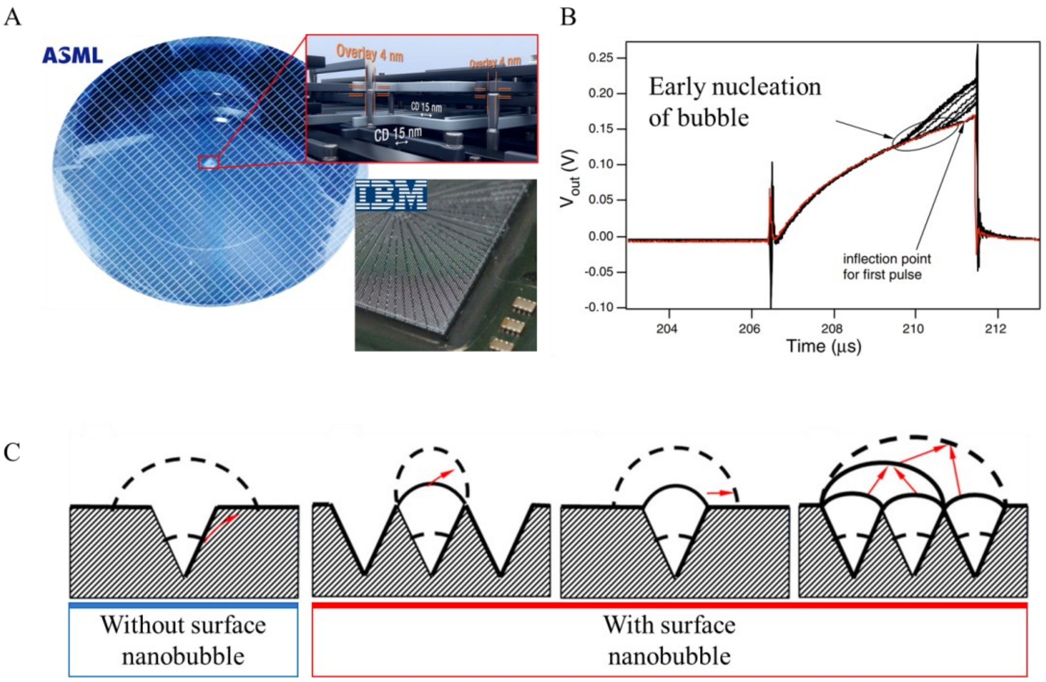

Figure 1.13 (A) Silicon wafer with fabricated intricate features having critical dimensions in order of 10 nm (inset) for next generation electronics. IBM chip having embedded channels for thermal management. Image Copyright © ASML Holdings and IBM. (B) Early nucleation of bubble due to formation of nanobubbles after collapse of first bubble. The Y-axis here can be correlated with surface temperature. Image adapted form [78] Copyright © American Physical Society. (C) Bubble nucleus growing from possible ideal configurations of a vapor-trapping crevice via a pathway: without (left) and with surface nanobubbles. The solid curve shows the metastable nanobubbles already present at the surface. Image adapted form [79] Copyright © American Chemical Society.

1.2.5.2 *Other applications*

Surface nanobubbles have various applications and technical relevance, owing to their unique properties and characteristics. Surface nanobubbles are known to enhance the attractive interactions between the hydrophobic surface,[80] hence they can be used in floating processes such as mineral or fine coal separation processes (**Figure 1.14**(A)),[81] solid impurity removal for wastewater treatment,[82] oil separation,[83] and in other separation processes. The separation processes using nanobubbles can further be optimized by changing the gas type and gas concentration dissolved in the liquid for nanobubble interactions. Moreover, due to their small size, they can be targeted towards minute particles having the size in the order of nanobubbles' size.

Surface nanobubbles are known to control various fluidic phenomena, such as initiation of liquid film rupture during drainage of the film,[84] and nucleation of microdroplets from a retracting liquid film,[85] as shown in **Figure 1.14**(B). During the film drainage, a foam is believed to form between the nanobubble and the film surface, which imparts additional capillary pressure assisting in the destabilization of thin-film and its rupture. Moreover, surface nanobubbles are also believed to nucleate the boiling,[79,86] even though there is some ambiguity in its description.[85] These gaseous domains raise much lower energy barriers in comparison to vapor-filled cavities.[87] Hence, the vapor and gas molecules can be pulled into the bubble embryos, leading to low-superheat boiling incipience.[86]

Surface nanobubbles also have the capability to provide a template for the fabrication of nanomaterials, nanopatterns, and nanostructures. As the bulk liquid evaporates leaving behind the material which engulfs around a nanobubble, nano-assembly of materials occurs and they transform into a hemispherical or semi-spherical nanostructure, depending on the wettability of the nucleating surface. Moreover, the bursting of nanobubbles can also be utilized to form ring-shaped structures, as hypothesized by Zhang and Lohse.[88] Moreover, the nanobubbles can be utilized for the growth of sub-micrometer-sized vaterite tubes.[89] Researchers have also demonstrated the application of nanobubbles in the fabrication of nano-porous films, where the pore size and pore density can be controlled by varying the nucleating parameters.[90]

They also find relevance in cleaning the surfaces, e.g. cleaning of protein-coated surfaces,[91] or for de-fouling the surfaces, and well as prevention of surface fouling.[92] Surface nanobubbles can also be utilized in catalyzing the reactions, such as the production of chlorine, photocatalysis, syngas catalysis,[93], etc. The bubble dynamics, such as the collapse of the bubble can also be utilized to decelerate reactions by damaging the surface by cavitation.[94] The plasmonic nanobubbles, composed of vapor instead of gas, are highly functional and find their application in harnessing solar energy with the help of metallic nanostructures.[95] Plasmonic nanobubbles also find their application in catalysis.[42] Many laser-assisted experiments suggest substantial superheating, sometimes up to 460 K, before the nanobubble nucleation. Due to the highly transient nature of plasmonic nanobubbles, it requires tools with very ultrahigh temporal resolutions for their observation and understanding. Plasmon-enhanced nanobubbles also find their application in targeted cell therapy for cancer treatment, as demonstrated in **Figure 1.14**(C).[96] A recent study also

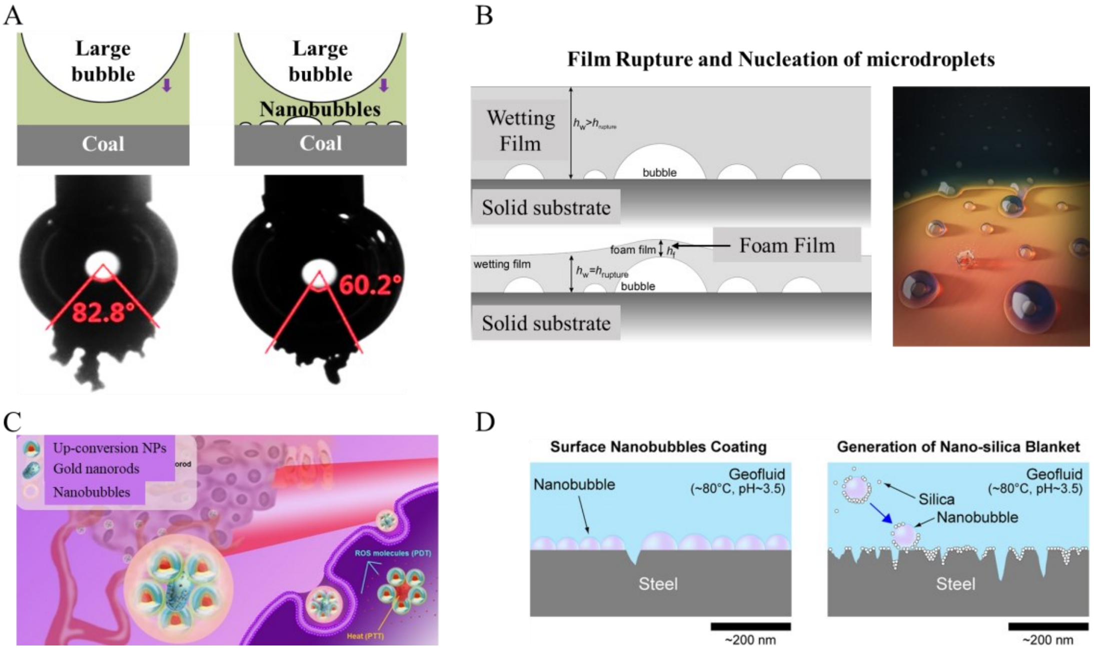

Figure 1.14 Applications and technical relevance of surface nanobubbles. (A) Role of nanobubbles in separation of fine coal particles. Image adapted from [81] Copyright © Elsevier. (B) Role of nanobubbles in film rupture and microdroplet nucleation. Images adapted from [84,85] Copyright © American Chemical Society, American Physical Society. (C) Role of nanobubbles in cancer cell therapy. Image adapted form [96] Copyright © Theranostics. (D) Role of nanobubbles in inhibition of corrosion. Images adapted from [97] Copyright © Elsevier.

demonstrates the application of nanobubbles in corrosion-inhibition of steel samples in the presence of acidic geothermal water, as shown in **Figure 1.14**(D).[97] Thus, surface nanobubbles could provide an environmentally friendly solution for limiting the corrosion of the pipes by nucleating a nanobubble protective layer on the possible corrosion sites. Nanoimprint lithography is another field which is affected by the nanobubbles, albeit in a negative fashion.[98] The defects at the nanometre scale line patterns are prominent due to the presence of nanobubbles and the challenge still remains to understand the nanobubble behaviour so that the defects can be controlled for performance enhancement for semiconductor fabrication.

With the progression and further understanding of the surface nanobubbles and their dynamics, several research subjects are poised to gain and advance for more exotic applications such as surface modification by nanobubbles for pattern formation, soft lithography, infection control by surface modification, drag and slip control, catalysis, stable hydrophobic nucleation sites for bubble nucleation in two-phase thermal management of electronics having nanometre scale characteristic length, etc.

1.3 Research Objectives

For nearly 30 years now since the first speculations about the existence of surface nanobubbles were made,[20] tremendous progress has been made on understanding their general characteristics such as stability, longevity, state of gas, physical properties, etc.[42,99–102] Importantly, AFM have born the burden of capturing such behavior for the apprehension of surface nanobubbles, however, their poor temporal resolutions have kept the dynamics of surface nanobubbles as the unknown territory for long now. Recently, several attempts to understand surface nanobubbles with high temporal resolutions have gained momentum,[34,35,71,103,104] but a comprehensive study on delineating their dynamic characteristics has been missing across the research databases. Understanding the dynamics is critical in defining the exotic characteristics of nanobubbles, such as their pinning, or gas influx-outflux balance, or the interactions and exchanges between the neighboring nanobubbles. Moreover, understanding this can help in the development of several research fields such as surface modifications, catalysis, thermal management of miniaturized electronics, etc. With the stated research gap in the dynamics of surface nanobubbles, we have utilized the in-situ liquid phase electron microscopy technique to study the temporally resolved behavior of surface nanobubbles.

The major research objectives of the present study are as follows:

- To understand and analyze the nucleation, size distribution and number density of the surface nanobubbles nucleated using the in-situ liquid-phase electron microscopy.
- To establish the interacting mechanism between the surface nanobubbles, and understand important parameters affecting such behavior.
- To capture the dynamics of nanobubble coalescence, and understand the unique shape these nanobubbles exist in.
- To demonstrate an application of surface nanobubbles nucleated using an electron beam.

The findings presented in this thesis will help the field of surface nanobubbles to mature. Primarily, this study will aid the understanding of the surface nanobubbles and their dynamics, and help their application in the domains of surface engineering, flow in nanochannels, bubble nucleation, point-of-care devices, catalysis utilizing hydrogen, ion segregation, reaction dynamics, etc.

1.4 Outline and Scope of Thesis

The thesis focuses on unveiling the dynamic behavior of surface nanobubbles using in-situ liquid-phase electron microscopy. The nanobubbles are nucleated in-situ using the radiolysis phenomenon and the size and the number density were controlled using the devised nucleation strategy. The interaction between the nanobubble pair and the coalescence behavior of the nanobubbles was then examined. Furthermore, nanobubbles were printed in patterns using the electron beam, and their ability to attract the ions from the parent solution is explored.

The thesis is organized into five chapters:

In **Chapter 1**, the general background on the nano-fluidics and nanobubbles has been given. A brief review of the existing knowledge about the nanobubbles, their characteristics, along their historical preview has been presented. This chapter also elaborates on the visualization techniques employed to understand their characteristics. The liquid phase electron microscopy technique is highlighted for its application to capture the nanobubble dynamics with high temporal and spatial resolutions. The chapter concludes with the research objectives and general outline of the thesis.

In **Chapter 2**, firstly, the nucleation strategy to attain nanobubbles with differential size and number density is elaborated. Further, the interactions between a nanobubble pair are examined and the role of asymmetric distribution of oversaturation in the depinning of a stably pinned nanobubble is studied. The unique pull-push phenomenon between the nanobubbles' contact lines is also examined and is attributed to the vdW and the electric double layer (EDL) interactions. It is then proposed that their counter-intuitive longevity and reluctance to merge is due to the EDL encompassing them.

In **Chapter 3**, the coalescence mechanism in the quasistatic pinned nanobubbles is focused upon. The nanobubbles are observed to show reluctance to merge via direct contact, instead, it is found that a thin gas layer formed between the adjacent interfaces of the nanobubbles tends to initiate the merging process. This gas layer acts as a bridge between the nanobubbles and slowly evolves in the transverse as well as normal direction, thus completing the merging process. Further, the magnitude of oversaturation is observed to affect the rate of gas film formation and merging of nanobubbles.

In **Chapter 4**, the methodology to write nanobubbles using an electron beam pen is proposed and devised. The patterns, comprising of nanobubbles, printed using the electron beam are experimentally observed to be stable for > 1 hour. Further, the pattern also shows high stability in flows.

In **Chapter 5**, the concluding remarks for the above chapters are elaborated and the potential contributions to the field are presented. Further, future research directions necessary to understand these nanoscale gaseous domains are recommended.

Overall, our study on the nanobubbles using the in-situ liquid-phase electron microscopy sheds light on the previously uncaptured dynamic behavior of nanobubbles and provides pertinent mechanistic insights on the nanobubble's longevity, interactions, coalescence phenomenon, along with presenting a methodology to attain tailored nucleation and writing nanobubble patterns.

2

Nanobubbles and their Related Interplay[†]

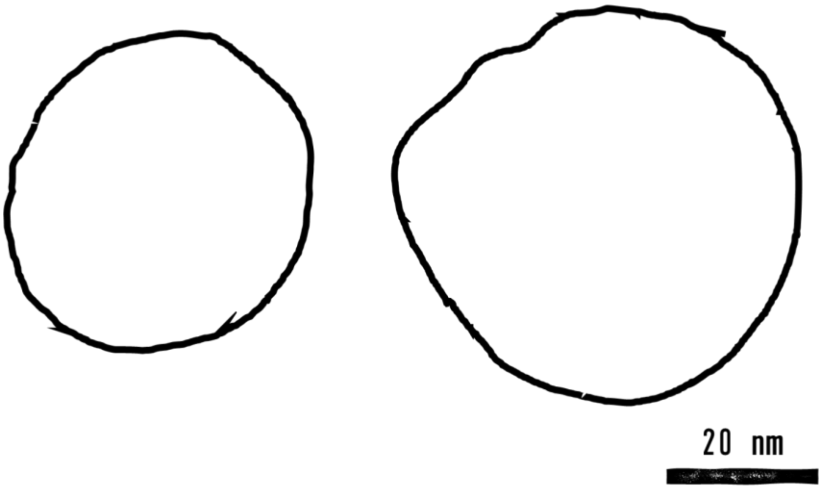

[†] Adapted with permission from "*Nag, S., Tomo, Y., Teshima, H., Takahashi, K. & Kohno, M.* Dynamic interplay between interfacial nanobubbles: Oversaturation promotes anisotropic depinning and bubble coalescence. *Physical Chemistry Chemical Physics* 23(43), 24652-24660 (2021)" DOI: https://doi.org/10.1039/D1CP03451K Copyright © 2021, Royal Society of Chemistry.

In this chapter, we establish a methodology to nucleate nanobubbles in an open system liquid cell using TEM. By controlling the beam intensity, nanobubbles of two specific size range and number density are nucleated: 11-25 nm radius but densely populated and 30-40 nm radius but sparsely populated. Further, by nucleating the sparsely populated nanobubbles, we attempt to gain insights into nanobubbles' behavior and their interfacial dynamics. Interestingly, we could observe a freely growing-shrinking nanobubble and a pinned nanobubble at the same experimental conditions, suggesting the possibility of multiple nanobubble stabilization theories and pathways. Remarkably, the study reveals that a freely growing-shrinking nanobubble induces anisotropic depinning in the three-phase contact line of a strongly pinned neighboring nanobubble. The anisotropic depinning is attributed to the differential local gas saturation levels, depending on the relative positioning of freely growing-shrinking nanobubble. Further, we also observed the unique pull-push phenomenon exhibited by the nanobubble's interfaces, which is attributed to the van der Waals interactions and the electric double layer (EDL), collectively. The role of the EDL in suppressing and delaying the merging is also highlighted in this study. Apart from providing a methodology to nucleate nanobubbles, the present chapter aims to reveal the role of locally varying gas saturation in the depinning of nanobubbles, their longevity due to EDL, and the consequent coalescence, which is crucial to understand the behavior of nanobubbles.

2.1 Background

The progression from macroscales to nanoscales, especially at the interfaces, induces notorious behaviors and much-unexpected transition from the familiar bulk behavior.[105,106] On a similar tone, surface nanobubbles[42,88,107,108] have continued to perplex researchers for nearly three decades now.[20] The classical Young-Laplace equation, otherwise valid at the nanoscale,[109] predicts an unusual high internal pressure of tens of atmospheres inside a bubble of a few nanometre radii. Likewise, the Epstein-Plesset theory on the stability and dynamics of gas bubbles[11] predicts the dissolution timescales in the range of a few microseconds for nanobubbles,[21,110] yet their week-long stability has been confirmed using numerous experimental techniques.[101,111] Therefore, efforts are required to investigate their dynamic behavior. In addition, their unique applications and the functional advantages, for instance, in chemical energy storage,[112] surface cleaning,[92] water treatment,[82] assisted nanofabrication,[113] boiling nucleation,[114] and surface drag reduction[115] have thrust the interest to understand their behavior and dynamics to further explore their potential applications.

Numerous experimental techniques have been applied to demonstrate the existence of surface nanobubbles and to characterize their behavior:[42] atomic force microscopy (AFM),[39,43,116–119] optical microscopy,[33,46,120] scanning transmission X-ray microscopy (STXM),[38,47] and liquid-phase electron microscopy (LPEM).[31,35,72,103,121] AFM has been used extensively due to its capability of providing information about the three-dimensional topography of nanobubbles and studying characteristics like contact angles, height and longevity as well as distinguishing between the nanobubbles and micro/nano-pancakes.[102,122] In fact, the long-term stability of surface nanobubbles has been proved experimentally using AFM. However, the time resolution of AFM is in order of tens or hundreds of seconds which renders them unsuitable to capture the dynamic behavior of nanobubbles. Advanced optical microscopy techniques have good temporal resolutions to capture nanobubbles' dynamic behavior but are incapable to capture ultra-fine nanobubbles having a size less than 100 nm.[120] Similarly, STXM also has a low spatio-temporal resolution, although it provides comprehensive information about the density of the gas phase in and around nanobubbles which contributes towards the understanding of gas behavior at the nanoscale.[38,47] LPEM, on the other hand, can observe the nanobubbles with high temporal and spatial resolutions.[31,58] Moreover, the in-situ nanobubble nucleation in the protic liquids due to radiolysis mediates the high time-resolved observation of the bubble dynamics such as their growth, shrinking, and dependence on the neighboring nanobubbles which holds importance in characterizing these nanoscale domains. Recent investigations on nanobubbles using transmission electron microscopes (TEM) have unveiled distinctive nanoscale gas transport and nanobubble behavior, such as direct fast gas transport between the nanobubbles through the instantaneous rupture of the ultrathin liquid film in a graphene liquid cell.[37] A similar study using graphene liquid cell revealed the dependence of inter-bubble gas transport, bubble shape, and bubble growth on the relative size of the nanobubbles.[36] Additionally, the advancements in nanofabrication and the development of silicon nitride (SiN_x) membrane liquid cells have helped in understanding nanobubble dynamics with better control over nucleation surfaces, liquid thickness, and other physical parameters. SiN_x cell based LPEM has revealed significant gas and nanobubble behavior at nanoscale such as the diffusive shielding for smaller nanobubbles,[35] unexpected homogenous nucleation of nanobubbles near the solid-liquid interface [72] and more recently, the mechanistic involved in pinned surface nanobubble merging.[121] Hence, the application of LPEM in observing and understanding nanobubble dynamics becomes highly relevant.

The available literature attributes the stability of the surface nanobubbles to the oversaturation and contact line pinning.[68,123,124] However, nanobubbles exhibit complex phenomena and it is difficult to construe the stability of nanobubbles on basis of any single novel model. Additionally, nanobubbles have been observed to be stable, both numerically and experimentally, in normal, or even in undersaturated conditions rather than undergoing dissolution.[69,100,125] On the contrary, the stability of the surface nanobubbles, in absence of contact line pinning, has also been studied and seems valid.[126,127] Hence, understanding the nanobubbles' phenomenon and dynamics is tedious and requires further studies to answer such complex physiochemical phenomena. LPEM, due to its high temporal resolution, has revealed the shrinking, growing, and merging of nanobubbles in real-time,[34,37,72] which also advocates for its utilization to understand the phenomenon that can provide answers towards stability and longevity of nanobubbles. On the other hand, several literatures also contemplate the role of the diffused double layer in the existence and stabilization of nanobubbles.[108,128–132] The charges at the bubble interface and their repulsive interaction create a net electrostatic pressure acting radially outwards, opposite to the Laplace pressure. An individual nanobubble is, therefore, encompassed in its EDL whose thickness is a function of ionic concentration, liquid properties, and temperature.[133]

In the present investigation, we have used LPEM to focus on the interactions between surface nanobubbles. The salient feature of this study is that we could observe nanobubbles with radii less than 50 nm at a higher resolution for a long duration, which allowed us to understand the slow-interplay these bubbles undergo. The nanobubbles were nucleated and probed in thin water film using the TEM. We observed neighboring nanobubbles showing contrasting behavior at similar experimental conditions: pinned nanobubble and freely growing-shrinking nanobubble. Next, we studied the interactions among the contrasting nanobubbles and found that the shrinking of the unpinned nanobubbles induces directional depinning in the pinned nanobubbles. This signifies the anisotropic gas transport as well as the presence of localized saturation regions near the interface. Further, the push-pull phenomena between the bubble interfaces were observed multiple times. We consider that the EDL exhibiting repulsive interaction is responsible for the push, whereas the attractive van der Waals interaction, coupled with the localized high saturation regions is responsible for the pull or the directional depinning. Last, we propose and evaluate the interacting pathway for these nanobubbles. Along with highlighting the utility of LPEM in understanding nanobubbles, the presented work essentially demonstrates the interplay between the nanobubbles, along with evaluating the stability of nanobubbles and gas transport at the nanoscale.

2.2 Experimental Methods and Procedures

2.2.1 Experimental equipment

The experiments were carried in a commercially available SiN_x liquid cell electron microscope system (Poseidon Select, Protochips Inc., U.S.A.),[134] as shown in **Figure 2.1**(A). It is an *in-situ* electron microscopy platform that allows direct observation of fluid inside the high vacuum of the TEM column. This liquid cell electron microscopy system also has the provision to flow liquid, which is important to refill the cell in case of de-wetting. The observation domain is situated at the tip of the holder, whose magnified view is shown in **Figure 2.1**(B). The fluid is encapsulated between two silicon environmental chips (e-chips) having SiN_x windows suspended through the trapezoidal prism cavity. **Figure 2.1**(C) shows the representative image of the small e-chip and large e-chip. The small e-chip has the dimensions of 2 mm × 2 mm × 300 μm, whereas the large e-chip is 4.5 mm × 6 mm × 300 μm. The small e-chip also has 4 spacers (Su-8 epoxy based resist) at its corners to accommodate liquid thin-film of desirable height between the e-chips.

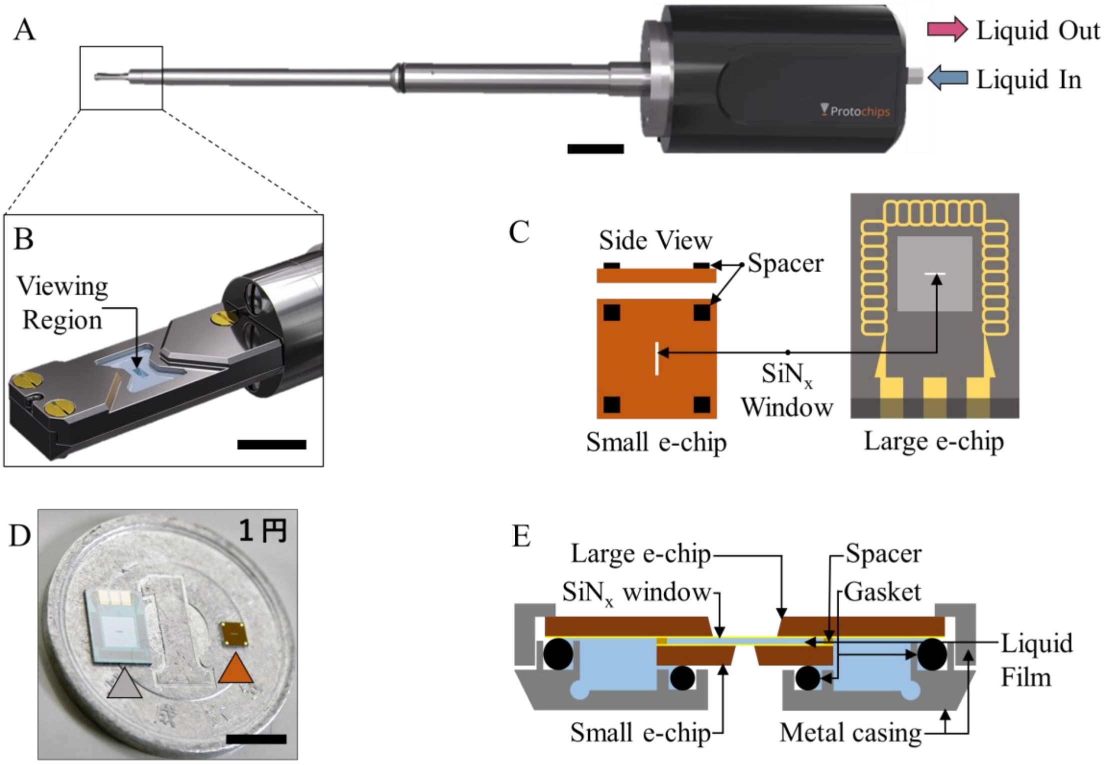

Figure 2.1 Experimental equipment for the nanobubble observation. (A) LPEM system: Poseidon Select, Protochips Inc. Scale bar: 2cm. (B) Magnified view of the tip of the LPEM system. Scale bar: 6 mm. Copyright © Protochips Inc., USA. (C) Representative images of e-chips used in the experiment. Image not to scale. (D) Large e-chip (grey triangle) and small e-chip (orange triangle) placed on a 1-Yen coin (∅ 20 mm). Scale bar: 5 mm. (E) Schematic image of the assembled liquid cell showing the encapsulated nanometre scale thin film between the e-chips.

The e-chips used in the experiments (large e-chip: EHT-45ZZ, Protochips Inc., U.S.A.; small e-chip: EPB-55DS, Protochips Inc., U.S.A.) have a 50 nm thick SiN$_x$ windows suspended through a trapezoidal prism cavity, having dimensions 400 µm × 50 µm cavity for the EHT-45ZZ e-chip and 550 µm × 50 µm for the EPS-55DS e-chip. The detailed description on their dimensions is provided in the supplementary information (**Figure S1**). **Figure 2.1**(D) shows the large e-chip and small e-chip placed on a 1-Yen coin, highlighted by grey and orange triangle, respectively, and **Figure 2.1**(E) shows the schematic of the assembled liquid cell with the nanometre scale encapsulated thin film. The experiments were attempted with two spacer height configurations (150 nm or 500 nm), however, for our configuration and the available microscopy facility, no nanobubble nucleation was observed using 500 nm spacer height. Hence, the results presented in this chapter, and the following chapters are with 150 nm spacer height. Moreover, even if the spacer height is 150 nm, it is important to emphasize that the height of the liquid is usually much larger (~1 µm at central region) than the spacer height due to the bowing of windows in high TEM vacuum.[135] Imaginably, the bowing in the 500 nm spacer height configuration would have further increased the height and liquid volume which might adversely affect the nucleation. To minimize the bowing, the e-chips were assembled in a cross-aligned configuration, and hence the available viewing area was 50 μm × 50 μm. The liquid cell used in the study is open to the ambient due to the flow spacers in the used e-chip configuration, which is contrary to the SiNx based liquid cells used previously.[34,35,72] The surface of these silicon e-chips was cleaned and hydrophilized using a glow discharge plasma reactor (PIB-10, Vacuum Devices, Japan). This is an important step to encapsulate a stable water film at such nanoconfinement levels and avoid liquid film retractions. This also rendered high hydrophilicity to the SiN_x chip with static contact angle <5°. Water used in the experiments was purified and deionized using a reverse osmosis water purifier (Aquarius RFP742HA, Advantec, Japan). Although deionized water was used for the experiment, carbon dioxide from the atmosphere is expected to increase the pH of the water due to the absorption of carbon dioxide during prolonged exposure to the ambient. Hence, the initial ionic strength and the pH of the water were 2×10^{-6} M and 5.6, respectively. After assembling, the liquid cell was kept in a vacuum pumping station (10^{-3}~10^{-4} Pa) and water was allowed to flow between the e-chips for ~12 hours to ensure its integrity before loading into the TEM column. After loading the sample into the TEM, the flowing water was allowed to complete one cycle in order to eliminate any air cavities in the liquid cell. All the observations were carried in static conditions with no flow inside the liquid cell.

The sample was imaged in a TEM (JEM-2100Plus Electron Microscope, JEOL Ltd., Japan), operated at an accelerating voltage of 200 kV. This TEM has a thermionic electron emission source (LaB_6 filament), whose current density is three orders less than the field emission electron sources, and hence has minimal beam effects on the sample.[37] This allowed for the long observations, sometimes for several tens of minutes, at the same viewing region without window damage or failure. The observations were done at room temperature (R.T.: 22°C) and all the images were acquired without flow in the liquid cell. CMOS camera (Rio 16, Gatan Inc., U.S.A.) installed in the TEM was used to capture individual images (at 4K resolution) and videos (at 1K resolution, 40 fps).

2.2.2 Imaging and analysis

The interaction between the electrons and the sample produces a greyscale image whose intensity depends on the local mass or thickness in the sample; hence, it is critical to use a systematic image processing methodology. Moreover, to understand the dynamics of the nanobubbles, a potent edge detection algorithm needs to be deployed. In our study, we used MATLAB for image handling, image pre-processing, and nanobubble edge detection. Firstly, the image frames were sequentially retrieved from the 40-fps video, and the frame retrieval rate was decided based on the speed of the phenomenon. In

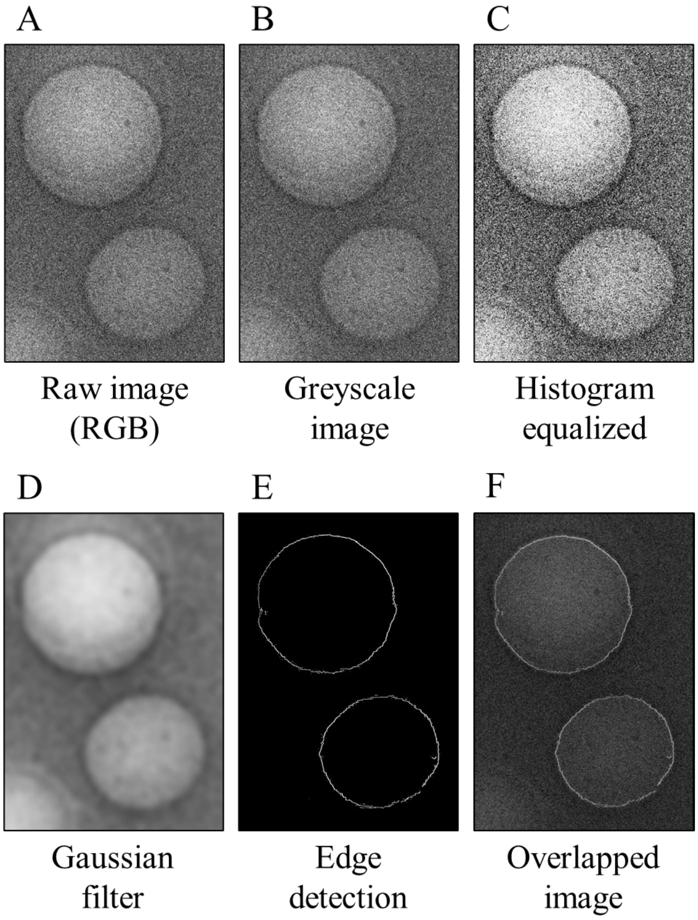

Figure 2.2 Sequential snapshots of the nanobubbles′ TEM image showing the results of various operation applied for the edge detection. (A) Raw image captured in RGB format. (B) RGB image converted to grey scale image. (C) Image contrast enhancement done using histogram equalisation. (D) Gaussian smoothening filter with standard deviation $\sigma = 10$ for noise reduction. (E) Detection of the nanobubbles′ interfaces carried using Canny edge detection algorithm using sensitivity threshold $\vartheta = 0.4$. (F) Edge detected image and original image overlapping shows accurate edge detection.

general, fast dynamics are expected at the nanoscale, but the bubbles, or liquid-solid-gas interfaces in general, were observably slow, which agrees with the previous reports.[35,36] Although the slow dynamics remains an open-question for experimental nanofluid dynamicists, a probable explanation could be the damped diffusion near the contact line due to presence of hydration layer and elevated viscosity of liquid near the solid interface.[103,136] The acquired frames, initially in RGB array (1024×1024×3) were converted to greyscale (1024×1024×1) for easier implementation of the subsequent operations (**Figure 2.2**(A&B)). The histogram equalization operation was then applied to the greyscale image to enhance the image contrast (**Figure 2.2**(C)). TEM images have an inherently low S/N ratio, hence, the gaussian smoothening filter was applied for background noise smoothening and improving the S/N ratio (**Figure 2.2**(D)). The edges (or boundaries) of the nanobubbles were then detected using the Canny Edge detection algorithm (**Figure 2.2**(E)). It works by finding the intensity gradients above the threshold in the image created due to the formation of dark Fresnel fringes in the overfocussed TEM image. **Figure 2.2** shows the sequential snapshots of the resultant images formed by the applied image processing procedures on a sample nanobubble image. The overlap of edge detected image and the original image (**Figure 2.2**(F)) shows the acceptable level of edge detection carried out by the image processing procedures. The physical measurements on the edge detected binary image was carried using an open-source image processing and scientific image analysis package: Fiji.[137]

2.3 Results and Discussions

2.3.1 Nanobubble nucleation strategy

It is *posteriori* that the existence of the nanobubbles is governed by the oversaturation ζ in the liquid medium,[68] and electron beam from the TEM plays a vital role in creating the conditions favoring nucleation of nanobubbles in the liquid cell.[138] **Figure 2.3**(A) shows the schematic of the liquid cell where the nanobubbles are generally nucleated on available nucleating surfaces, i.e., both at upper and lower SiN_x windows. As the liquid thin film in the liquid cell is irradiated with the electron beam, the collision between the electrons and the H_2O molecules leads to the formation of products such as: e_h^-, $H^\bullet$, $OH^\bullet$, H_2, H_2O_2, H_3O^+, $HO_2^\bullet$. This process of dissociation of water molecules by ionizing radiation is known as Radiolysis. The concentration of the products formed during the radiolysis is proportional to the electron dose rate. Among the products, the gaseous molecules play a major role in the nucleation of the nanobubbles, i.e., once the liquid becomes oversaturated with the gaseous molecules, these gaseous species agglomerate on the solid surface and nucleate the nanobubbles, as represented using a schematic in **Figure 2.3**(B). Furthermore, it was previously established that the nanobubbles can only be observed on the hydrophobic surfaces, however, numerous new studies, including this study, showcases the nucleation and observation of nanobubbles observation on a highly hydrophilic SiN_x surface (CA $< 5°$). This also reaffirms that oversaturation is one of the critical governing factors for the existence and stability of nanobubbles on the hydrophilic surfaces.

It is important to note that the nanobubbles nucleated in the LPEM are not the vapor bubbles, but the gas bubbles majorly composed of H_2 and O_2. Previous studies have clarified that the interaction between the water molecules and the electron beam does not cause any beam-induced heating in the liquid cell.[138] In fact, we also tried heating the liquid cell up to 100°C (safe limit) in some of our experiments but did not observe nanobubble nucleation or inferable changes in the already nucleated nanobubbles. Although the effort remains beyond the scope of this thesis, we sometimes observed rapid drying of the thin water film while heating. The positioning of heater with respect to the viewing region (> 1.5 mm) could be the reason behind rapid drying and no changes in the

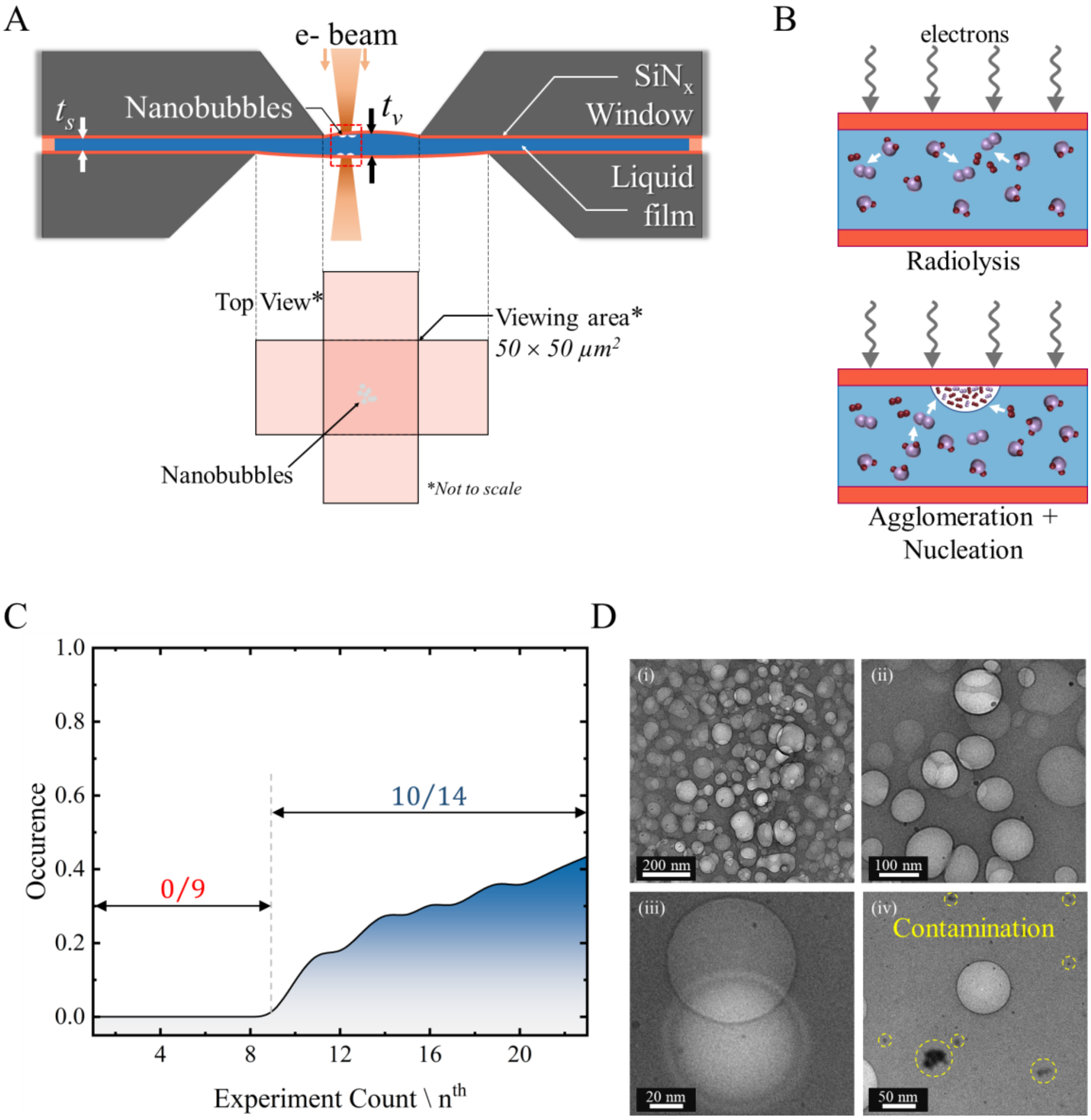

Figure 2.3 (A) Schematic side view of the liquid cell used to observe nanobubbles and the region of view (top view) observed using TEM. (B) Schematic depicting the nanobubble nucleation pathway: heterogenous nucleation at the water-SiN_x interface due to the e-beam induced radiolysis and agglomeration of gaseous molecules at the solid surface. (C) The cumulative occurrence log of the nanobubbles observed during the experimentation. The improvement in the probability of occurrence due to the devised methodology can be seen after 9 attempts. (D) Snapshots of the nanobubbles observed during various experiments: (i) general view of the nanobubbles present on both the upper and the lower SiN_x window; (ii) excessive contamination observed in few experiments; (iii) nanobubbles exhibiting contrasting Fresnel fringes (dark and bright) due to their relative position with respect to the in-focus plane; (iv) isolated single nanobubble at least >150 nm away from the nearest nanobubble. Contaminations are also highlighted using yellow color in this frame.

nanobubbles morphology. The future studies should incorporate heater at region closer to the viewing region (nanobubbles) to attain inferable results and better understanding of the effect of temperature on the nanobubbles.

There have been handful studies of using LPEM, specifically SiN_x based, to study nanobubbles but the deviation in the instrumentation and operating conditions of the instruments, coupled with the different volumes of the used liquid cells, complicates the rather straightforwardly reported nucleation. For example, Huang et al. reported no nanobubble nucleation in pure water encapsulated in a 23 nl liquid cell using a 200 kV TEM,[35] on the other hand, Tomo et al. observed the nucleation in 23 s at high magnification of 300000× using a 300 kV TEM in a ~5.85 nl liquid cell.[34] In this study using 200 kV TEM for irradiating liquid thin film in an open liquid cell, we failed to nucleate and observe nanobubbles in our first 9 attempts (**Figure 2.3**(C)), either due to window damage after exposing the sample at high magnification for few tens to hundreds of seconds or no change in the *status quo* of the liquid even after long localized exposures, sometimes up to 2 hours at the same position at low magnifications.

In the successive experiments, we devised a new nucleating strategy in which the sample was first observed at low magnification (10,000-25,000×) for 30-40 minutes to increase the overall gas saturation levels in the liquid film (*Step 1*), followed by observing the sample at very high magnification (~500,000×) for 5-10 s using a highly convergent beam to create gas molecule clusters in the liquid (*Step 2*), and at last, observing the region at desired magnification for few seconds (10-20 s) to allow the bubbles to finally nucleate and grow (*Step 3*). *Step 2* is the most important step to nucleate nanobubbles, as the formation of gas clusters and its adsorption at the interface is critical for nanobubble nucleation at solid-liquid interface, as discussed in previous studies using AFM.[116] This strategy allowed us to successfully observe nanobubbles in 10/14 (~71.4%) of the successive experiments (**Figure 2.3**(C)). However, it is important to note that care needs to be taken while controlling the brightness of beam during *Step 3* as it may affect the nanobubble population; too bright beam and highly dense nanobubble clusters, sometimes even homogenously nucleated nanobubbles, are formed thus making the physics too complicated to perceive the fundamental dynamic behavior of the surface nanobubbles. Nonetheless, this strategy can be applied for applications where on-demand highly dense nanobubbles' clusters are required, such as in catalysis, etc. One such case of highly dense nanobubble nucleation is shown in **Figure 2.3**(D(i)) where more than 100 nanobubbles are present in ~1 μm^2 observation area.

In principle, the situations having fewer bubbles, as shown in **Figure 2.3**(D(ii-iv)), are preferred to understand the nanobubbles' dynamic behavior. This helps to define a clearer interaction and interplay these bubbles might have and the cause-effect understanding can be perceived effectively. Moreover, since the nanobubbles are nucleated on both the upper and lower SiN_x window surface, it is important to keep the focus plane between the two windows so that contrasting Fresnel fringes can be used to distinguish the relative position from the perceived overlapping nanobubbles in 2D TEM images.[34] For example, in **Figure 2.3**(D(iii)), the bubble exhibiting bright Fresnel fringe is in the region of overfocus, hence it is present on the upper SiN_x window and vice-versa. Lastly, as visible in all the frames of **Figure 2.3**(D), some contaminations of size range in order of $10^0 \sim 10^1$ nm are omnipresent, even though special care was taken while fabricating the liquid cell and all the fabrications were completed in the Class 1000 clean room facility. Therefore, we were convinced that it is irrelevant to look out for cases having no contaminations. For readers reference, the contaminations are highlighted using yellow color in the **Figure 2.3**(D(iv)).

2.3.2 Experimental observation

LPEM provides the opportunity to nucleate and directly observe nanobubbles and their interfacial phenomenon with high temporal and spatial resolution. Besides observing the nucleated nanobubbles, we also observed the disparity in the size of the nanobubbles depending on the fluence (or brightness) of the electron beam while using the developed nanobubble nucleation strategy (**Figure 2.4**). When the sample was irradiated with a bright electron beam (high fluence) during *Step 3* of the nucleation strategy, we observed dense clusters of heterogeneously nucleated nanobubbles and a few homogenously nucleated nanobubbles, as shown in **Figure 2.4**(A). Moreover, the size of the nucleated nanobubbles was small with 25-75 percentile of the nanobubbles falling within ~11-25 nm contact radius range ($contact\,radii = \sqrt{area/\pi}$). The observed mean and median values for the contact radius were 19.5 nm and 17.5 nm, respectively, as shown in **Figure 2.4**(C). On the other hand, when the sample was irradiated using a weak electron beam (low fluence), the number of nucleated surfaces nanobubbles were much lower, however, the size of the bubbles was larger i.e., the 25-75 percentile of the nanobubbles fell within ~28.5-39.5 nm contact radius and the mean radius being 34.6 nm, as shown in **Figure 2.4**(C). This observation was useful to obtain nanobubbles of required size and population density, which have been employed in various phases of this thesis. The brighter electron beam implies relatively higher oversaturation, which leads to the formation of multiple clusters of gaseous molecules on or near the solid surface, and since the gas molecules and clusters are present in abundance throughout the liquid, multiple nanobubbles nucleation can be achieved. The gas molecules present at the adjacence then contribute to the nanobubble growth locally. However, since the nanobubbles have already nucleated very closely to one another, the possibility of growth in their size was limited and hence, the nanobubbles observed using bright beam were lower in size. Moreover, a previous analytical study discussed that the equilibrium contact radius of an unpinned nanobubble is governed by the equation:[68]

$$L_e = \frac{L_c}{\zeta} \sin\theta$$

where, L_e is the equilibrium contact radius of the nanobubbles, L_c is the critical lateral extension, ζ is the gas oversaturation and θ is the contact angle. Since the L_c is constant for given liquid and pressure and assuming θ to be invariable (constant contact angle mode while growth), the equilibrium contact radius

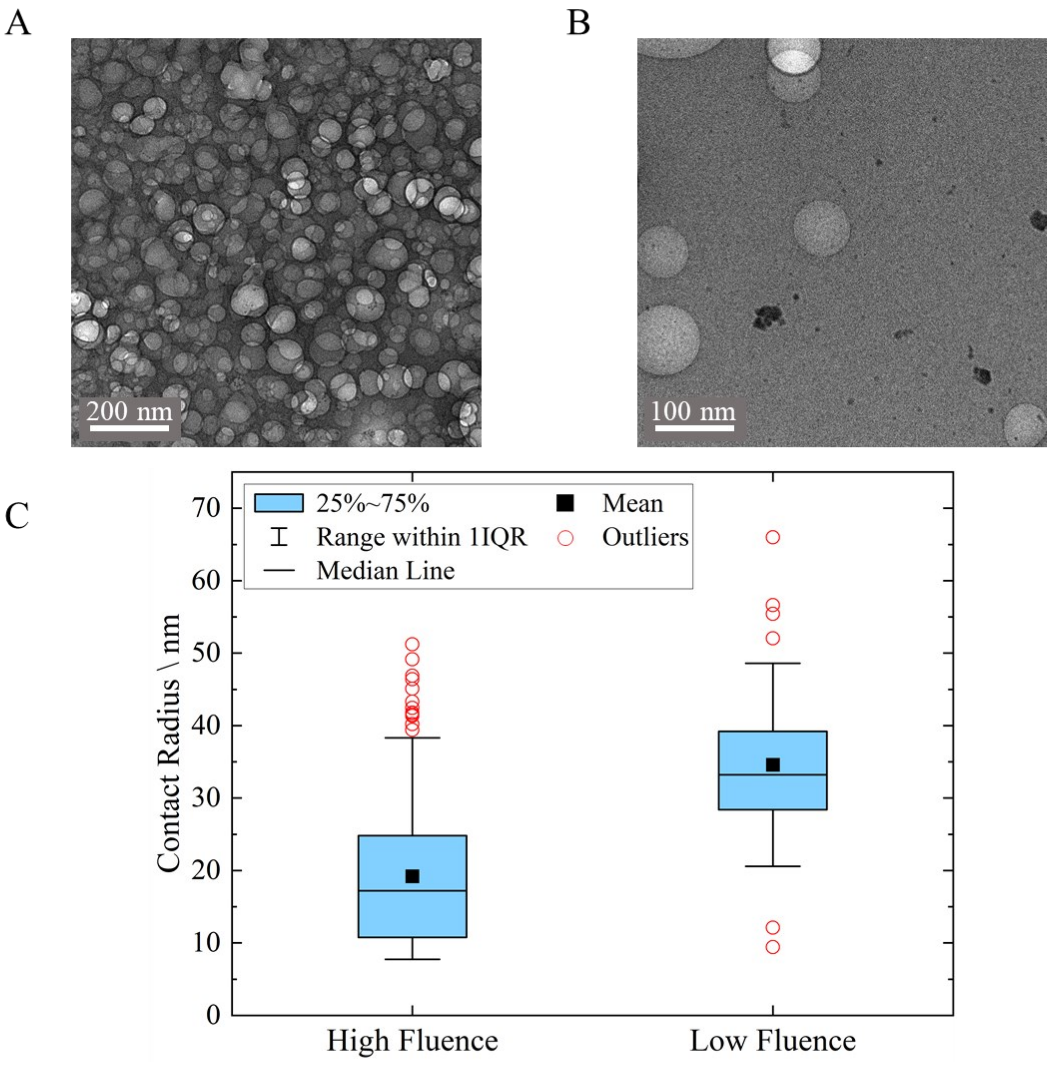

Figure 2.4 (A) Representative image for nanobubbles nucleated using bright beam in the *Step 3* of the devised nucleation strategy. (B) Representative image for nanobubbles nucleated using dull beam in the *Step 3*. (C) Box plots for the nanobubbles' contact radii distribution for the exposure using high fluence beam and low fluence beam. The lower-upper quartile region is shown in the box. The mean radius for the observed nanobubbles using high fluence beam is ~19.5 nm, whereas, using low fluence beam, the mean radius is ~34.6 nm.

would be smaller for higher gas saturation, hence smaller nanobubbles would be observed. On the contrary, in the case of a dull beam, the number of clusters formed would be sparsely distributed near the solid surface, and the excessive energy required for multiple nucleation cannot be supplied due to the relatively lower amount of oversaturation. The gas molecules in the liquid find it easy to contribute towards the growth of nanobubbles, rather than nascent nucleation. Hence, the size of the observed nanobubbles was higher as compared to the nanobubbles formed due to the bright beam.

By utilizing the weak beam to nucleate nanobubbles, we nucleated nanobubbles in the size range of ~30-40 nm contact radius and used them to study their interactions and interplay. **Figure 2.3**(D(ii)) and **Figure 2.4**(B) shows the representative images for such kind of nucleation. **Figure 2.5**(A) shows the TEM image of the two nanobubbles, named nbA and nbB, which are in closer vicinity to one another and do not have another bubble close to them. This provides an opportunity to understand the dynamic behavior, gas exchanges, and interplay between two nanobubbles. The image frame (**Figure 2.5**(A)) also shows nanobubbles with bright boundaries (highlighted using blue arrows), in contrast to darker boundaries of nbA and nbB (highlighted using red arrows).

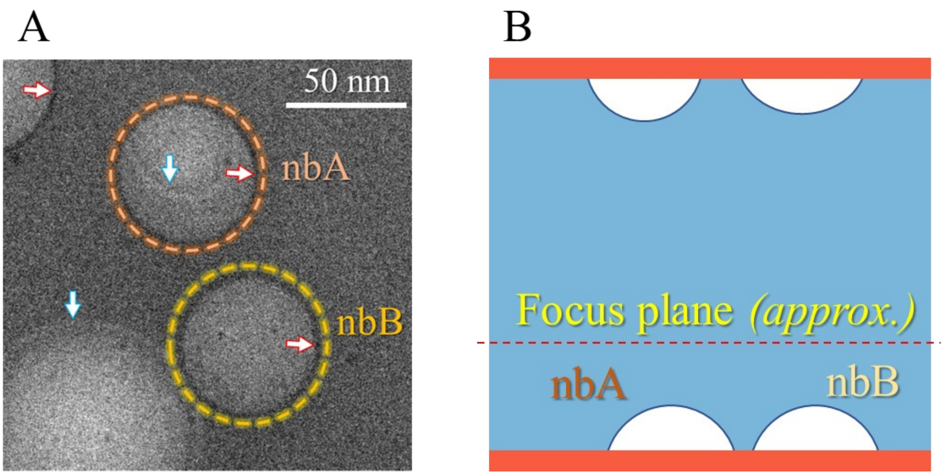

Figure 2.5 (A) TEM image showing the region of interest: nanobubbles A and B (in short: nbA and nbB). The initial distance between the three-phase contact lines of these nanobubbles is 20 nm. These surface nanobubbles are nucleated on the bottom SiN_x window. Few nanobubbles, present on the top SiN_x window, can also be seen in the TEM image. Red and blue bordered arrows are used to depict the bubbles at the bottom and top windows, respectively. (C) Side view representation of the TEM image in (B). The approximate focus plane during the imaging is also shown in the schematic.

These boundaries are the Fresnel fringes which can be used to estimate the relative position of the nanobubbles.[34] The bubbles with the brighter fringes are on the upper SiN_x window, and due to their certain distance from the in-focus plane (**Figure 2.5**(B)), are not considered in this study. Additionally, the gap between the nanobubbles on the adjacent SiN_x windows is too large for the nanobubbles to have strong interactions between them. The only probable effect bubbles present on the upper window may have is the variations in the path length of electrons due to the changing bubble height, and hence, varying gas oversaturation in the liquid. However, even this effect was not persistent as we observed instances where no change in the size of nbA was observed as the bubble on the adjacent window (bubble having bright Fresnel fringe) shrinks. One such instance to show the negligible interaction between the bubbles present on the adjacent windows is given in the supplementary information (**Figure S2**). Hence, the nanobubbles present on the adjacent SiN_x windows are assumed to be independent or, at most, weakly interacting in comparison to the nanobubbles on the same window with much less gap between them. Moreover, since the prime focus of the study was to understand the interplay between the neighboring nanobubbles, we chose the bubbles on the lower window having separation less than 20 nm.

The contact angle of the nanobubbles could not be measured from the 2D images and was assumed to be less than 90° from the gas side. This assumption agrees with previous studies which have clarified a definite distinction between the macroscopic and nanoscopic contact angles.[35,42,122] Since the bubbles were nucleated in-situ, the radiolysis and the sequential events leading to the *status quo* had already begun and succeeded for some time, hence the experimental observation began at the time t_0. The time-sequential information of these nanobubbles, before their coupled interplay, has been provided in the supplementary information (**Figure S3**).

The dynamics of the studied nanobubbles were observed with a high spatial and temporal resolution for nearly 18 minutes. **Figure 2.6** shows the variation of the mean radii of these nanobubbles for the observed duration. Initially, at 0 s ($t = t_0 + 0$ s; same nomenclature else specified otherwise) the initial contact radii of the selected nanobubbles nbA and nbB, was 31.5 nm and 27 nm, respectively. Both the nanobubbles were circular with very low deformity, as

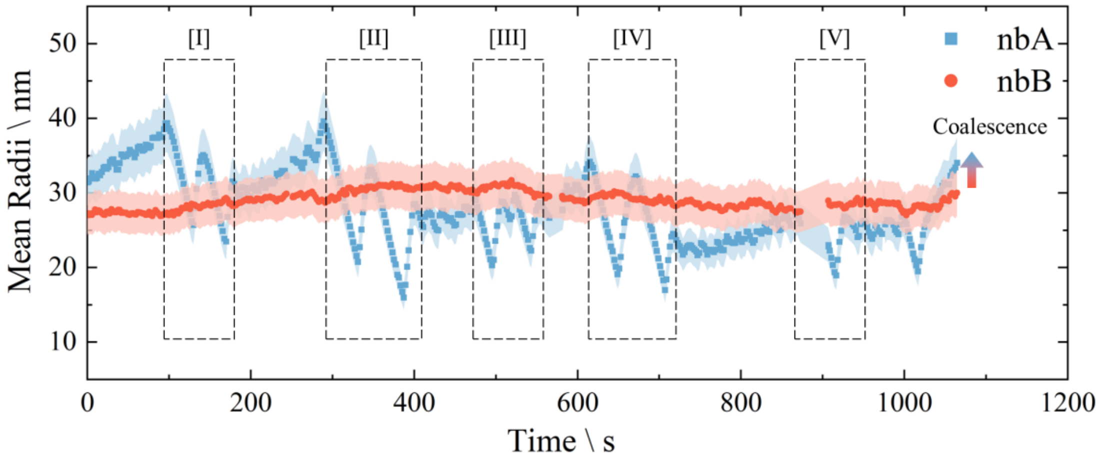

Figure 2.6 Variation of mean radii of nanobubbles nbA and nbB during the complete observation of ~18 minutes. nbA exhibits high variations in its radius and is deemed as unpinned nanobubble. nbB has low variations due to the strong pinning of its contact line. Series of shrink-growth behavior of nbA were observed in the study, as depicted by dotted rectangles [I] – [V]. The merging of nanobubbles was observed at 1065 s.

can be seen in **Figure 2.5**(A). As the e-beam irradiation continues, the nbA exhibits a gradual increase in its contact radius at 0.07 nm/s, whereas no increase in nbB's contact radius was observed. Consequently, the gap between the adjacent interfaces also reduced in the initial 100 s, owing to the monotonic growth in nbA's contact radius. The nbA then undergoes a series of rapid shrinkage and growth, before stabilizing, followed by a gradual increase in its contact radius. The radius of the nbB, on the other hand, did not exhibit such trends. Interestingly, such growth-shrinkage cycles in nbA were observed multiple times, as highlighted in **Figure 2.6**. One such cycle and the related dynamics are investigated in detail in the subsequent sections.

Figure 2.7(A-F) shows the time sequence of the observed phenomenon. On observing the region of interest for around 95 s, the nbA, unexpectedly, begins to shrink as its contact area reduces from 4890 nm^2 to 2094 nm^2 in around 34 s, as shown in **Figure 2.7**(G). **Figure 2.7**(A-C) demonstrates the shrinking of nbA. However, the nbB continues its trend of infinitesimal increase in the contact area. Further, the nbA regrows to the contact area 3870 nm^2 in next 12 s. It is evident that the nanobubbles, nbA and nbB, behave distinctly, as nbA is a freely growing-shrinking nanobubble whereas nbB exhibits strong pinning in its contact line. The pulsating of nbA and its effect on the contact line of nbB can also be seen in **Figure 2.7**(D-F). In our experimental study, nanobubbles were expected to grow due to oversaturation conditions under the continuous electron beam irradiation of the water.[34,71] However, pulsations were observed for the nbA as shown in **Figure 2.7**(G). Considering nbA is an unpinned nanobubble exhibiting growth, it should continue its growth due to the fact that unpinned nanobubbles have unstable equilibrium,[68] and hence, transform into a microbubble before detaching from the solid surface. However, the shrinkage was triggered due to its proximity with the nbB. Distinctively, the stability of nbB and its reluctance to exhibit similar dynamics can be accounted to the strong pinning of the contact line. The stability of the nanobubbles has, indeed, been attributed to the contact line pinning by several studies in the past.[68,122,139] The pinning behavior of the contact line might be due to any possible chemical heterogeneities, which can be present on the smoothest of surfaces.[42] In a similar context, a recent study has experimentally demonstrated the role of adsorbed gas layers on the surface, which exhibits solid-like rigidity, in limiting the mobility of micro-pancakes.[140] The presence of such adsorbed layers are unlikely to be observed by a TEM, however, they might be responsible for the stability of nbB.

For a better insight into the phenomenon, let us focus on the reasons that contributed towards the shrinkage and successive pulsations in the nbA's contact line. Because of the continuous e-beam exposure, the gas oversaturation in the irradiated region accumulates and the nbA grows due to its unpinned three-phase contact line (**Figure 2.6**), which can be perceived from the TEM images. However, nbB is also expected to grow due to the oversaturation and the gas influx, which cannot be perceived in the 2-D TEM images due to its

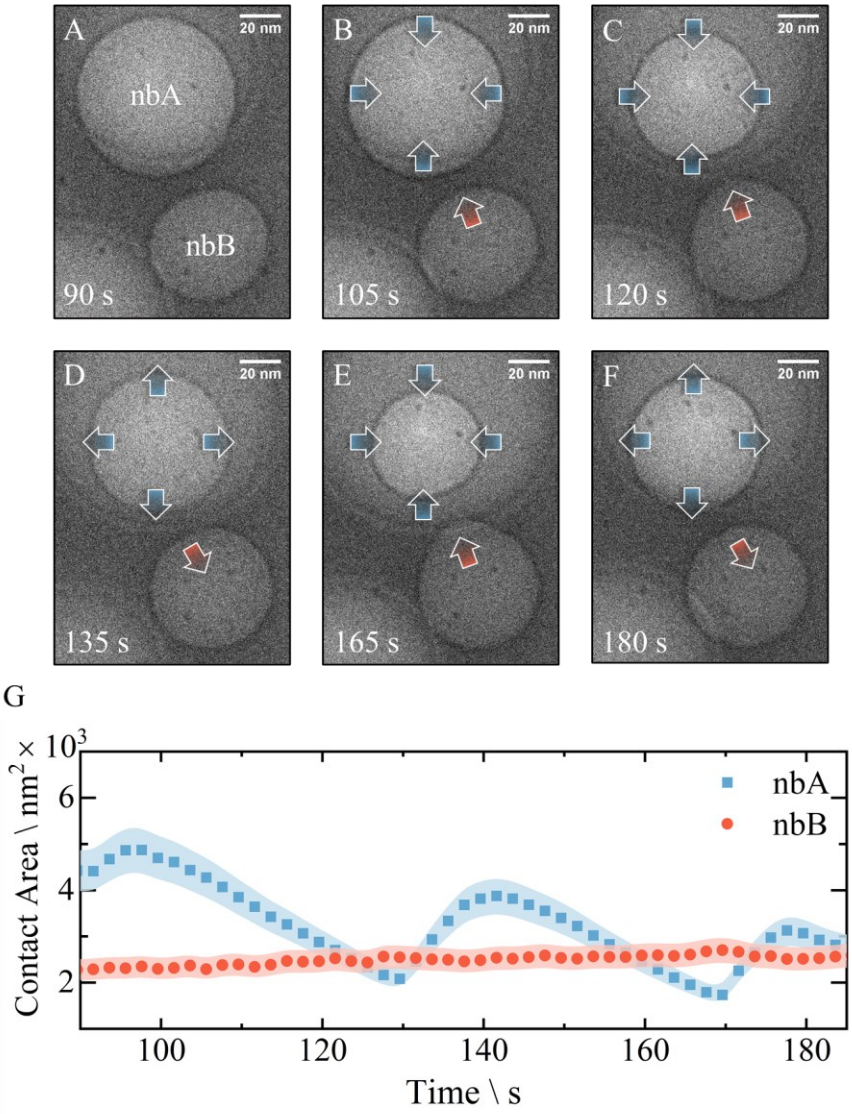

Figure 2.7 Time sequence images demonstrating the interfacial interplay between nanobubbles observed using TEM. (A) TEM image showing the state of nanobubbles at t = 90 s. (B,C) The shrinking of nbA induces elongation in nbB, directed towards nbA. (D) The growth of nbA pushes the adjacent interface of nbB. (E,F) nbA and nbB demonstrating the pull-push phenomenon, induced due to the grow-shrink mechanism of nbA. Blue and Red arrows show the direction of the interface movement for nbA and nbB, respectively. (G) Temporal variation of nanobubble contact area for nbA and nbB.

pinned three-phase contact line. In an analytical study, Lohse and Zhang suggested that for a pinned nanobubble, the equilibrium radius varies inversely with the oversaturation, ($\boldsymbol{R_e = L_c/2\zeta}$, where $\boldsymbol{R_e}$ is the equilibrium radius, $\boldsymbol{L_c}$ is the critical lateral extension, and $\boldsymbol{\zeta}$ is the gas oversaturation), hence an increase in the oversaturation will compel the nanobubble to swell, thus increasing in its height and effective volume.[68] The schematic of the phenomenon is given in the **Figure 2.8**(A), where any increase in the size of nbA is accompanied by an increase in height of nbB, and vice versa.

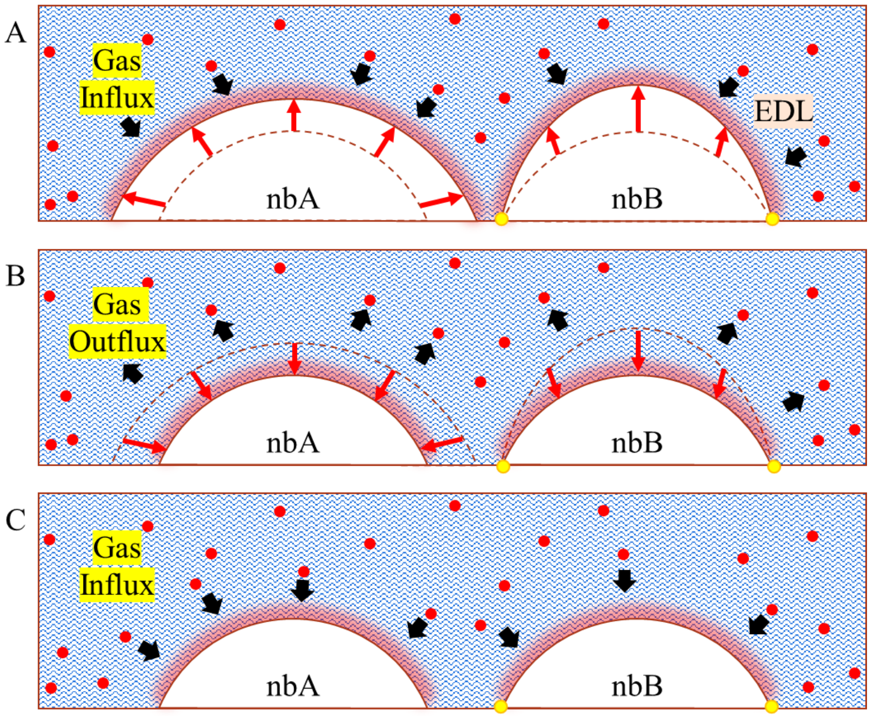

Figure 2.8 Schematic of the observed nanobubble dynamics. (A) Due to the oversaturation, the bubble nbA and nbB grows. The gas flow direction is depicted by black arrows whereas the interface movement is depicted by red arrows. (B) The shrinkage in the nanobubbles in triggered by the cumulative effect of EDL, liquid thin film stability and the dynamic equilibrium of the nanobubbles. (C) As a reaction to the gas outflux in (B), the nanobubble starts to grow again after inhibiting further shrinkage.

Since the nanobubbles are encompassed in the EDL due to their charged interfaces, the repulsive interaction between the nanobubbles' interface increases as their separation decreases and triggers the shrinking in the nbA (**Figure 2.8**(B)). Moreover, the relative positioning of these nanobubbles also promotes the shrinkage effect in the nanobubbles. As the nbA expands towards nbB and the distance between the nanobubbles' three-phase contact line reduces, the presence of nbB and the thin film formed between the nanobubbles hinders the further expansion of nbA. The stability of thin-film and the nbA's intrusion into the thin film not only suppresses the growth of the nbA, but also leads to repulsions between the two nanobubbles due to their interacting double layers. Additionally, since the nanobubbles are always in dynamic equilibrium with the gas saturation in their vicinity,[27] any overshoot in their size due to the inertia in interfaces' motion may destabilize this equilibrium which may impart dynamic behavior to balance the gas saturation. Therefore, the nanobubbles begin to shrink after its trigger and the gas outflux from the nanobubbles increases. As a reaction to this gas outflux, the nanobubbles shrinking deaccelerates and then start their growth (**Figure 2.8**(C)) as they surpass the equilibrium and successively exhibit undulating behavior, as shown in **Figure 2.7**(G), until the equilibrium is established.

2.3.3 Anisotropic depinning in nanobubbles

The unpinned nbA undergoes a series of grow-shrink undulation before stabilizing and following its usual growth pathway. Further, these undulations in nbA induced deformity in nbB, which tends to elongate the nbB. **Figure**

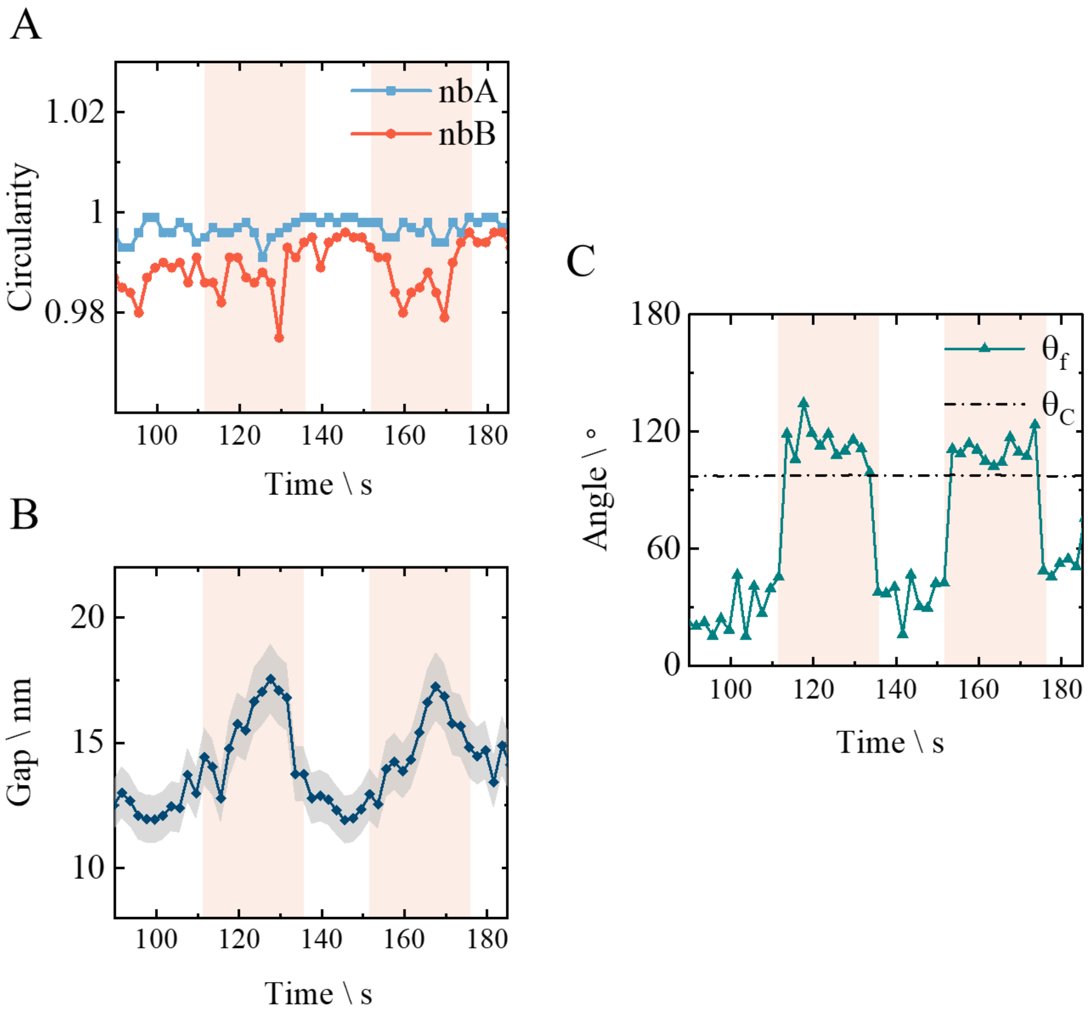

Figure 2.9 Anisotropic depinning of nanobubbles. (A) Temporal variation of circularity for nanobubble nbA and nbB. (B) Variation of the gap between the nanobubbles. (C) Feret angle and the angle formed by joining the centroids of nbA and nbB. The shaded region in (A), (B) and (C) highlights the directional deformation of the nbB induced due to nbA.

2.9(A) shows the variation of circularity of the studied nanobubbles. Here, circularity is defined as 4π times the ratio of area (A) to the square of the perimeter (P), i.e., $Circ. = 4\pi(A/P^2)$. The circularity value of 1 indicates a perfect circle, whereas any decline in its value indicates the extent of elongation. The reduced circularity of nbB demonstrates its deformation, whereas the circularity of nbA continues to be closer to 1. It was observed that while nbA continued to maintain its circular form due to its unpinned interface, nbB deformed asymmetrically. Moreover, the undulations in the nbA also lead to the variation in the distance between their three-phase contact lines, i.e., the gap varies between 12 nm to 18 nm as shown in **Figure 2.9**(B). We also measured the feret angle for nbB to understand the angularity and directionality of the deformation in nbB. Feret angle is the angle between the line segment joining two farthest points in an enclosed entity with the horizontal line and is helpful in determining the angularity of elongation (or distortion) in any enclosed figure. In **Figure 2.9**(C), the feret angle was observed to fluctuate in two discrete ranges, (a) 15°-50°, and (b) 100°-135°. This demonstrates a strong association between the pulsation in nbA and deformation in nbB. For the shrinking phase of nbA, the feret angle remained between 100°-135°, thus confirming that nbB's interface is pulled directionally towards nbA due to its shrinking. Similarly, for the growing phase of nbA, the feret angle remained between 15°-50°, demonstrating push from the growing nbA's interface. The variation of feret angle, either parallel or perpendicular to the line joining the centroids of nanobubbles reassures the coupled behavior of the nanobubbles' interfaces. The measured parameters plotted in **Figure 2.9**(B-C) are shown in the supplementary information (**Figure S4**).

The contact lines of these bubbles were traced using an edge detection algorithm to further understand the deformation and the depinning of the nbB. Interestingly, it was observed that the contact region of the nbB, farther from the nbA, remained completely pinned to the surface during the whole phenomenon, as demonstrated in **Figure 2.10**. **Figure 2.10**(A) shows the contact boundary of the nanobubbles observed during the first shrink-grow cycle, i.e., at time 111 s, 125 s and 135 s. Pulsating of nbA and the consequent depinning of the adjacent interface of nbB, highlighted by blue and yellow arrows, respectively, can be seen in **Figure 2.10**(A). A similar phenomenon of selective depinning was observed again at 154 s to 175 s into the observation, as shown in **Figure 2.10**(B). Previously, the distortions in nanobubbles' pair were also observed by Park et. al, however, they observed it specifically in the larger nanobubble exhibiting growth due to the Ostwald ripening.[36] Moreover, they did not observe the asymmetrical depinning behavior in their experiments. In addition, we also observed the pushing of nbB's interface when the nbA enters the growth regime.

The probable side views of the nanobubbles and the observed anisotropic depinning is shown in **Figure 2.11**(A), where any increase in the size of nbA is accompanied by an increase in height of nbB, and vice versa. The observed anisotropic depinning coupled with the shrinking of the nbA can be explained

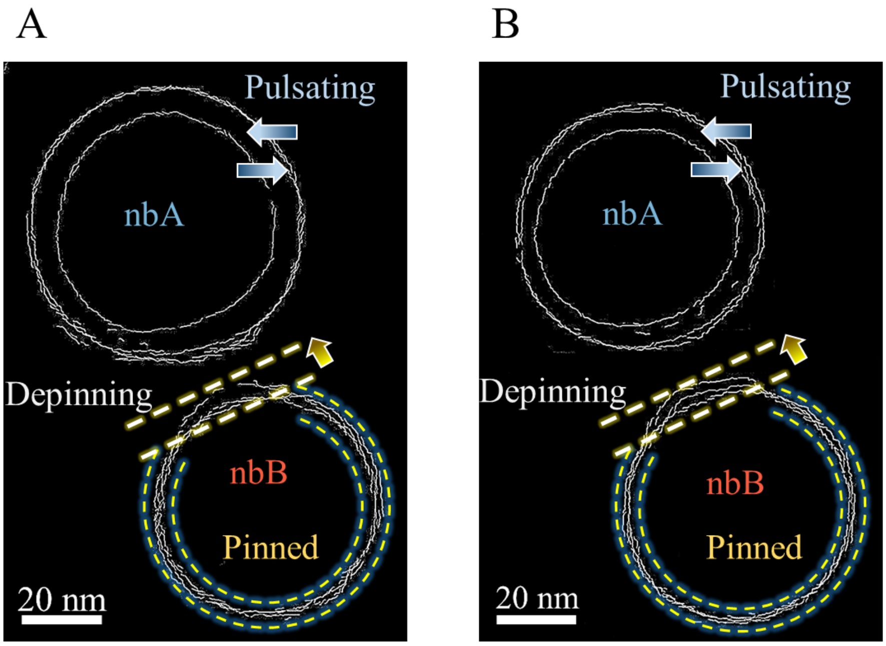

Figure 2.10 (A) Contact line of the nanobubbles traced for the first shrink-grow observation at the time: 111 s, 125 s and 137 s. nbA shows the pulsating behaviour, while the nbB shows depinning along edge adjacent to nbA and pinning along the opposite edge. (B) Contact line of nanobubbles for second shrink-grow observation at time: 155 s, 165 s and 175 s. Similar anisotropic depinning is observed in nbB.

as follows (**Figure 2.11**(B)): the simultaneous shrinking of nbA and nbB leads to gas outflux in their peripheral region. The gas concentration is expected to be higher in the region between the nanobubbles near the solid interface, due to the damped diffusion of gas molecules near the interfaces.[103,136] As the contact line of nbA is moving away, these gas molecules then transmit to the pinned nbB, resulting in the growth of its partial portion. Nanobubbles are in dynamic equilibrium with the gas molecule in the liquid and the gas outflux is balanced by the influx through nanobubbles' interfaces.[27] This, in general, does not affect depinning. However, asymmetric distribution of gas oversaturation around a pinned nanobubble leads to anisotropic depinning of its three-phase contact line. Interestingly, the pinning force at the interface for the remaining region was observed to be strong enough to keep the surface pinned without compensating for surface tension. In addition, the interface farther from the region between the nanobubbles does not experience any dramatic changes in the relative gas saturation, and hence, the remaining three-phase contact line of the nanobubble remains pinned, as shown by the yellow color in **Figure 2.11**(A). The schematic in **Figure 2.11**(B) also weighs the factors responsible for the observed anisotropic depinning, where the increased local oversaturation around the pulsating nanobubble is responsible for selective depinning of a strongly pinned nanobubble.

Similar phenomenon was observed on multiple occasions while observing other nanobubble pairs, however, the presence of more nanobubbles at relative adjacence seems to impact the time scales and bubble pulsations in the phenomenon. The time sequence imagery and brief description of such events have been provided in the supplementary information (**Figure S5, S6,** and **S7**), where deformation in the three-phase contact line of the nanobubbles could be observed due to the shrinkage or growth of adjacent nanobubble. On observing a nanobubble pair at a lower electron beam intensity, we found the anisotropic depinning to be lower in magnitude due to the lower relative oversaturation at a low electron dose environment, as shown in the supplementary information (**Figure S5**). This reassures the role of localized oversaturation on the anisotropic depinning of pinned surface nanobubbles. However, the pushing of nbB's three-phase contact line due to the pulsating nbA needs to be discussed further while considering the nanoscale forces at play.

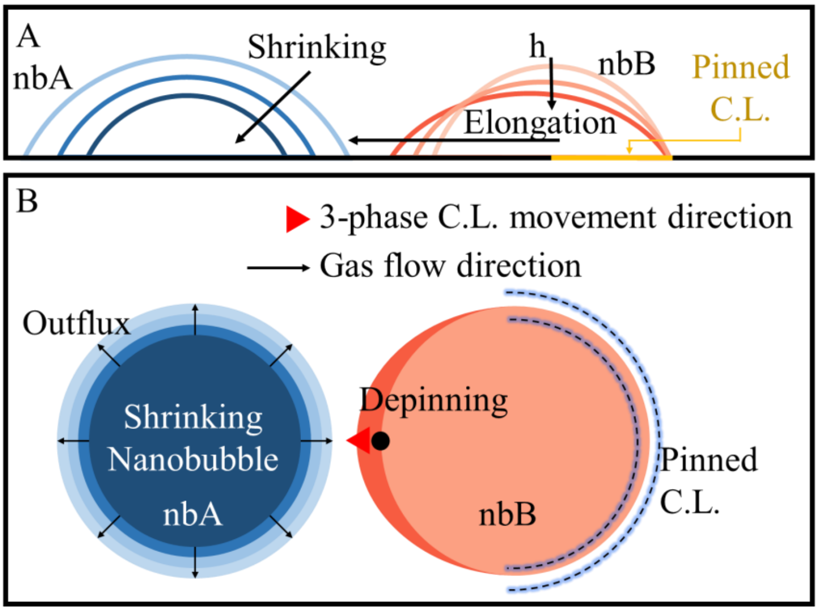

Figure 2.11 (A) Schematic of the probable side view of the nanobubbles shows the shrinking of the nbA initiates the anisotropic depinning of nbB's three-phase contact line. (B) Role of increase in localized gas concentration in the anisotropic depinning of surface nanobubbles. The lighter blue region around the nbA shows the level of high gas concentration.

The thin liquid film between the nanobubbles, with varying thickness of 6-20 nm, was observed to be stable experimentally. Moreover, the nanobubbles interact across this thin film, which causes the pull-push phenomenon between the nanobubble's interfaces. Nanobubbles' surface, or in general all gas-water interfaces, is charged negatively due to the strong adsorption of hydroxide ions,[141,142] which prompts an electric force field around their interfaces. This electric field influences the ion distribution around a nanobubble, which leads to the generation of diffused EDL around its interface.[128] The double layers of two individual nanobubbles in the vicinity lead to the interactions between their interfaces due to the accumulation of counterions at the peripheral region. Due to the likeness of the interfacial charges, the double-layer interaction is repulsive in nature. In addition, the van der Waals interactions are accounted for the attractive behavior and are dominant as the distance between the bubbles reduces. Hence, cumulatively, the nanobubble pair exhibits attractive-repulsive behavior along with their interfaces, which is a factor of the separation distance between the nanobubbles, size of the bubbles, surface charge, and the physical properties of the nucleating medium. These interactions are analogous to the colloidal particles interacting in the bulk medium,[143] except that the nanobubbles are also coupled via the gas exchanges (mass diffusion) between them. Further, the hemispherical shape of the bubbles, along with their soft interfaces and interfacial pinning further increases the complexity in the quantifiable modeling of such phenomenon, however, the nature of interactions can be discussed qualitatively. The Debye-Hückel constant, which is proportional to the ionic concentration of the liquid, plays a critical role in determining the interactive behavior between the nanobubbles. It is important to note here that even though no salt was added in this study, the ionic concentration in the water is affected by the electron beam dose rate. For the lower electron dose rates, the pH of the water remains unaffected, but at higher electron dose rate values, the pH of the water reduces significantly,[66] implying an increase in the ionic concentration of the H_3O^+ ions. For the typical TEM dose (10^8 Gy/s), the pH of the water is expected to lie between pH 4-5.[66] Since the Debye length (κ^{-1}) varies inversely with the ionic concentration (φ_∞) i.e. ($\kappa^{-1} \propto 1/\sqrt{\varphi_\infty;}$), the increased H_3O^+ concentration, hence the thin double layer, may be the reason for pull-push behavior between the nanobubble interfaces, which can be justified by the feret angle variation between 15°-50° and 100°-135° in **Figure 2.9**(C). In the case of the pH value closer to the neutral cases (pH~7), the double layer would be much thicker, and the interaction is expected to be repulsion dominant. Moreover, the nature of gas molecules dissolved in the water is highly unlikely to affect the charge at the interface, except for CO_2. Most of the gases dissolved in water, such as N_2, O_2, He, Ar, CH_4, H_2, etc are non-polar and inert in nature and have no impact on the pH of water.[144] However, CO_2 is arguably known to reduce the pH of the water and impart a negative charge to the water-gas interface.[145] Hence, the concentration of CO_2 in water will in fact affect the charge concentration, Debye-Hückel constant, and the strength of EDL, which may impact the pull-push phenomenon.

2.3.4 Weakened repulsions and coalescence

In our experiment, we observed the coalescence of nanobubbles after nearly 18 minutes from the beginning of the observation (t_0). During the observation, the nanobubble pair underwent multiple pull-push and anisotropic depinning events, as shown in **Figure 2.6**. It is important to note here that the bubbles have existed for a longer time as they were already nucleated when the observation was initiated. Recollecting the derogatory electron beam conditions and the fluctuation in gas saturation conditions caused by them, our observation reassured the long-term existence of nanobubbles and their metastability. In the due course, we observed the coalescence of the nanobubbles. The snapshots of nbA and nbB before and during merging are shown in **Figure 2.12**(A-D). As discussed in the previous section about the EDL, the bubbles should demonstrate hesitance to merging, due to the attractive repulsive equilibrium at a lower separation gap. That was, indeed, the reason for the observed longevity of nanobubbles. However, the phenomenon exhibited by nanobubbles is intricate and depends on the various physio-chemical phenomenon, which may be transient and changes as the experimental parameters change. Although the formation of EDL hinders the coalescence initially, the continuous exposure of the sample to the electron beam and the accumulative build-up of gas saturation may be the reason behind the observed coalescence. A previous study on the effect of gas concentration in liquid on the bubble coalescence also points towards the increased coalescence.[146] The accumulation of gas molecules and their steric effects might be responsible for

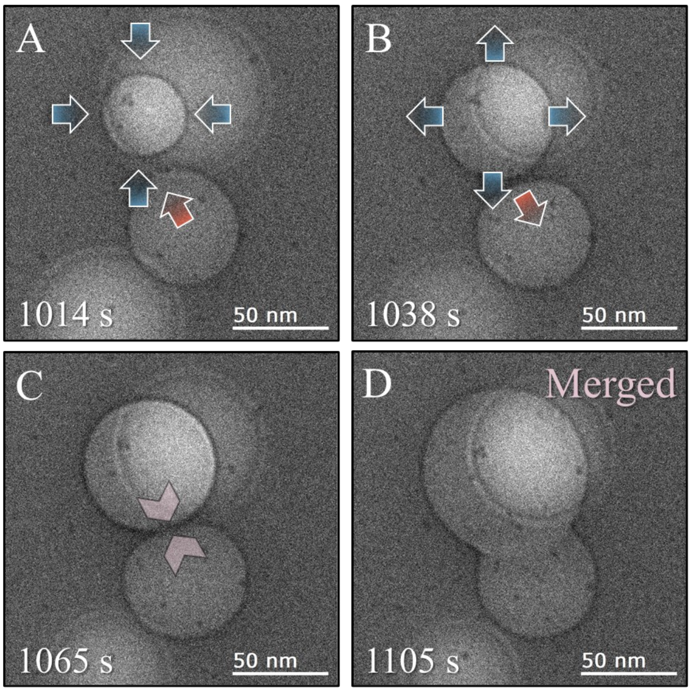

Figure 2.12 Time sequence snapshots of nbA and nbB for the time (A) 1014 s; (B) 1038 s; (C) 1065 s and (D) 1105 s. The blue and red arrows in (A) and (B) show the direction of the interface movement in nbA and nbB, respectively, whereas the pale markers in (C) shows the initiation of merging. The bubble merged after 18 minutes of observation. The shape of the bubble after merging verifies that the observed bubbles are surface nanobubbles.

the displacement of ions from the interfacial region of nanobubbles. This is further supported by the higher steady-state concentration of hydrogen molecules in the radiolysis of water,[66] and the high diffusion coefficient of H_3O^+ ion.[147,148] The resultant may be a weaker EDL and reduced repulsive force between the nanobubbles. Additionally, few previous studies also suggested that the gas molecules' number density is generally higher near the liquid-solid interfaces, owing to strong gas-solid interactions.[149,150] This is further favored by the inherently higher number of molecules between the neighboring bubbles' diffused interfaces.[36,121] The increased gas saturation may play a vital role in suppressing the repulsive behavior, which leads to the merging of the nanobubbles. Interestingly, as shown in **Figure 2.13**(A), the gap between the nanobubbles' three-phase contact line, which in the earlier stage of interactions fluctuated in the range of 12-20 nm, also reduced to 5-10 nm range before merging, which is another indication of the reduced magnitude of repulsive behavior. The decreased repulsive behavior as a function of irradiation time is also evident from the reduced center-to-center distance between the nanobubbles, as shown in **Figure 2.13**(B). The nbA was observed to move towards the pinned nbB while pulsating as their center-to-center distance reduced from 77 nm to 64 nm while the whole observation was carried.

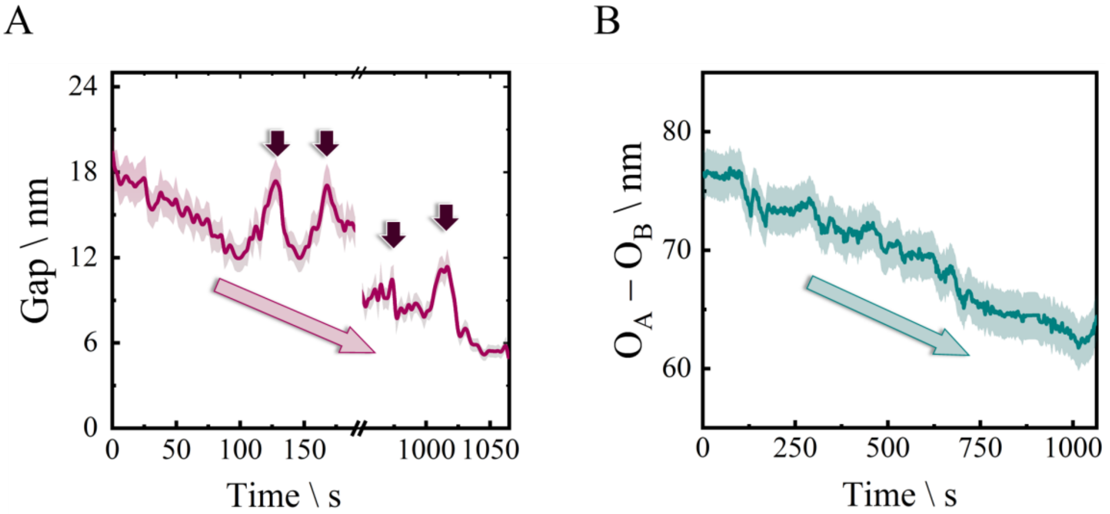

Figure 2.13 (A) Variation of gap between the nanobubbles for time 0 s – 180 s (initial observation) and 950 s – 1065 s (before merging). The black arrow shows the increased gap due to the shrinking of nbA. The reduced repulsions between the interfaces have led to a decrease in the overall gap between the bubbles. (B) Variation of center-to-center distance between the nanobubbles for the complete 18 minutes of observation. The reduced repulsions between the nanobubbles due to the accumulative oversaturation increase are evident as the center-to-center distance decreases monotonically for the whole observation.

2.4 Summary

In this chapter, the methodology was devised to nucleate nanobubbles with differential sizes by controlling the electron beam fluence in the liquid phase electron microscopy experiments. Further, this work also provided insight into the nanobubble dynamics and their interplay with high spatial and temporal resolutions for long durations. Previously, the counterintuitive longevity of surface nanobubbles had been long attributed to the contact line pinning, however, this study contributed towards expanding the existing knowledge by experimentally demonstrating the existence of surface nanobubbles with and without contact line pinning. In addition, our work also captured the anisotropic depinning of the pinned nanobubbles and revealed the role of localized gas oversaturation in this asymmetric interfacial phenomenon. The pulsations in the unpinned nanobubble created an environment with fluctuating gas concentration and were responsible for the anisotropic depinning. Further, this study highlighted the effect of the ionic concentration on the coupling of the nanobubbles' interfaces and the pull-push behavior, which was attributed to the EDLs encompassing the nanobubbles and their successive interactions. The present study also revealed the role of accumulative gas saturation in suppressing the EDL's repulsive interaction, which reduces the nanobubbles' reluctance to merge. These findings not only provided insight into the dynamic nanobubble behavior but also explained the importance of EDL in rendering the longevity to nanobubbles, which in some cases have been a few days.

Future studies on this subject can be on developing the quantitative model to find the relation between the oversaturation and the nanobubble size and population density. Further, controlling the gas oversaturation and ionic concentration in the liquid by improvising the experimental methods needs to be carried out for an in-depth understanding of the observed phenomenon. The nucleation methodology devised in this chapter will serve as a key to nucleate on-demand nanobubble size and population in **Chapter 3** and **4**. Nonetheless, this work captured the dynamic phenomenon of nanobubbles, which have so far been visualized through the MD simulation lens.

3

Nanobubble Coalescence[‡]

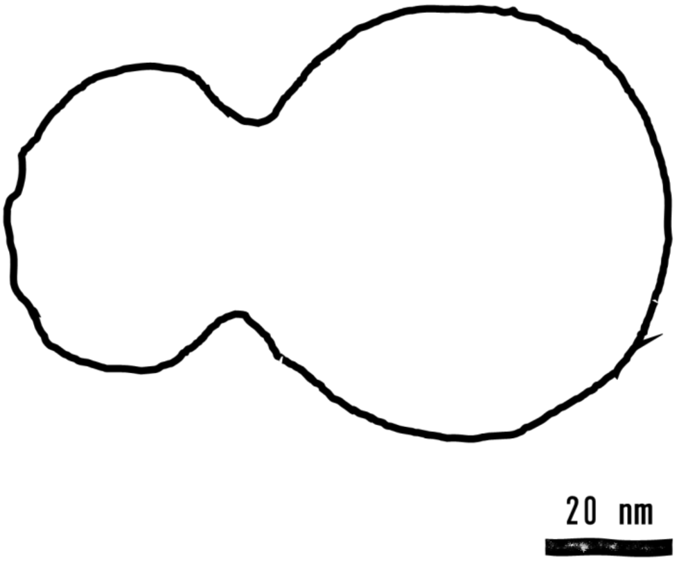

[‡] Adapted with permission from "*Nag, S., Tomo, Y., Takahashi, K. & Kohno, M.* Mechanistic Insights into Nanobubble Merging Studied Using In Situ Liquid-Phase Electron Microscopy. *Langmuir* 37(2), 874-881 (2021)" DOI: https://doi.org/10.1021/acs.langmuir.0c03208 Copyright © 2021, American Chemical Society.

In this chapter, we studied the coalescence phenomenon in surface nanobubbles using the in-situ liquid-phase electron microscopy technique. The electron beam environment was systematically controlled to suppress rapid bubble dynamics and nascent bubble nucleation. Our study reveals that the merging of closely positioned surface nanobubbles is initiated by gradual localized changes in the physical properties of the region between the adjoining nanobubbles' interfaces. The observed phenomenon is discussed based on the perception: localized liquid density gradient and bridge formation for gas exchange between the nanobubbles. In this study, we found that the merging of the stable nanobubbles is initiated by the deposition of gas molecules and the formation of a thin gas layer. Further, we also observed that the kinetics of deposition and formation of the thin film is majorly governed by the degree of oversaturation.

3.1 Background

Bubble coalescence[121,151] is a very common process in nature and industry,[152,153] and has attracted major research interest in the past due to its applications and relevance in domains related to mass transfer,[154,155] catalytic reactions for energy conversion,[156] electrolytic processes,[157] and various other electrochemical systems.[158] The bubble coalescence process also affects various thermal-fluid engineering aspects, such as flow dynamics inside confined channels,[159] slug flows,[160] flows inside porous media,[161] and heat transfer enhancement during the two-phase cooling due to rewetting of the heater surface and turbulent mixing effects.[162] These applications have motivated the researchers to understand basic questions about the evolution of bubbles, i.e., interfacial interactions, and coalescence.

Conventionally, bubble coalescence is known to occur in three stages: (*i*) collision of bubbles' interfaces as they grow, followed by (*ii*) drainage of thin film between the bubbles' interfaces, and finally, (*iii*) film rupture leading to the formation of a larger bubble.[163] The stability of the thin film between the bubbles defines the rate of bubble coalescence.[152] In general, bubbles have the natural tendency to merge in order to reduce their surface energy, however, the mutual attraction and repulsions between the bubbles' interfaces acting due to the *vdW* and *EDL* interactions are known to govern the slowness or the swiftness of the bubble coalescence process.[152] In the past, bubble coalescence has been actively studied for both micro as well as macro scales, however, little is known about the bubble coalescence at the nanoscale, in particular, bubbles of size less than 100 nm. As the electronic components and point of care healthcare devices are thrusting towards miniaturization,[164] it is important to understand the coalescence process at the nanoscale because of the richness in mechanisms acting at nanoscale coupled with the amplified effects of surface and interfacial forces, that may give rise to a new phenomenon.[165] Understanding of bubble coalescence at the nanoscale has also been of prime importance for the advancements in emerging technologies like rapid heat dissipation, water desalination, self-cleaning surfaces, biomedical imaging, and targeted drug delivery.[166–168] Most of the existing experimental studies of nanobubble merging have been carried using the AFMs,[122,169,170] which, due to its slow scan speeds conceals the dynamic behavior of the process. Few other studies have reported the use of advanced optical microscopy techniques to capture temporally resolved merging process,[120,171] however, the poor spatial resolutions limit its capability to provide insights into the merging. LPEM is the most sought-after technique to observe nanobubbles with high temporal and spatial resolution. In past, researchers have used GLCs and SiN_x liquid cells to study the nanobubble dynamics and observed distinct nanoscale behavior.[35–37,73] Huang et al. studied the dynamics of hydrogen nanobubbles in KLH protein solution using SiN_x-LC based LPEM and distinguished the growth dynamics into 5 phases: (i) gas layer nucleation, (ii) single bubble expansion, (iii) multiple bubble interaction, (iv) nanobubble contact, and (v) nanobubble merging.[35] Shin et al. studied the evolution of nanobubble pair using GLC based LPEM and observed Ostwald ripening nanobubbles and coalescing nanobubbles for 10 nm diameter nanobubbles (~50 s).[37] Later, Park et al. focussed on the merging and found that the relative size among the nanobubbles is the main driving force for the distortion and merging.[36] The aforementioned studies observed the phenomenon to be unexpectedly slow. Bae et al. used GLC based LPEM to study nanobubble dynamics in aqueous surfactant solutions.[73] The observations in their study were at least 1 order of magnitude faster than the previous reports. Although there have been a handful of studies on the dynamics and merging of nanobubbles, a focussed study on the coalescence dynamics and the changes in the thin film and bubbles' interfaces during the coalescing process is vital to provide insights on the role of factors such as gas oversaturation and other surface characteristics.

Therefore, in this chapter, a focused study on the merging of two selected surface nanobubbles using LPEM is presented. By applying the image processing technique to the TEM images, the interfacial region between the nanobubbles was evaluated. The analysis was based on the local image intensity, as the local intensity and image contrast of the TEM image reveal information on the mass and thickness of the specimen.[172] During the observation, the interfacial distance between the nanobubbles, i.e. the thin film thickness was also tracked before initiation of merging. Further, the mechanism of merging is then proposed, and mechanistic insights are provided. The present study also outlines the effect of gas oversaturation on the merging dynamics of nanobubbles. The study was also expanded for the simultaneous coalescence of multiple nanobubbles and was found in agreement with the proposed mechanism. We believe that understanding the merging phenomenon at the nanoscale will aid in controlling and engineering the surface properties of surfaces submerged in liquids.

3.2 Experimental Equipment and Methods

3.2.1 Experimental equipment

For details on the experiment equipment, kindly refer to **section 2.2.1** of the previous chapter, however, briefly, the experiments reported in this chapter were also carried using the SiN_x liquid cell electron microscope system (Poseidon Select, Protochips Inc., U.S.A.). The spacer height used was 150 nm and the e-chips were assembled in the cross-configuration. The e-chips were also cleaned using a glow discharge plasma reactor (PIB-10, Vacuum Devices, Japan) before their assembly in the liquid cell holder, mainly, to remove any organic contaminations and to provide hydrophilicity to the e-chips for accommodating thin liquid film without any retraction. After assembling, the liquid cell was kept in a vacuum pumping station (10^{-3}~10^{-4} Pa) and water was allowed to flow between the e-chips for ~12 hours to ensure its integrity before loading into the TEM column. After loading the sample into the TEM, the flowing water was allowed to complete one cycle in order to eliminate any air cavities in the liquid cell. All the observations were carried at room temperature without any flow inside the liquid cell.

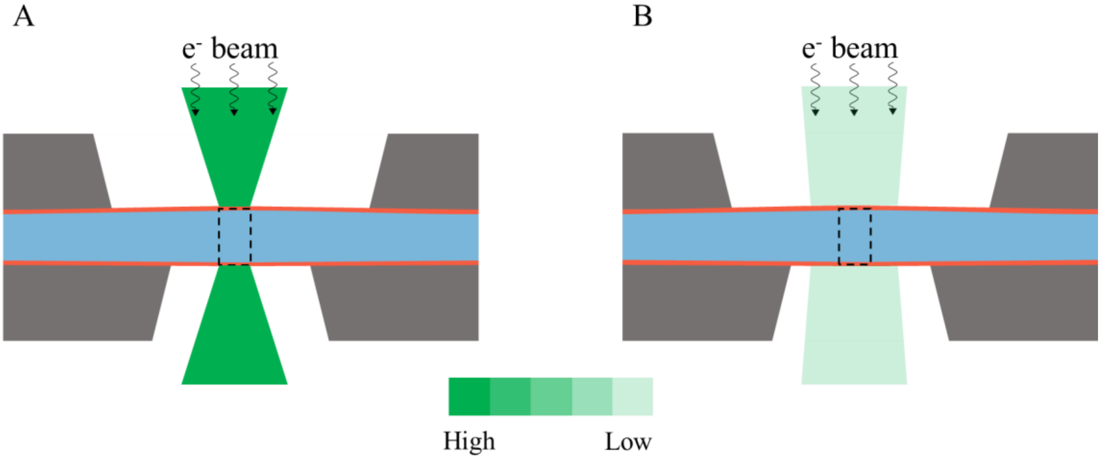

Figure 3.1 Schematic representation of (A) converging beam and (B) diverging electron beam irradiated on the sample using the TEM.

The samples were imaged in a TEM (JEM-2100Plus Electron Microscope, JEOL Ltd., Japan), operated at an accelerating voltage of 200 kV. This TEM has a thermionic electron emission source (LaB_6 filament), whose current density is three orders less than the field emission electron sources, and hence has minimal beam effects on the sample.[37] In addition to this, the study was specifically carried using a higher spot size (Spot Size: 2-3). The spot size is controlled by the condenser lens of the TEM and increasing the spot size reduces the beam convergence as well as the beam current density irradiated on the sample, as demonstrated in **Figure 3.1**. This is advantageous when samples are susceptible to high electron beam effects and avoids localized beam damage on the liquid cell. Hence, a higher spot size sustains observation for a longer time duration. The image acquisition was done using a CMOS camera (Rio 16, Gatan Inc., U.S.A.) at 1K resolution and 40 fps.

3.2.2 Imaging and analysis

Since the TEM image consists of varying grey levels depending on local mass or local thickness in the sample, using a systematic image processing methodology becomes highly relevant. Due to the quasi-static nature of the observed phenomenon, the video, initially acquired at 40 fps, was rendered at 8 fps (play speed 1x) for trouble-free data handling. MATLAB was used for image handling, image pre-processing, and nanobubble edge detection. Firstly, the TEM image, initially in RGB array (1024×1024×3) was converted to greyscale (1024×1024×1) for easier implementation of the subsequent operations. The histogram equalization operation was then applied to the greyscale image to enhance the image contrast. TEM images have an inherently low S/N ratio, hence, the gaussian smoothening filter was applied for

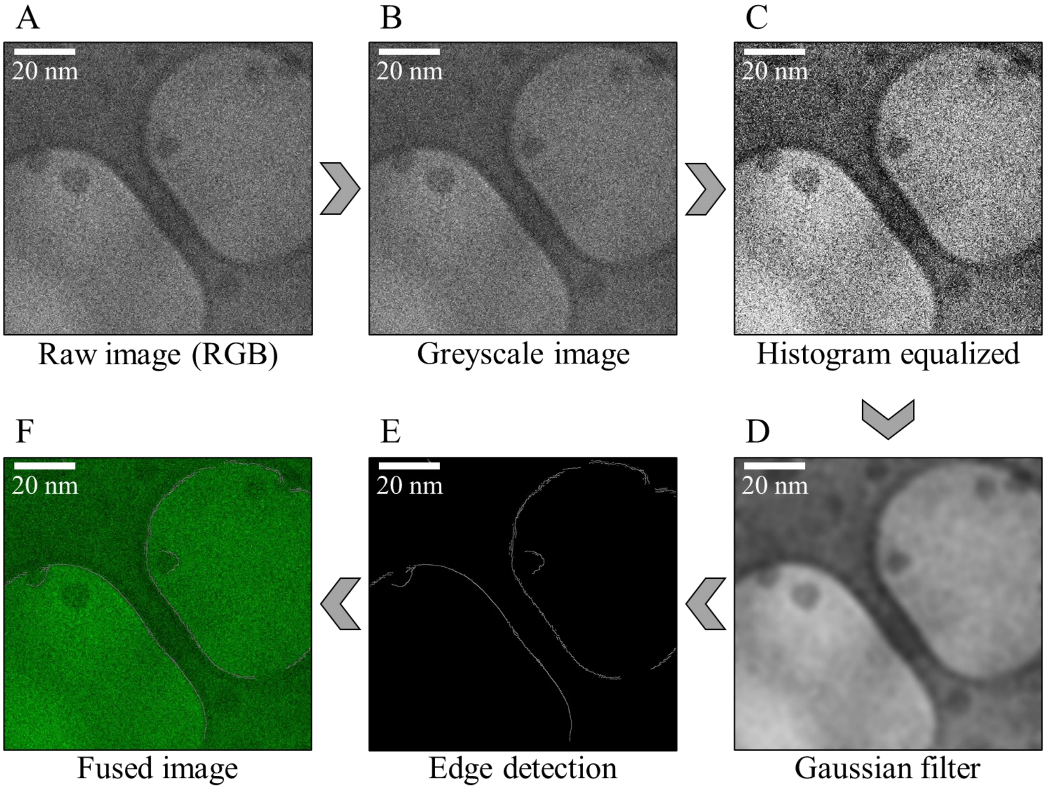

Figure 3.2 Sequential snapshots of the nanobubbles' TEM image showing the results of various operation applied for the edge detection. (A) Raw image captured in RGB. (B) RGB image converted to grey scale image. (C) Image contrast enhancement done using histogram equalisation. (D) Gaussian smoothening filter with standard deviation $\sigma = 12$ for noise reduction. (E) Efficient detection of the interface of the nanobubbles carried using canny edge detection algorithm. (F) The edge detected image fused with the Raw image for further analysis using image analysis package Fiji.[137]

background noise smoothening and improving S/N ratio. The edges (or boundaries) of the nanobubbles were then detected using the Canny Edge detection algorithm. It works by finding the intensity gradients in the image created due to the formation of dark Fresnel fringes in the overfocussed TEM image. **Figure 3.2** shows the sequential snapshots of the resultant images formed by the applied image processing procedures on a sample nanobubble image. The resultant edge detected binary image was then fussed on the original RGB image and the distance measurements were carried using an open-source image processing and scientific image analysis package: Fiji.[137] Qualitative estimation of the height profiles of the TEM images and their 3-D reconstruction based on the image's local intensity was done using Gwyddion.[173] It is also an open-source multi-platform software that can be used for general height field and greyscale image processing.

3.3 Results and Discussions

3.3.1 Nanobubble observation in liquid cell

As discussed in the previous chapter, the interaction between the water and ionizing electron beam leads to the formation of various molecular and radical products, with H_2 and O_2 being the gaseous species (radiolysis).[66] This electron beam governed radiolysis of water produces rapid statistical fluctuations in the local concentration of the product species imparting the required free energy for nucleation.[174] Since the saturation concentration in of H_2 (1.57 mg/l) in water is far less than that of O_2 (41.60 mg/l), H_2 molecules agglomerate quickly to form nanobubbles. The nanobubbles in this study were nucleated using the dull beam so that the population density of nanobubbles facilitates the true characteristics without enforcing much-complicated physics.

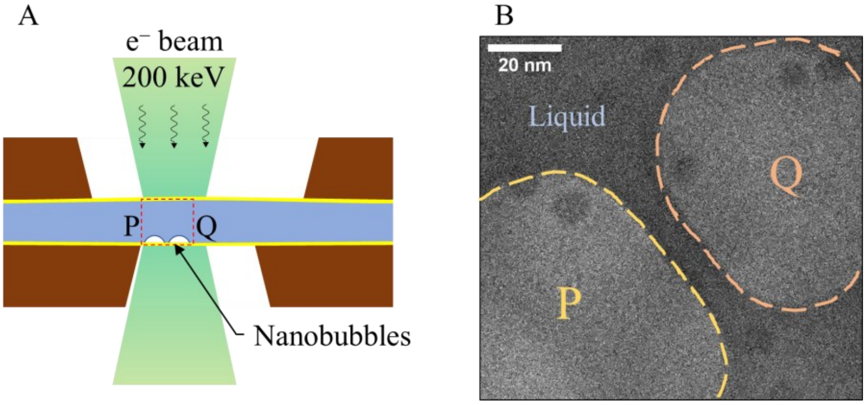

Figure 3.3 (A) Schematic diagram of the liquid cell and the surface nanobubbles during the observation. The red-dashed line represents the region of interest i.e., the region between the adjacent interfaces of the nanobubbles. (B) Image frame from the TEM experiment showing nanobubbles P and Q. Scale bar: 20 nm.

Figure 3.3(A) shows the schematic of the liquid cell as well as the TEM image of the nanobubbles. Two stable surface nanobubbles (P and Q), were observed and tracked during the experiment, as shown in **Figure 3.3**(B). Since the contact area of nanobubbles P and Q was not circular, their radii, approximated using $r \approx \sqrt{\mathrm{Area}/\pi}$, and came out to be 36 nm and 31 nm, respectively. These bubbles exhibited dark Fresnel fringe at their respective interfaces, therefore, it can be estimated that these bubbles are present on the lower SiN_x window (region of under-focus).[34] Moreover, the bubbles' contact angle, from the gas side, was estimated to be less than 90° as no variation in the electron beam intensity was observed in the region outside the 3-phase contact line. The observed nanobubbles were extremely stable in their form and showed a low initial growth rate (quasistatic: 3 nm increase in radius in ~80 seconds). Although, after the initial nucleation, the experiment was carried with a higher electron beam spot size to minimize the beam effects, the nanobubbles were still observed to grow due to higher beam energy at relatively higher magnification (250,000×).

The continuous growth of the nanobubbles and the decreased interfacial distance created an opportunity to observe the merging of two surface nanobubbles with high spatial resolution. In general, the nanobubble dynamic processes are rapid and it is important to reemphasize that the present experiment was carried at a larger spot size, i.e., with low current density, in order to capture the quasi-static nature of the merging process. **Figure 3.4** shows the time-resolved image sequence for the merging of these surface nanobubbles for 220 seconds of observation. The growth of the nanobubbles was observed for the initial 80 seconds of observation time (**Figure 3.4**(A-E)), followed by the initiation of the merging process of the interfaces, as shown in **Figure 3.4**(E,G). The variation in the separation between the adjacent interfaces of two nanobubbles was measured along the four-line segments (A, B, C, D) using the tuned Canny edge detection algorithm, as shown in **Figure 3.5**(A). At the beginning of the observation, the separation between the two bubbles was in the range of $10 - 12$ nm. Due to the radial expansion of the interfaces, the separation gradually decreased up to the value of ~ 6 nm (Figure 3.5(B)) in around 100 seconds. The segments C and D, where the initial separation was the lowest, were the fastest to obtain this separation value (~ 100 seconds), followed by segments B and A (in that order). It is noteworthy that fluctuations were observed for all segments while approaching the minimum separation, as shown in the highlighted sections in **Figure 3.5**(B).

At 100 seconds into the observation, the local image intensity of the region between the two bubbles started to decrease, as depicted by light orange arrows in **Figure 3.4**(F). The variation in the local intensity suggests a slow but definite alteration in mass/thickness of the species in that particular region.[172] This transformation was observed to then propagate to the remaining region between the bubble interfaces, as depicted by the widening gap between blue arrows in **Figure 3.4**(F-J). In principle, the human eye is incapable to detect the difference in images when the contrast variation is less than 10%, therefore, the aid of an image processing tool is essential to visualize and understand the actual occurrence and phenomenon.[172]

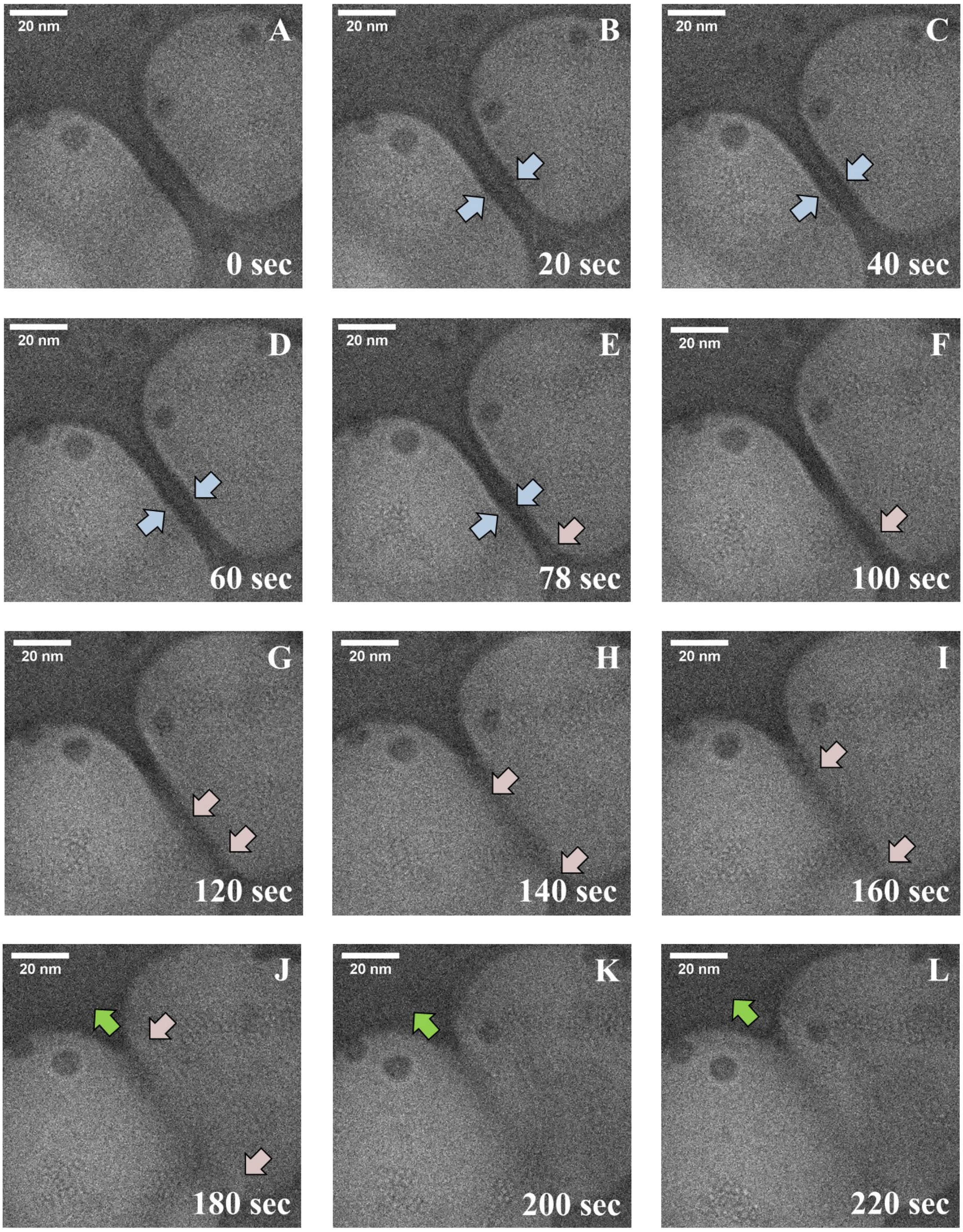

Figure 3.4 Time sequence of merging of nanobubbles observed using TEM for 220 s (A–L). Light Blue arrows show the bubble interface approaching during the initial phase. Light orange arrows show the increase in the local image intensity between the nanobubbles. Green arrow shows the increasing image intensity propagating in the plane parallel to the SiN_x window.

To understand this image intensity variation and the evolution of liquid film between the two bubbles, plots based on the variation in the image intensity along various line segments at the interfacial region were plotted. **Figure 3.6** shows the profile of the interfaces along the line segments A, B, C, and D, similar to line segments shown in **Figure 3.5**(A). The profiles were plotted for the merging initiation and completion phases, i.e., for the time 100-240 seconds. It is important to note these profiles do not provide quantitative information about the height of the bubbles, hence, the Y-axis in **Figure 3.6** qualitatively represents the intensity of the image along the line segment. An increasing general trend in the image intensity was observed for all the four-line segments, suggesting the formation (initiation) and propagation (completion) of the species with lower mass/ thickness between two interfaces.

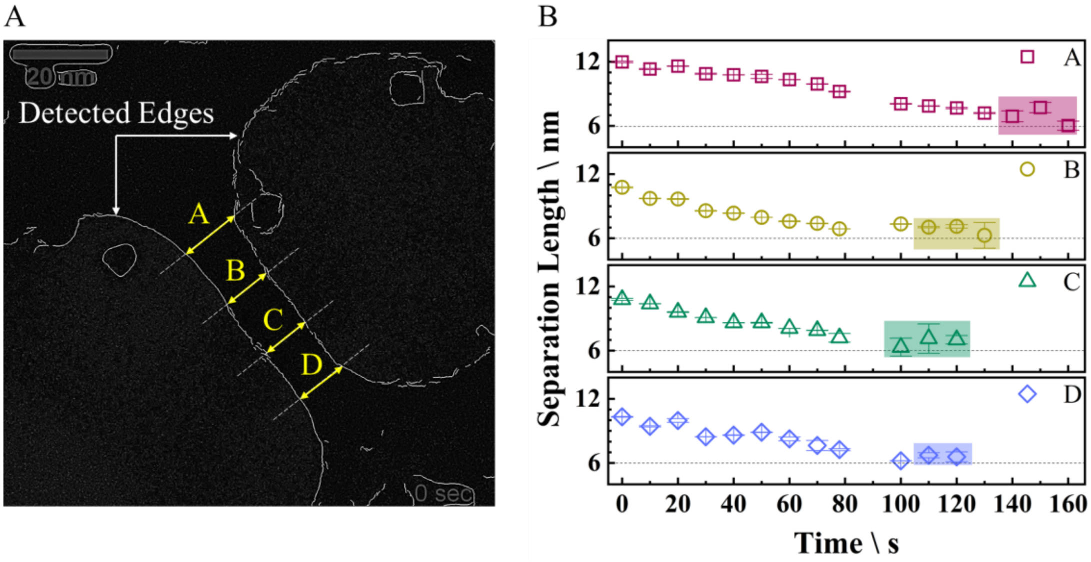

Figure 3.5 (A) Image formed by overlapping the original RGB image with the edge detected binary image, showing the four specific segments: A, B, C, and D, where the distance was measured (B) Variation in the liquid film thickness between the nanobubbles P and Q measured at four distinguish segments. The highlighted region in each graph shows the fluctuations in the interfacial distance observed before merging.

3.3.2 Insights on varying intensity between the bubbles

The absence of supplemental invasive investigatory techniques to physically capture thin film with high-resolution time scales has limited our capacity to filter down our findings, however, the change in the local intensity of the TEM image usually develops due to the change in local density or the thickness of the region in study. One perspective of analyzing the change in local intensity is the variation of density of liquid confined between the interfaces. The

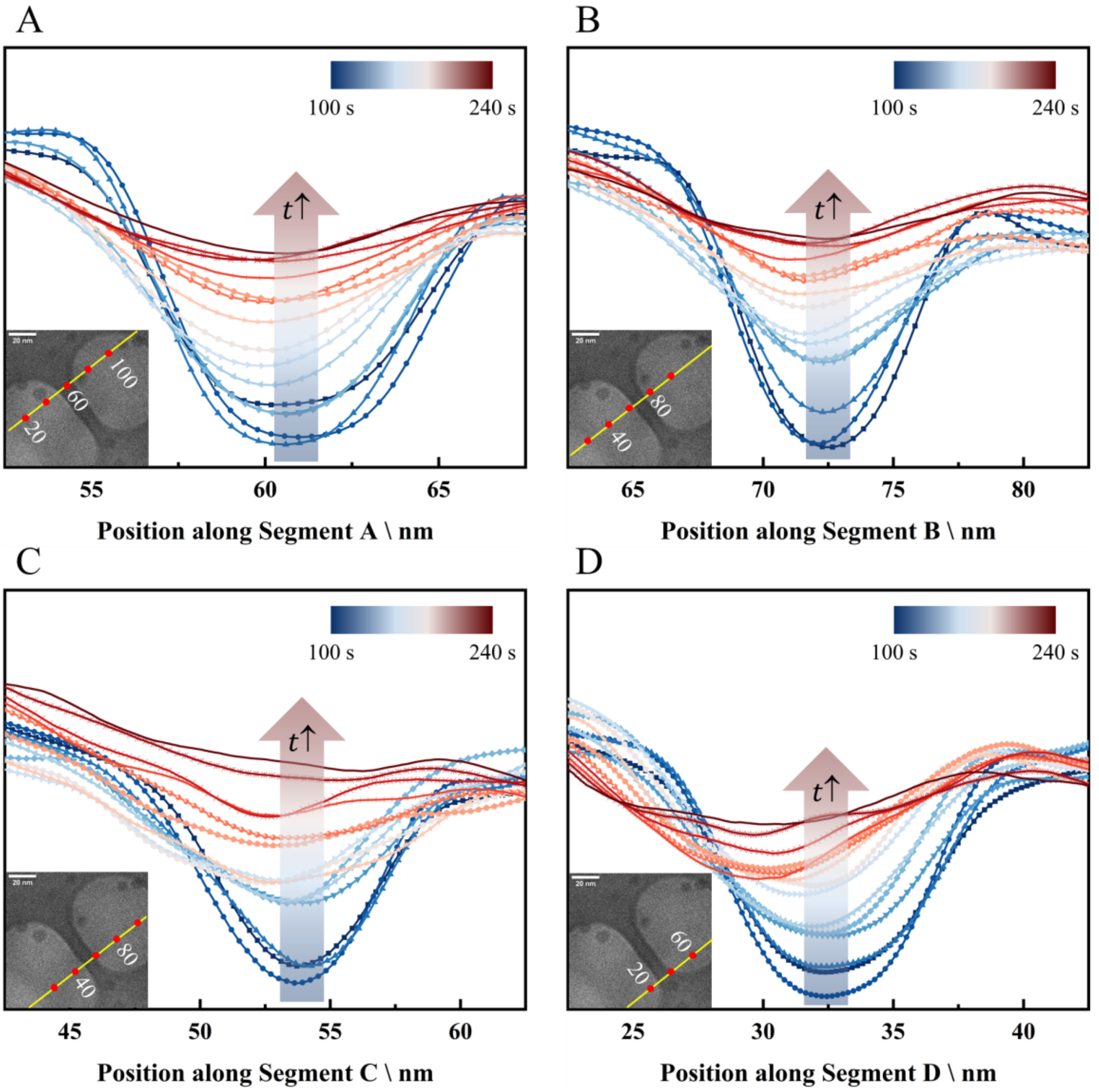

Figure 3.6 Estimated profile of the region between the merging nanobubbles' interfaces based on the variation in the image intensity. The evolution of the intensity is shown for the line segments A, B, C and D (similar to **Figure 3.5**(A)) for the time 100–240 s. Inset in each plot shows the line segment along which the profile was plotted.

presence of two bubbles in close vicinity may further strengthen this argument due to the possibility of enhanced exchanges among them. However, various studies suggest that the inhomogeneity across the liquid surface is usually few Angstroms (molecular level),[175,176] which is one order lower than the separation between two bubbles. The feasibility to capture such variation in liquid density in the localized region with the TEM would be impossible. Additionally, hydration layers are responsible for density variations near the substrate surface,[177,178] but the thickness of hydration layers (order of 10^0 nm) is too little to be practically captured in a >150 nm thick liquid using TEM.

The interaction between the two surface nanobubbles is often weak due to the presence of the three-phase contact line.[150] However, for the slowly growing nanobubble pair (due to continuous e-beam exposure), the nanobubbles are destined to interact as their separation reduces. To understand their interaction, 3D reconstructions of the nanobubbles were done based on the intensity of the liquid and gas phases in the image. **Figure 3.7** shows the reconstructed 3D images for the whole merging process captured. On analyzing the contrast of the region between the two nanobubbles, one aspect of looking into the increase in the local intensity is the formation and increase in thickness of the gas film. At t = 100 s (**Figure 3.7**(F)), this change in intensity is quite noticeable. It can be construed from the reconstructed 3D image, based on changing thickness contrast, that a thin gas layer has formed. The formation of this gas layer initiates at the region having minimum separation (~6 nm), which may be dependent by the acting *vdW* forces and the *EDL* forces as well as the size of the coalescing bubbles. At t = 100 s, the formation of the gas layer begins, as depicted by the light orange arrow in **Figure 3.7**(F), however, no formation is observed at the region of separation greater than 6 nm. The formation of the gas film acts as a precursor for the formation of a bridge between two bubbles. The gas layer then advances in both radial as well as in the perpendicular direction, as seen in **Figure 3.7**(H-L). The formation propagates and starts growth towards bulk liquid which completes the merging process **Figure 3.7**(H).

In addition, we also observed that the initial bubbles themselves and then the merged bubble were not perfectly hemispherical. Similar structures, flat gaseous enriched domains called micro/nano-pancakes, have been previously studied, both experimentally and using MD simulations.[35,102,140,179] A recent MD simulation study on the two equal-sized pinned nanobubbles suggested that the strong gas-solid interactions promote the gas exchanges through tunneling along the solid surface.[150] Hence, the formation of the gas layer may resemble gaseous enrichments on the surface which promotes merging of the nanobubble. Additionally, the presence of ultra-high dense gas phase,[38] specifically, near the solid-gas interface inside a nanobubble,[180] might also promote the formation of a gas layer between two nanobubbles. Moreover, it is known that surface tension decreases with an increase in density and internal pressure, which also enhances the stability of the gas layer between the bubbles.[181]

Additionally, it is evident from the process time scales that the interaction is very weak when the effects of the electron beam are reduced to a minimal. The merged nanobubble also has a neck formed due to the merging. Similarly shaped nanobubbles have been observed previously using AFM,[122] however AFM's lack of in-situ capabilities possibly prevented appreciation of such a phenomenon. A similar proposition has been put forward using MD simulations[182] for unpinned surface nanobubbles, where the authors have discussed on the formation of a layer of gas molecules, on a solid surface with high gas-solid interaction, which serves as a bridge for the exchange between the nanobubbles. Since the surface bubbles observed in our experiments were pinned, the perturbations necessary for the nanobubble interaction were provided by the electron beam.

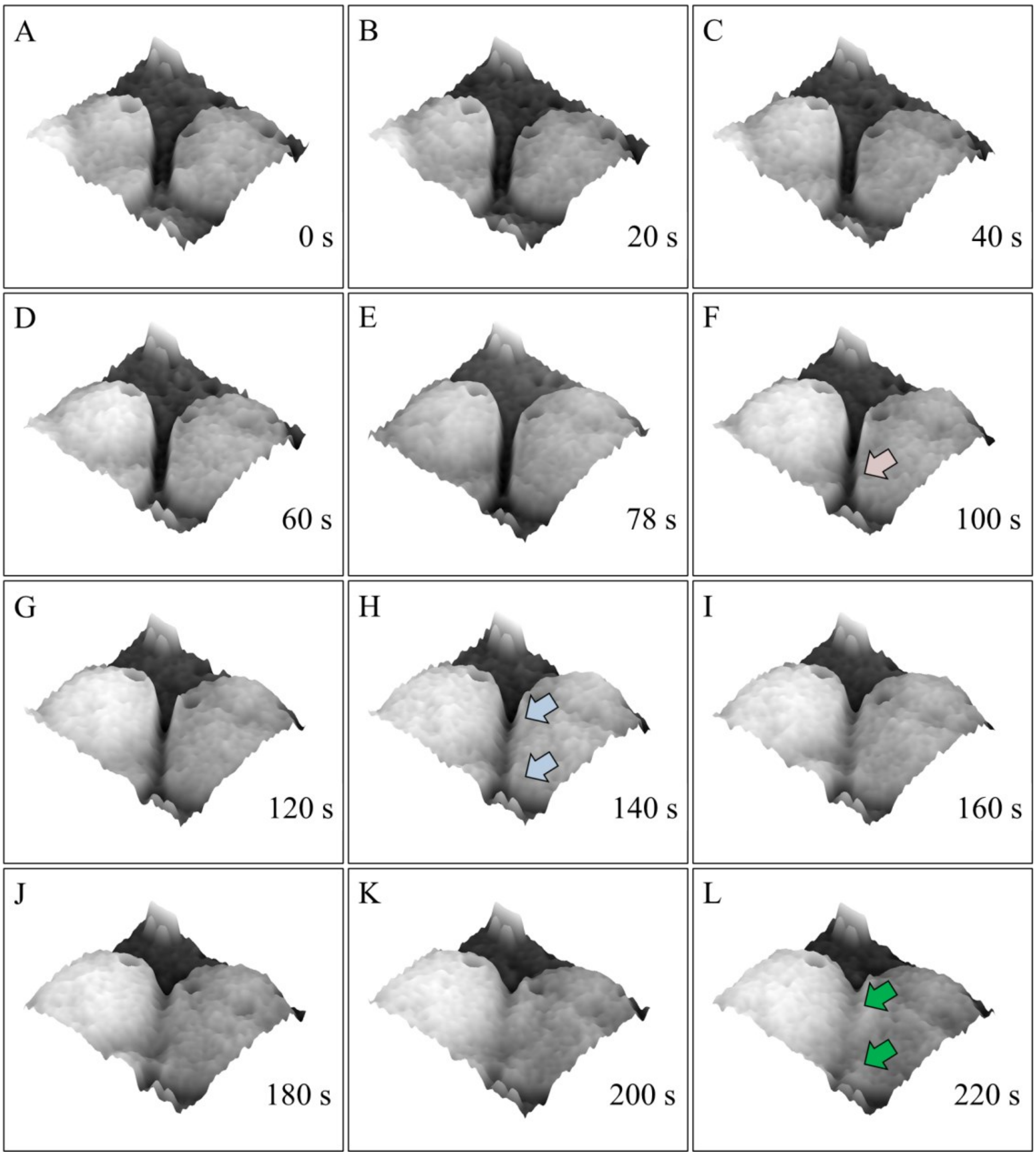

Figure 3.7 3D reconstruction of TEM phase contrast images. Dark region depicts the liquid phase, whereas the bright region depicts the gaseous phase. 3D reconstructions are shown for the TEM images present in presented in Figure 3.4. The light orange arrow in (F) highlights the initiation of gas layer formation, which then translates throughout the interfacial region, as depicted by the light blue arrows in (H). The gas layer then grows and completes the merging process, as depicted by green arrows in (L).

3.3.3 Proposed mechanism for the formation of the thin gas layer

The association of the like molecules is always favored over dispersion due to the presence of effective attraction between alike molecules, albeit, with the proviso that the coulombic forces are nondominant.[133] As the concentration of the molecules exceeds their solubility limit, the association may result in a separate phase, either in the medium or at the interface. Moreover, thermodynamics favors the molecule cluster formation over the bubble formation, provided the nucleus size is less than the critical nucleus size.[183] Here, we propose the formation of the gas layer mechanism using the pathway which involves the formation of gas clusters at the interface (**Figure 3.8**), which act as a precursor for nanobubble merging. Initially, as the bubbles are 10-12 nm apart, the gas molecules produced due to low intensity but continuous electron beam irradiation leads to the initial quasi-static growth of nanobubbles, as shown in **Figure 3.8**(A). The irradiation also creates a higher local saturation of gas molecules through its path. As the nanobubbles' adjacent interfacial distance decreases, and the repulsions between the interfaces inhibits further growth, the number of the gas molecules in the region close to the adjacent three phase contact lines grows, due to diffused nature of interfaces, which increases the effective gas molecular density in this region. The increased local gas concentration leads to the accumulation of molecules and ultimately leads to the deposition of a gas molecule clusters (**Figure 3.8**(B)) and successive formation of thin gas layer near the surface, as shown in **Figure 3.8**(C), which resembles the quasi two-dimensional gaseous domains called micro-nano pancakes. Luo et al. suggested that the interfacial region between the gas and liquid may be considered as the coupled gas-liquid layer,[184] which is the case of nanobubbles is expected to have a lower surface tension due to the higher supersaturation ratio. The effect of the supersaturation ratio on the surface tension is linear and is given by:

$$\gamma(s) = \gamma_0 \frac{s^+ - s}{s^+ - 1}$$

where, s is the supersaturation ratio, $\gamma(s)$ is the surface tension at given supersaturation ratio s, γ_0 is the saturation surface tension ($\gamma_0 = 0.072\ N/m$), and s^+ is the spinodal saturation ration.[185] The decrease in surface tension with increase in the supersaturation ratio is consistent with the experimental results suggesting that the surface tension of water is lower in presence of oxygen or nitrogen and water vapor than in the presence of pure water vapor, as discussed by He and Attard.[186]

The prospect of having lower surface tension at this region is further supported by the fact that the density of gas molecules near the solid surface surrounding the nanobubble is very high,[38] which increases the Tolman's length due to the easing unbalanced force state leading to substantially low surface tension.[187] Moreover, this gas layer exhibits slow growth dynamics because of the intrinsically strong liquid-solid interaction between the water and SiN_x window and the effect of reduced surface tension due to oversaturation. The gas layer then gradually expands and spreads throughout the region in-between nanobubbles, thus completing the merging of the nanobubbles, as shown in **Figure 3.8**(D).

This proposition is further supported by the fact that fluctuations of interfaces were observed when the separation between the nanobubbles approached its

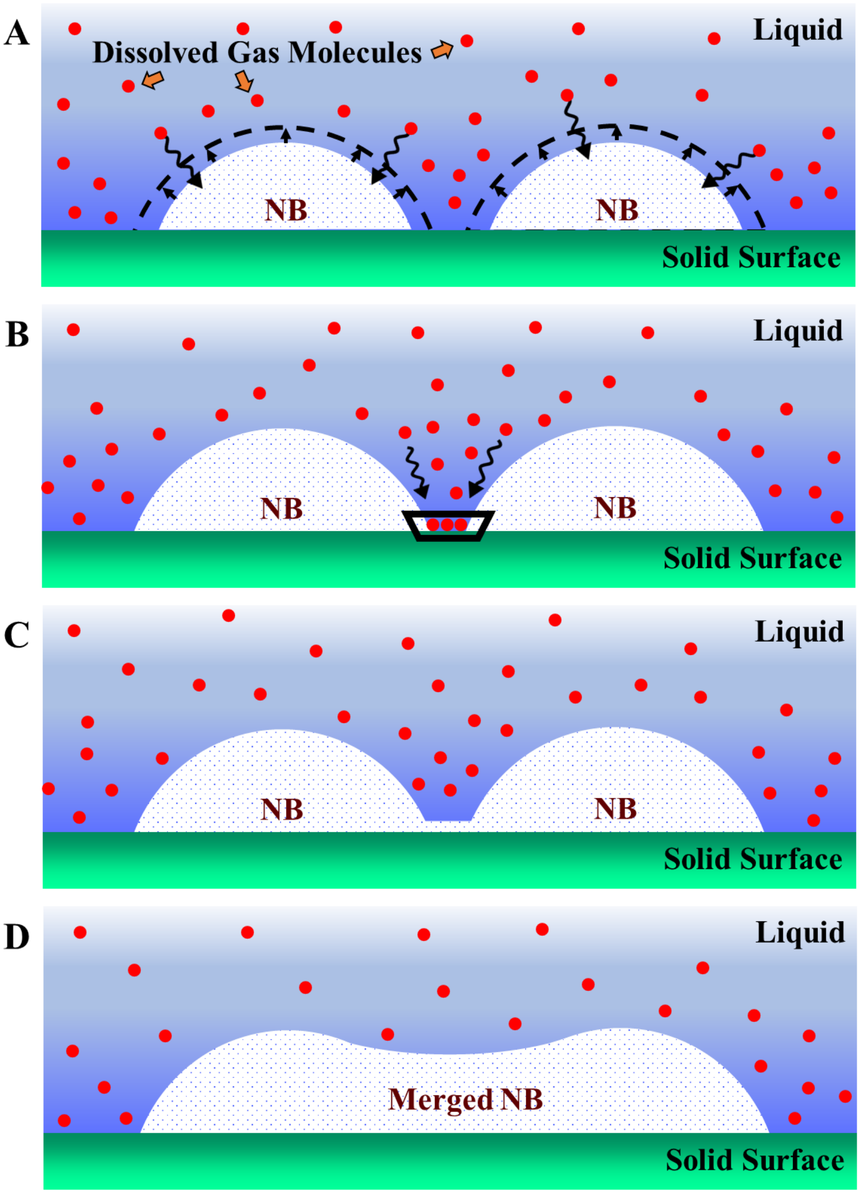

Figure 3.8 Pathway for the formation of a gas layer between two stable surface nanobubbles. (A) Electron beam increases the gas concentration of the irradiated region, leading to quasistatic expansion of the bubbles. (B) Gas molecules begin to accumulate at the solid surface between the two bubbles, forming an adsorbed layer. (C) Gas layer nucleates between the bubbles. (D) The nucleated gas layer grows while acting as a bridge between the two nanobubbles, thus completing the merging process.

minimum, as shown in the shaded regions in **Figure 3.5**(B). These fluctuations are possibly due to the shifting Fresnel fringes when thin gas layer forms and grows in the perpendicular direction. The formation of the thin gas layer on the surface interferes with the interface of bubble imaging in a way that an apparent increase in the separation is observed.

3.3.4 Effect of gas saturation on gas-layer initiated merging

We also carried a qualitative study to investigate the effect of gas oversaturation on the rate of gas-layer formation and its growth rate during the nanobubble coalescence. Gas oversaturation is known to play an important role in defining the stability[68] and dynamics[188] of nanobubbles. Kim et al., in their theoretical study, found a strong correlation between the effect of oversaturation and the growth of nanobubbles and were able to match their model with the experimental findings.[71] Moreover, gas oversaturation in the liquid cell can be affected by the electron dose or intensity, irradiation time, and

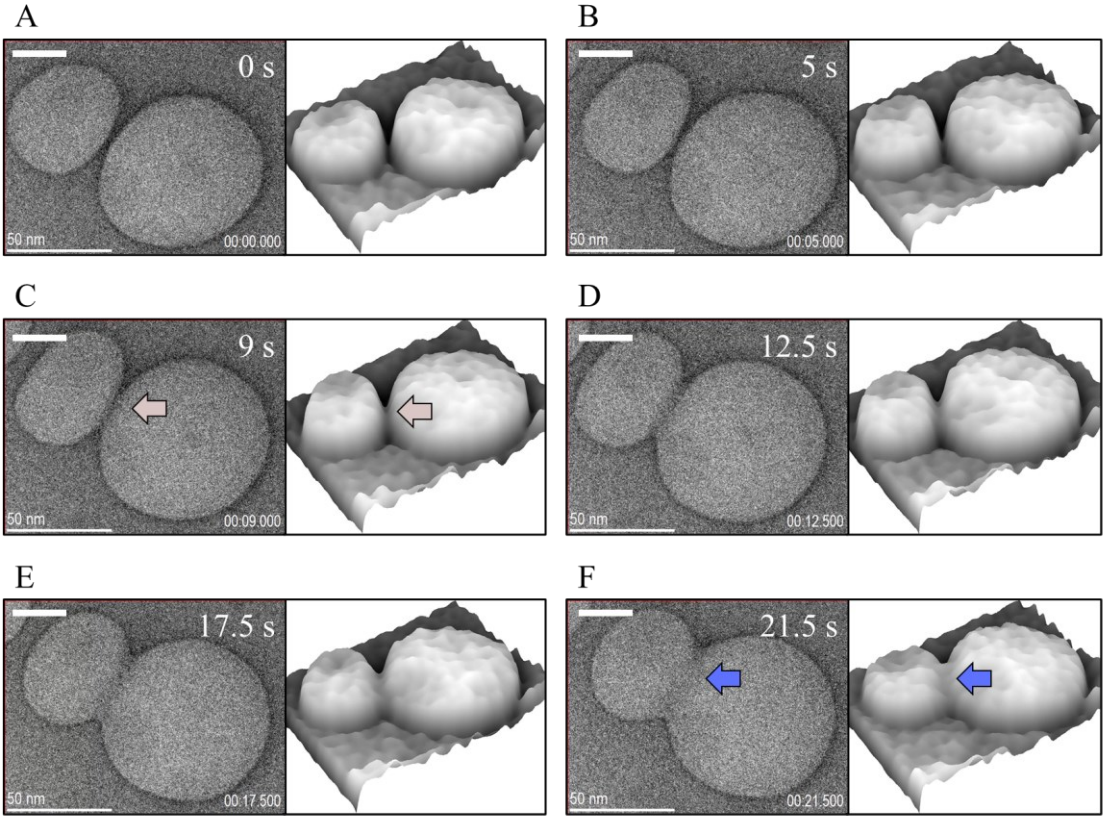

Figure 3.9 Time sequence of merging process observed at higher electron intensity of ~2.8 A/cm^2. The nanobubbles have separate 3 phase contact line as highlighted by yellow arrow in (A). The initiation of the gas layer formation (C) and the successive merging was observed to be much faster when compared to the merging observed at a relatively weaker electron intensity of ~0.3 A/cm^2.

the volume of the liquid cell. Although it is inherently difficult to account for the irradiation time and the volume of the liquid cell, mainly due to the initial threshold irradiation required to nucleate the nanobubbles and the intricate internal geometry of the liquid cell, respectively, the electron intensity can be controlled by changing the spot size and the beam convergence on the fluorescent screen of the TEM.

In the series of other experiments, we observed similar merging dynamics between the nanobubbles. The electron beam intensity calculated at the CMOS sensor varied from 0.07 A/cm^2 to 2.8 A/cm^2. It is important to note that the measured electron beam intensity depends on the liquid cell thickness, which may vary depending on the region of image acquisition, or the vacuum level of the TEM column. **Figure 3.9** shows the merging process of two nanobubbles captured at the electron intensity of 2.8 A/cm^2. The merging process was observed to be ~10× faster, in comparison to the merging phenomenon captured at 0.3 A/cm^2, showcased in **Figure 3.4**. The formation of the gas layer starts at 9 seconds, as highlighted in **Figure 3.9**(C), followed by its growth and completion of merging in 21 seconds. This is due to the enhanced number density of the gas molecules present in the liquid which rapidly begins to deposit on the solid surface and participate in the merging process. Moreover, this strongly reaffirms that the rate of gas film formation, propagation, and its growth is strongly dependent on gas oversaturation. Similar growth dynamics were also observed in the merging of nanobubbles captured at 0.07 A/cm^2 and 0.87 A/cm^2, which are presented as supplementary information (**Figure S8** and **S9**). **Table 3.1** shows the effect of electron beam intensity on the coalescence time. Here, coalescence time is the time-lapse between the initiation of gas film formation and the bubble relaxation phase.

Table 3.1 Effect of electron beam intensity on the nanobubble coalescence time

Sr. No.	Electron beam intensity (A/cm^2)	Coalescence Time (s)
1	0.07±0.01	323±61
2	0.38±0.11	130±20
3	0.87±0.04	21±6
4	2.87±0.18	12±2

3.3.5 Evolution of multiple merging nanobubbles

Due to the lack of control on the existence of nanobubble’s population at any liquid-solid interface, it is highly pragmatic to encounter situations having more than two nanobubbles present at the interface. During the nanobubble observation, we also observed the simultaneous merging of multiple nanobubbles. **Figure 3.10**(A) shows the initial image of five surface nanobubbles undergoing coalescence via gas layer formation at their respective interfacial region. All these nanobubbles have a mean diameter below 50 nm.

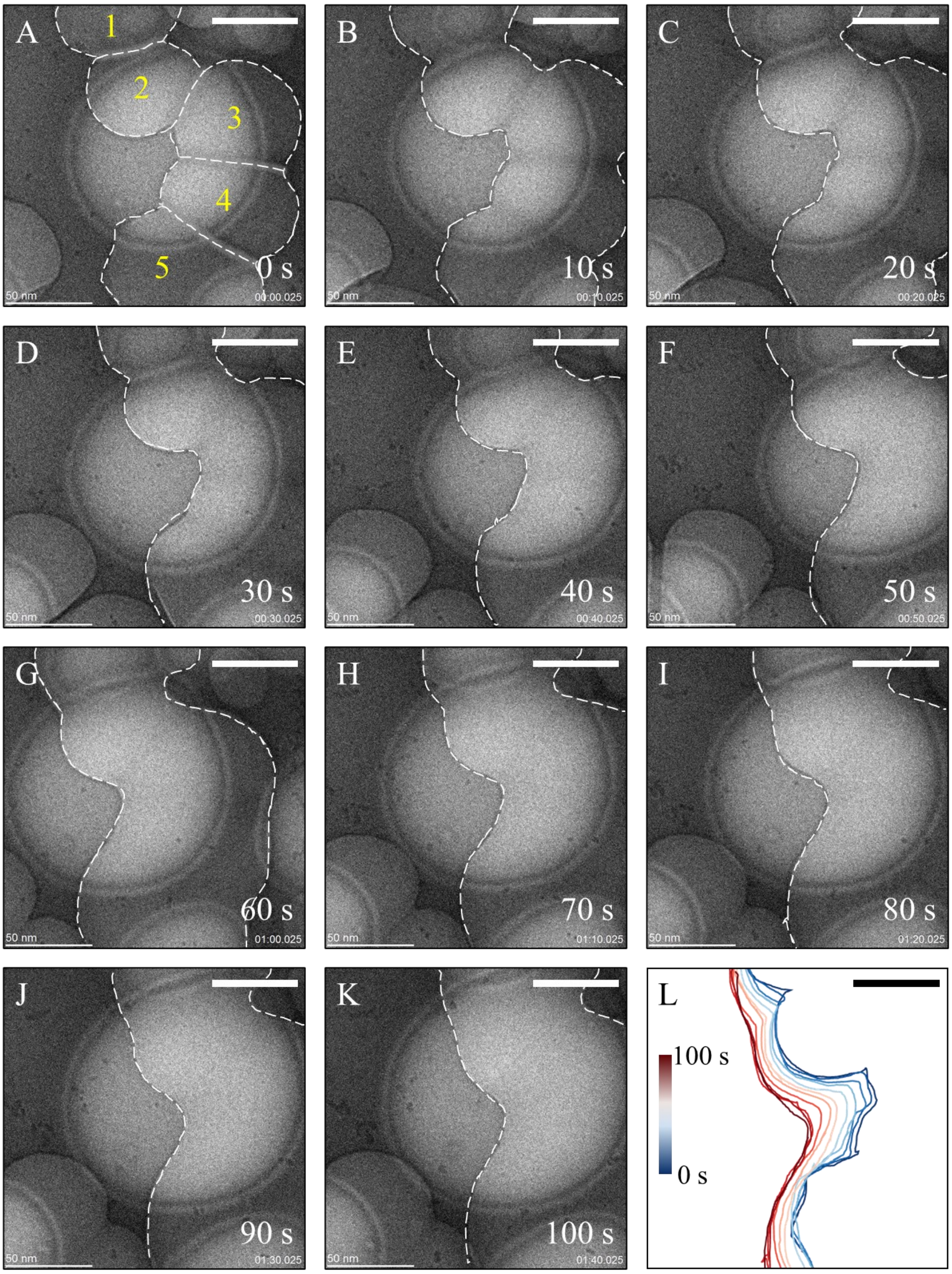

Figure 3.10 Time sequence imaging for the merging phenomenon in 5 adjacent nanobubbles imaged for 100 seconds. (A) The merging initiated by the formation of gas film between the nanobubbles. (B-E) The gas film grows, thus forming the flat nanobubble. (F-K) Slow evolution of the contact line during the interface relaxation of the merged nanobubble. (L) Interface evolution of the nanobubbles. Scale bar: 50 nm.

Few bubbles exhibiting bright Fresnel fringe are also present in the image frame, which are present on the other SiN_x window. In the time frame of 40 s (**Figure 3.10**(B-F)), the gas layer, along with the nanobubbles, seem to have evolved into a skewed nanobubble, having a flattened gas-liquid interface. However, at this instance, the 3-phase contact line have a concave curvature. Further, the merged bubble undergoes interface relaxation to stabilize its geometry, as observed in **Figure 3.10**(E-K).

The contours depicting the movement of the 3-phase contact line is shown in **Figure 3.10**(L). The slow dynamics of the gas layer and the nanobubble's interface can be explained on the basis of dependence of surface tension on the oversaturation degree.[186] **Figure 3.11** shows the schematic for the simultaneous merging of multiple nanobubbles. In the initial state, the bubbles have high internal pressure due to their comparatively smaller radii. As the oversaturation increases, the gas layer formation begins and forms roughly trough-crest shape. As this point, the surface tension is reduced due to the increased oversaturation, which may even vanish at the spinodal.[181] The gas layer then completes the merging of the nanobubbles, thus reducing its internal pressure and stabilizing it.

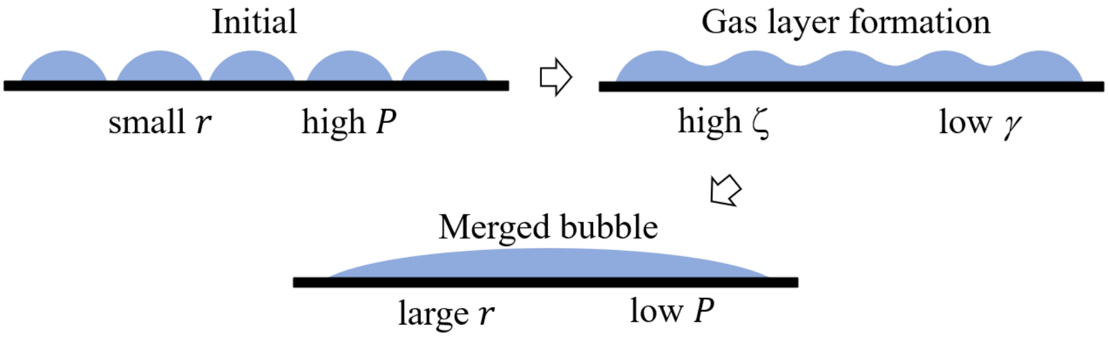

Figure 3.11 Schematic for the simultaneous merging of five nanobubbles. Merging process here resembles the merging in a nanobubble pair. The growth and evolution of gas layer leads to the formation of larger bubble having lower internal pressure.

3.4 Summary

In summary, we studied the coalescence process in surface nanobubbles using in-situ liquid phase electron microscopy. We observed nanobubbles having size below 100 nm nucleated at the solid-liquid interface due to the radiolysis of thin film of water under electron beam irradiation. Due to the continuous irradiation, the nanobubbles grew and coalesced. Further, analysis of the

TEM's contrast images and their intensity profiles helped in understanding the dynamics of formation of gas-layer and the successive nanobubble merging. We found that the formation of the thin film initiated in a localized region-wise manner when the interfacial distance between the adjacent nanobubbles decreased. We also propose a plausible mechanism indicating the formation of high gas molecule dense region between the nanobubbles. The interfacial region between the gas and liquid may be considered as the coupled gas-liquid layer, having lower surface tension which facilitates the formation of gas layer. These highly saturated regions were postulated to initiate the formation of gas layer at the regions where the separation between the nanobubbles was minimum. Our results suggest the formation of the bridge between the stable surface nanobubbles which is important for their merging. Further, we also found that the rate dynamics of the gas layer formation is driven by the oversaturation level in the liquid. The gas layer governed merging was also observed for multiple nanobubbles undergoing simultaneous coalescence. The formation of skewed nanobubbles was also observed which could be crucial in understanding the wetting-dewetting dynamics governed by nanobubbles.

Future studies on this subject can be focused on the slow evolution of gas layer, its precise measurements, and the quantitative evaluation of liquid surface interactions, as well as on the estimation of gas saturation and the successive coalescence of nanobubbles at different saturation levels. Moreover, the present study can be used to develop nanobubble patterns, as discussed in the following **Chapter 4**, which due to their stability can be used in development of facile soft pattern making processes. The present study will also aid in understanding and development of nanoengineered surfaces for targeted submerged applications, e.g. in 2-phase heat transfer, fluid flow in nanocapillaries etc. Nonetheless, the present analysis serves as prima facie affirmation of the nanobubble merging process initiated by gas-layer formation.

4

Writing Nanobubbles

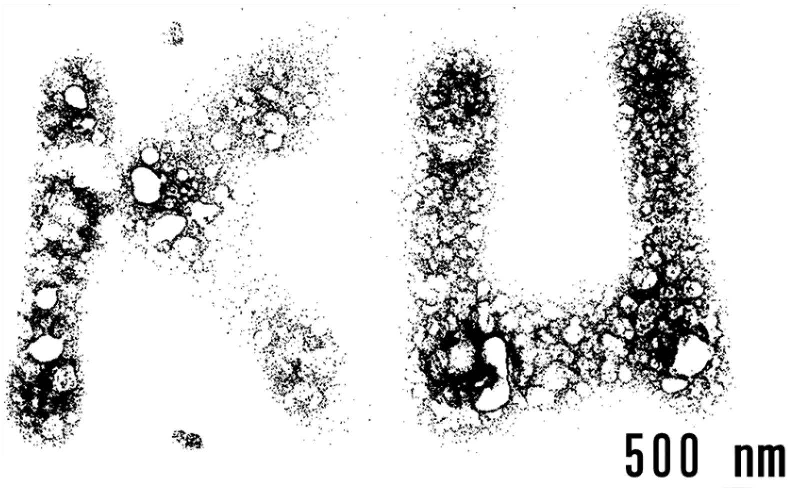

In this chapter, a novel methodology to fabricate soft-matter line features from surface nanobubbles is demonstrated. The highly focused electron beam from the TEM is used to generate localized oversaturation in the liquid film whereas the TEM's trackball is used to facilitate sample-electron beam relative motion, which is required to nucleate and embed surface nanobubbles in a pattern on the SiN_x *membrane. The feature size achieved using this methodology is less than 300 nm, which is an enhancement from the ~1 µm resolution achieved using the laser governed bubble assisted nanofabrication. Our study also demonstrates the stability of the printed nanobubble features for long duration, both temporally as well as in liquid flow, which is advantageous for several practical applications. Apart from providing a methodology to nucleate surface nanobubbles features, the present chapter also proposes several applications where this methodology can be applied in practice.*

4.1 Background

Although the history of writing small is undetermined, the nanotechnologist's *sacred* text: *Why can we not write the entire 24 volumes of the Encyclopedia Britannica on the head of a pin?* by Feynman was one of the initial perspectives focused on writing small features by immobilizing atoms or molecules.[189] The ability to tailor structures on a surface at the nanoscale is important for molecular electronics, materials assembly, and numerous other applications and processes. Exemplifying this, writing features or patterns at the nanoscale is important for miniaturization in nanofabrication[190] and provides an opportunity to control various processes at the nanoscale.[191] The ability to fabricate nanometer-sized features in the modern IC chips by modernizing the photolithography processes has played a vital role in extracting high computational efficiency from electronic devices.[192] Likewise, the feature printing at the nanoscale has also been applied to produce interfaces having tuned physical properties[193] or multi-functionalized chemical properties.[194] It is, therefore, important to explore alternatives for the demand of various nanoscale industries to write and embed nanoscale features, which can also assist secondary processes required to fabricate intricate features.

Various researchers have used bubbles to fabricate features having low dimensions in the past. The capabilities of the laser induced bubble assisted fabrication are demonstrated in the **Figure 4.1**. Particularly, bubble pen lithography technique[195] is a popular technique that uses plasmonic bubbles to agglomerate and print features made of colloid particles (**Figure 4.1**(A)) or quantum dots (**Figure 4.1**(B)).[196] Laser-based techniques have also demonstrated nanoparticle ring fabrication on the gold surface (**Figure 4.1**(C)),[197] and accumulation of microparticles using vapor nanobubbles, as shown in **Figure 4.1**(D).[198] However, all these laser-based techniques lack the capability to print patterns having feature sizes less than 1 µm, possibly due to the size of the opto-thermally generated surface bubble.[199] Therefore, with the advancing miniaturization, the demand exists for a facile bubble patterning technique having feature resolution less than 1 µm which can support complex operations. Surface nanobubbles assisted nanofabrication has the potential to

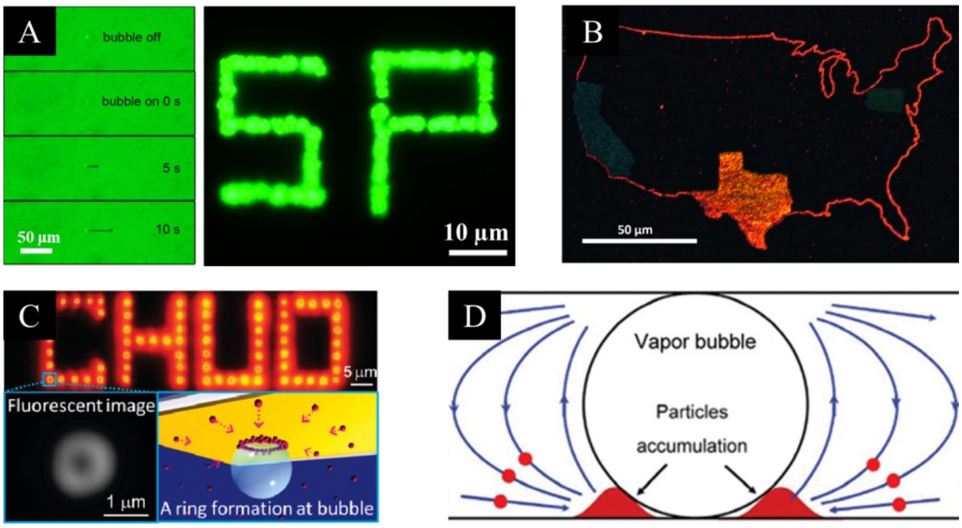

Figure 4.1 Laser induced bubble assisted fabrication. (A) Bubble-pen lithography using plasmonic bubbles to form nanopatterns from colloidal particles. Image adapted from [195] Copyright © American Society of Chemistry. (B) High resolution bubble printing of quantum dots and patterning. Image adapted from [196] Copyright © American Society of Chemistry. (C) Ring structured fabrication of nanoparticles on gold surface using laser-induced micro-nanobubbles and the Marangoni convection and capillary flow around it. Image adapted from [197] Copyright © American Society of Chemistry. (D) Particle accumulation due to the convection flow around the continuous wave laser induced vapor bubble. Image adapted from [198] Copyright Royal Society of Chemistry.

fill in this gap due to their nm size. Moreover, surface nanobubbles are believed to exhibit stability and long life, which may be advantageous for fabricating complex patterns requiring multiple steps. Additionally, the capability to nucleate and create nanobubbles patterns is also advantageous for inhibiting metallic corrosion on exposed surfaces by acting as a bubble mattress between the corroding liquid and the metallic surface and by promoting agglomeration of silica precipitations (or other impurities) on the steel surface.[97]

Therefore, in this work, we have focused on developing a methodology to nucleate surface nanobubbles and form line features at the liquid-solid interfaces using the electron beam. This methodology has its analogy to the dip-pen lithography,[200,201] where the electron beam is analogous to the scanning tip, the nanobubbles are analogous to the material deposited at the tip and the tip radius is analogous to the electron beam spot size. The TEM trackball is used to traverse the electron beam through the liquid film and nanobubbles are nucleated along its path. The highly focused electron beam from the TEM is necessary to write such features due to its capability to produce high localized oversaturation through its path. Although the maximum line feature resolution was limited by the electron beam diameter and the operating magnification of the TEM, feature sizes less than 300 nm are achieved using this methodology. The printed nanobubble features are also stable during liquid flow, which makes them advantageous for fabricating complex features requiring multiple operations.

4.2 Experimental Equipment

The experiments were carried using the liquid cell electron microscopy system, details of which are provided in **section 2.2** of this thesis. The e-chips were assembled in a cross configuration with a spacer height of 150 nm. Before the assembly, the e-chips were cleaned using a glow discharge plasma reactor (PIB-10, Vacuum Devices, Japan) to remove any organic contaminations and grant hydrophilicity to the e-chips. After assembling, the liquid cell was kept in a vacuum pumping station (10^{-3}~10^{-4} Pa) and water was allowed to flow between the e-chips for ~12 hours to ensure its integrity before loading into the TEM column. After loading the sample into the TEM, the flowing water was allowed to complete one cycle in order to eliminate any air cavities in the liquid cell. All the observations were carried at room temperature. The nanobubbles were nucleated in static conditions, i.e., without any flow, however, water was intermittently flowed through the liquid cell, at 150 μl/hr, as per the experimental requirements.

The bubble nucleation and imaging were performed using the same TEM (JEM-2100Plus Electron Microscope, JEOL Ltd., Japan), operated at an accelerating voltage of 200 kV. Since high electron density was *sine qua non* for the experiments discussed in this chapter, therefore, the experiments were performed at spot size 1 and high beam brightness, which translates into small beam spot size. The spot size and brightness are governed by the first and second condenser lens of the TEM, respectively, and affects the saturation of gaseous species produced during radiolysis. In addition, the experiments were restricted to a maximum duration of 90 minutes as a factor of safety to avoid SiN_x window damage and fluid leakage into the TEM column.

4.3 Results and Discussions

4.3.1 Nucleation and pattern formation

As discussed in **Chapter 2**, the electron beam convergence can be tuned to nucleate numerous nanobubbles in high number density per specific nucleating area. Moreover, using the highly converging electron beam also ensures the nucleation of nanobubbles having a lower interfacial separation between them. The ability to control the nucleation region and the number density of the electron can, therefore, be utilized to embed patterns made from nanobubble in user-defined shapes practical for numerous scientific and engineering applications. The prerequisite to forming such soft patterns using nanobubbles is the accumulation of high gas oversaturation at localized region traversing through the required shape, which can be performed by controlling the electron beam path. **Figure 4.2** shows the schematic for the liquid cell and

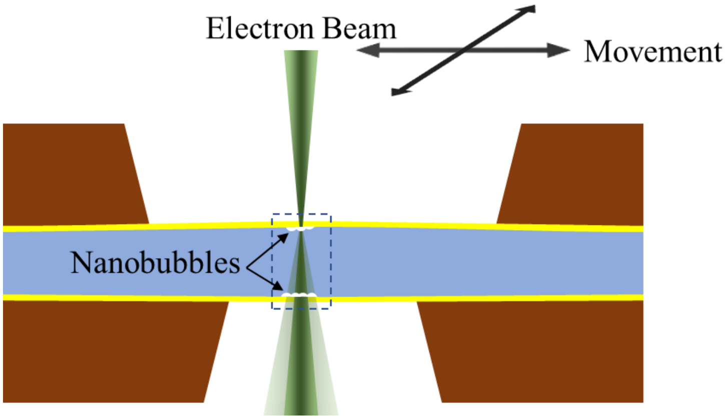

Figure 4.2 Schematic for the liquid cell and beam-stage relative movement to nucleate and pattern nanobubbles.

the relative beam-stage movement which, in our experiment, was controlled manually using the TEM's trackball.

The highly converging electron beam creates excessively high oversaturation in the liquid region, which when scanned through the liquid cells print nanobubbles along its path. The direct imaging of such a process is not possible as it can potentially damage the CMOS camera sensor; therefore, a different approach was utilized to capture nanobubble printing at the liquid-solid interface. For imaging purposes, the patterns were printed using a two-step approach: the excessive oversaturation was created in the region where the pattern was to be printed using a converging beam which would nucleate a few bubbles while the camera shutter was closed, followed by diverging the beam to observe nanobubble nucleation in the adjoining region during pattern formation without damaging the camera. The TEM images for the bubble nucleation are provided in **Figure 4.3**, wherein **Figure 4.3**(A), the opening of the shutter can be seen. The already nucleated nanobubble region (**Figure 4.3**(B)) was then moved to the center of the observation region for electron beam exposure, and the nucleation of new nanobubbles in the adjacence of already nucleated nanobubbles was observed, as shown in **Figure 4.3**(C-F). Although the electron beam irradiation area could not be measured, it is expected to be smaller than the size of the nanobubble cluster (∅ 260 nm) shown in **Figure 4.3**(B). Due to the diffusion of gas molecules, the region adjacent to the electron beam irradiated region is also expected to undergo increase in gas saturation, and hence can provide environment for nanobubble nucleation and growth. It is also worth noting that relatively long exposure at a specific region also leads to several nanobubble dynamics, such as nanobubble growth, merging, and formation of bigger nanobubbles, as shown in **Figure 4.3**(E-F).

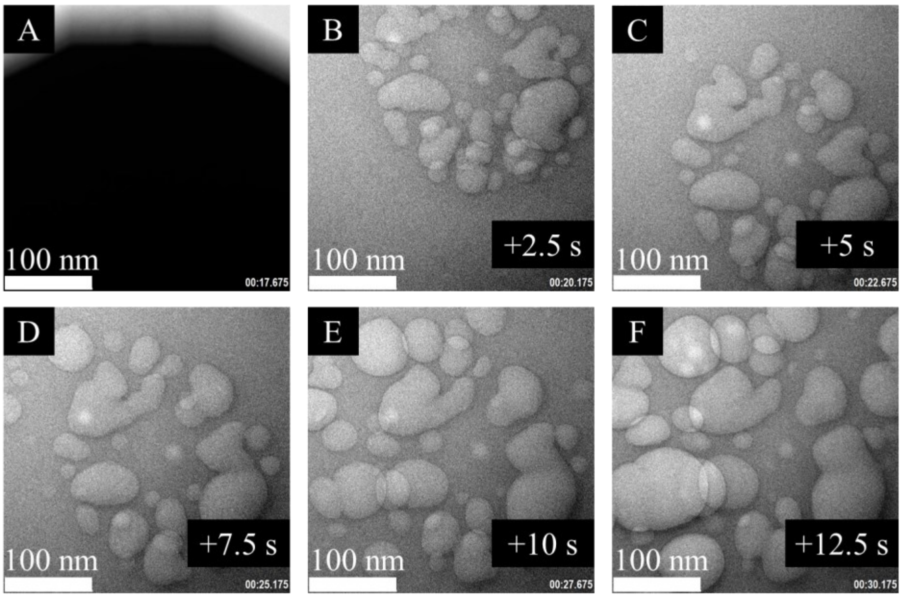

Figure 4.3 TEM imagery showcasing the nucleation of nanobubbles during formation of patterns. (A) Opening of the TEM camera shutter. (B) Bubbles already nucleated by converging electron beam, prior to insertion of camera. (C) Evolution of bubbles began due to prolonged exposure. (D, E, F) Multiple nascent bubble nucleation.

4.3.2 Patterning capability

The nanobubbles formed due to the electron beam-induced radiolysis of water can be nucleated in well-defined shapes and patterns by irradiating the liquid film with the electron beam and controlling the beam path using the trackball of the TEM. **Figure 4.4**(A) shows the schematic of the deployed methodology to print nanobubbles onto a surface using an electron beam. To demonstrate the capability of this methodology, the initials of the Kyushu University [KU] (**Figure 4.4**(B)) are patterned using nanobubbles on the SiN_x membrane water interface. The initials are written by moving the focused beam slowly through the liquid film while keeping high magnification, usually >100000X, and a converging electron beam. As the beam spot traverse through the liquid, very high oversaturation is achieved in a localized area which leads to the formation of nanobubbles and thus, the printing of the pattern. The printed pattern KU, using nanobubbles is shown in **Figure 4.4**(C). The width of the stroke (line feature width) printed depends on the beam spot diameter, usually, little larger than the beam spot diameter. For the printed pattern, the demonstrated line thickness was ~ 300 nm, whereas the initials of KU were confined to 1.5 μm × 2.9 μm area. It is important to note that ~ 300 nm is not the limit as it depends on the TEM and its electron gun capabilities and can further be improved using

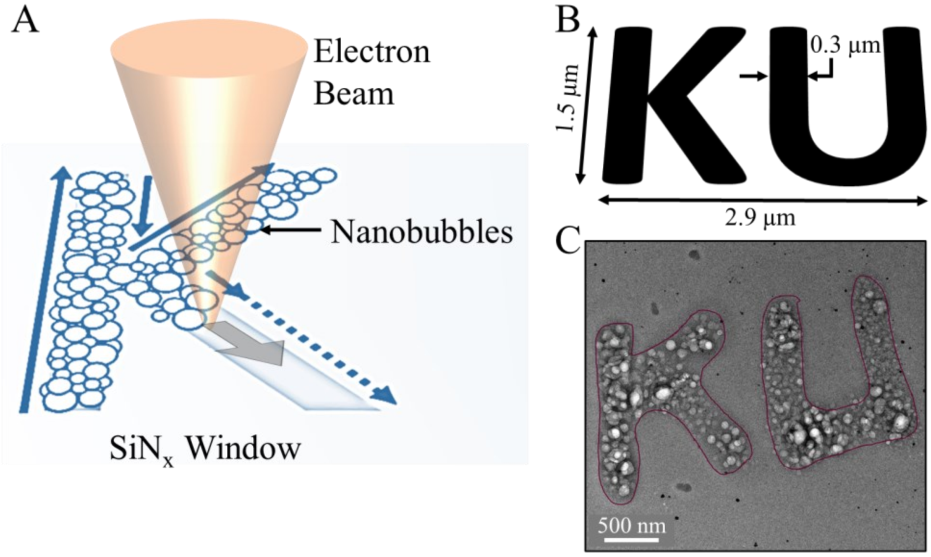

Figure 4.4 (A) Schematic for the methodology to print nanobubbles on a surface using electron beam. (B) Dimensions of the initials of Kyushu University: KU written on the surface. (C) TEM image of the KU written from nanobubbles by controlling the sample using the TEM's trackball.

highly convergent beams having lower spot size. However, to further demonstrate the capability to write the characters, we also attempted writing a few other English letters characters, which are presented as supplemental information (**Figure S10**).

4.3.3 Stability of nanobubble patterns

Stability, or rather longevity, is an important prerequisite for bubbles in order to form patterns or features and to apply them for some useful application. If the patterns printed from nanobubbles are to be used as templates to print certain lithographic features, then these printed nanobubble patterns should also exhibit stability in presence of flow. We demonstrated the longevity of these patterns for as long as the experiment was carried, which in our case was nearly 1 hour. **Figure 4.5**(A) shows the initial captured image of the printed pattern in the shape of the small English language alphabet "*n*". The same region was imaged intermittently for around 1 hour, and a pattern feature was observed in all the images, as shown in **Figure 4.5**(B-E). We also imaged the stability of another pattern, the image of which is provided in the supplementary information (**Figure S11**). While imaging, special care was taken about the beam parameters so that any electron beam initiated nanobubble dynamics, such as growth or accelerated merging processes are not observed. After printing the patterns, the region of interest was only irradiated

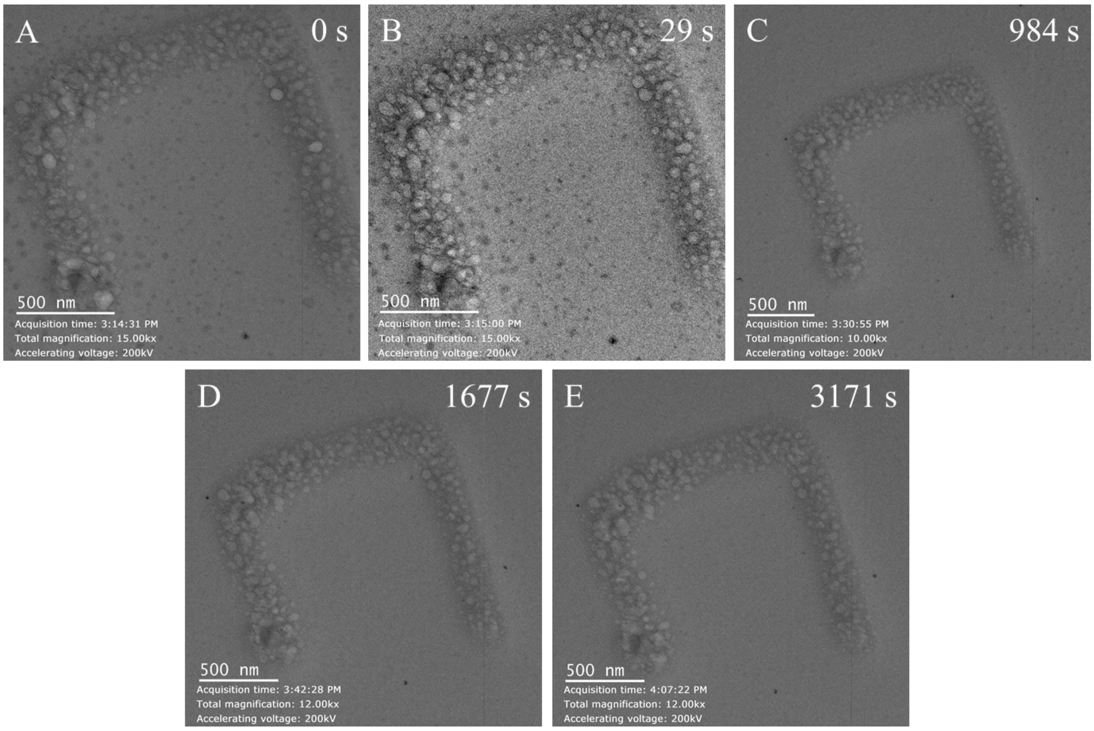

Figure 4.5 Stability of pattern in time due to nanobubble longevity. TEM images of small "n" nanobubble pattern at (A) Initial; (B) 29 s; (C) 984 s; (D) 1677 s; and (E) 3171 s. The information about the time of acquisition and magnification is embedded in the image frames.

with the electron beams while imaging to avoid electron beam induced changes. Although the presence of surface nanobubbles on a solid-liquid interface is of importance to numerous processes, its stability and longevity for several hours can only increase the scope of application.

Additionally, we also tested the stability and longevity of these surface nanobubbles against the flow. For this experiment, we printed clusters of nanobubbles on the surface and initiated the flow between the SiN_x membranes. The flow rate was set at 150 µl/hr, which is limited by the safe operational standard of the liquid cell holder inside the TEM column. On simple analysis using the flow rate of 150 µl/hr, and a cross sectional flow channel 2 mm × (~150 nm – 2 µm), the flow velocity comes out to be in order of 10^7~10^8 nm/s, which is beyond the acquisition capability of the used CMOS camera sensor. We observed the nanobubbles to be stable and immobile during the flow. **Figure 4.6** shows the time sequence image of the nanobubbles in the presence of flow. Although the flow mostly indistinguishable while imaging, we can observe blurring of the contamination region intermittently during flow, as highlighted with the orange arrow in **Figure 4.6**(B, D, F). During the flow, we also observed fluttering in the frame with occasional image blackout, possibly due to vibrations and momentarily increase in the thickness of the liquid film, as shown in the supplementary information (**Figure S12**). This points out that

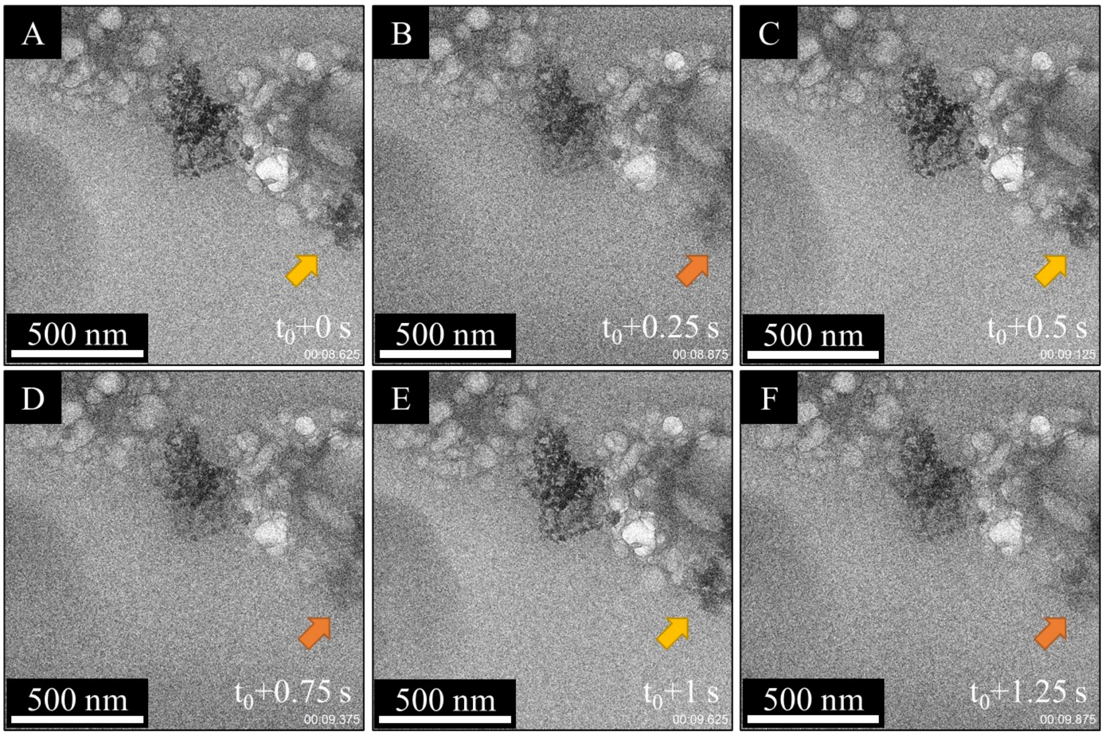

Figure 4.6 Stability of nanobubbles in flow. The variation in the intensity of region pointed by the arrow is an indicator for flow.

the accumulated oversaturation near the nanobubbles is highly localized, usually happens close to the solid surface, and is tolerant towards the liquid flow in its vicinity. Various studies in the past have also pointed towards such slow dissolution rates[29] and higher gas accumulation[38] near the surface. The cooperative effect of nanobubble clusters and the pinning of nanobubbles lead to the slow dissolution rate for nanobubbles, which accounts for the stability of these nanobubble patterns, even when the water is flowed.

4.3.4 Proposed applications

Since the liquid-gas interfaces are vulnerable to surfactant accumulation,[133] the patterns formed using the developed methodology can act as a template for surface fabrications and modifications. In general, the liquid-gas interface attracts nanoparticles, or contaminations, also visible in **Figure 4.6**, which assembles around the nanobubbles forming chains or depositions. Once the liquid is drained or fried, the patterns formed due to depositions can impart desired functional properties depending on the characteristic of the nanoparticles. The same has been demonstrated in **Figure 4.7**(A). Another application of such nanobubbles can be ion segregation or creating nano-spaces with ionic gradients. Liquid-gas interfaces are usually charged which leads to the accumulation of ions at the liquid-solid interfaces. A double layer is formed encompassing the bubbles which create regions having higher ionic densities, as shown in **Figure 4.7**(B).[128] Since the nanobubbles are stable in a variety of salts or ionic liquids,[202] these may then be applied to tune or customize chemical reactions at nano-spaces or reduce the net ionic concentration from a flowing liquid.

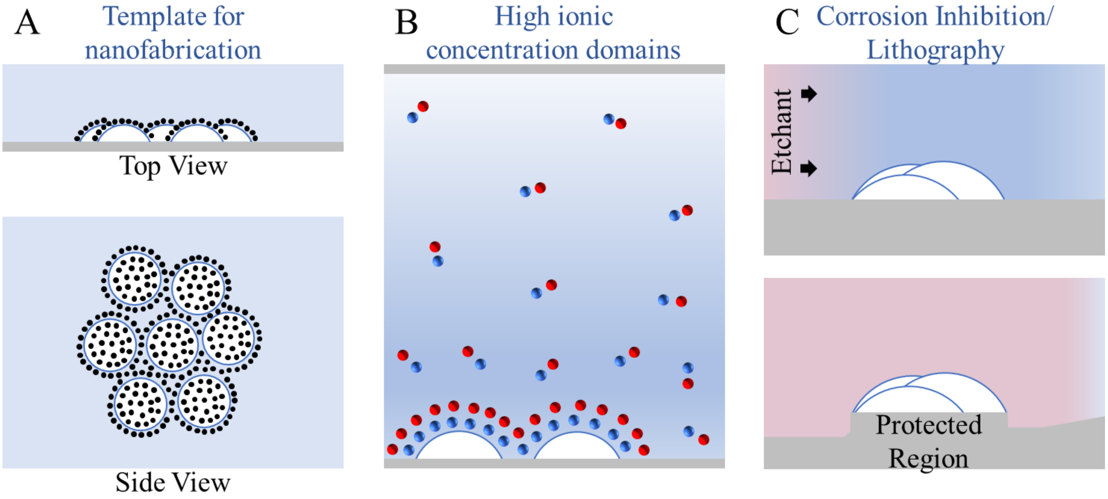

Figure 4.7 Proposed applications for nanobubble patterns. (A) Template for nanofabrication by agglomerating nanoparticles at liquid-gas interfaces. (B) High ionic concentration domains formed due to agglomeration of ions around a nanobubble in an ionic liquid. (C) Corrosion inhibition and 3-D patterns formation due to the protection offered by nanobubbles due to their longevity and stability at numerous conditions.

Another application of such patterns made of nanobubbles is corrosion inhibition. As our study demonstrates the stability of nanobubble patterns, both temporally and in flow conditions, the nanobubbles sitting on the SiN_x surface acts as a mask. In case the liquid is exchanged by a surface etchant, the area masked by the nanobubbles will be protected against material removal or etching and the 3-D nanopatterns having ridges at regions having nanobubbles and valleys at unprotected regions can be formed, as demonstrated in **Figure 4.7**(C).

4.4 Summary

In summary, we demonstrated a methodology to form patterns and features composed of clustered surface nanobubbles on a SiN_x surface using the focused electron beam from the TEM. The localized oversaturation due to high-intensity electron beam traversing on the sample nucleates the nanobubbles through the electron beam's path. We found that the patterns formed using the nanobubbles are temporally stable which makes them quite favorable for application as template material for nanofabrication, or to inhibit corrosion of the surface. Moreover, our study also proves their stability in the presence of flows which demonstrates their applicability for applications where multi-step fabrication is required. We anticipate that the results obtained from our study will provide the benchmark for bubble-assisted patterning technologies with feature size less than the existing ~ 1 µm laser-bubble assisted fabrications.

5

Conclusions and Outlook

5.1 Conclusions

This thesis was centered around delineating the dynamics of surface nanobubbles using the in-situ liquid-phase electron microscopy technique. As the fabrication and instrumentation techniques have evolved in the past, a consensus has formed on the existence of surface nanobubbles. However, most of the established theories have been based on the results obtained using the microscopy techniques lacking either satisfactory spatial resolution or adequate temporal resolution. Therefore, through this study, we aimed to provide mechanistic insights into the dynamic phenomena occurring at the nanoscale by the direct visualization technique.

Although the liquid-phase electron microscopy technique has been used in the past by a handful of researchers to study nanobubbles, our study demonstrated how the electron beam intensity has a role in nucleating nanobubbles having different sizes and number density. After developing a strategy to nucleate nanobubbles, the interplay between a nanobubble pair was studied by nucleating nanobubbles distributed sparsely. It was concluded that the nanobubble's existence and stability cannot be solely attributed to the contact line pinning due to their complex physio-chemical nature. The accumulated oversaturation near the surface was the most important factor governing the nucleation and stability of nanobubbles. Additionally, this work also captured the novel anisotropic depinning of the pinned nanobubbles and revealed the role of localized gas oversaturation in this asymmetric interfacial phenomenon. Further, this study highlighted the effect of the ionic concentration on the coupling of the nanobubbles' interfaces and the pull-push behavior, which is attributed to the EDL encompassing the nanobubbles and their successive interactions.

Our study also focused on providing mechanistic insights into the coalescence process in surface nanobubbles using in-situ liquid-phase electron microscopy. The analysis of the TEM's contrast images captured during the coalescence process revealed that the thin gas film grows in a localized region-wise manner between the neighboring nanobubbles. A plausible mechanism was proposed indicating the formation of high gas molecule dense region between the nanobubbles. The interfacial region between the nanobubbles might be considered as the coupled gas-liquid layer, having lower surface tension which facilitates the formation of the gas layer. These highly saturated regions were postulated to initiate the formation of the gas layer at the regions where the separation between the nanobubbles was minimum. The results also suggested the formation of the bridge between the stable surface nanobubbles which is important for their merging. Furthermore, it was concluded that the rate dynamics of the gas layer formation are driven by the oversaturation magnitude in the liquid.

Lastly, as a demonstration to put surface nanobubbles into the application, a methodology to form patterns and features composed of clustered surface nanobubbles on a SiN_x surface using a focused electron beam from the TEM was illustrated. The localized oversaturation due to high-intensity electron beam traversing on the SiN_x membrane nucleated the nanobubbles through the electron beam's path. The nanobubble patterns formed were stable, which makes them favorable for their application as a template for nanofabrication. The stability of nanobubbles in the presence of flows also pointed that the oversaturation is persistent near the solid surface and is not affected by liquid flow.

The curiosity-driven nature of this research helped to unravel the dynamic behavior of nanobubbles and their interactions. The findings of this research will not only impact the so-far-developed perception of nanobubbles but will also be useful in the development and surface modification of nanoscale devices, nanoscale pipes, chemical reactions, bubble assisted fabrication, and many more.

5.2 Future Research Directions

5.2.1 Immediate research direction

One domain where immediate efforts are required is quantifying the oversaturation produced in the liquid cell while irradiation of electron beam. Since oversaturation is a function of electron beam intensity as well as the volume of the liquid cell, its estimation would require advanced instrumentation for the precise measurement of electron beam intensity interacting with the sample. Quantifying the oversaturation will help in the estimation of the threshold value required to nucleate nanobubbles and will provide deeper insights on the effect of oversaturation on the size distribution or the number density of nucleated nanobubbles. Its quantitative estimation is also essential to develop a deeper understanding of the gas film formation and growth while the nanobubbles are coalescing. Moreover, it was observed that nanobubble clusters are indifferent to flows, which suggests that the oversaturation has minimal effect on the bubbles after nucleation. Contrastingly, it was also observed that the shrinking nanobubble de-pins the pinned nanobubble due to localized changes in the oversaturation. Hence, there needs to be an effort towards understanding the localization of oversaturation and how it can stay close to the solid-liquid interfaces without diffusing into the flowing liquid.

The ionic concentration in the liquid also seems to affect the dynamic phenomena in the nanobubbles, especially the observed pull-push phenomena. The whole concept of a double layer encompassing the nanobubbles also required experimental validation which may be done by nucleating the nanobubbles in an ionic liquid. While we attempted such experiments in order to understand the ion distribution around a nanobubble, we could not optimize the nucleation environment and our efforts lead to either highly dynamic situations or salt crystal formations at the solid-liquid interfaces (supplementary information **Figure S13**), thus impeding the experiments' objectives. The application of graphene liquid cells for performing such experiments on ionic liquid may be fruitful in understanding the formation of a double layer around a nanobubble.

The patterns formed by embedding stable surface nanobubbles on the SiN_x membrane seem to have potential applications in numerous domains as discussed in **Chapter 4**. However, efforts are required to develop a proof of concept of such patterns by putting them into applications.

5.2.2 Additional recommendations

The liquid phase electron microscopy holds potential towards attaining a deeper understanding of the nanobubbles and the gas-liquid-solid interactions in general. Experiments need to be conducted for bubble nucleation in nanofluids (nanoparticle-infused liquids) due to their extensive and established applications. This kind of experiment would impact our understanding of the interaction between the solid-liquid-gas phases at scales where the electrical and surface forces are highly dominant. Tracking the movement of nanoparticles around the nanobubble would help define the influx and outflux from nanobubbles. Of course, the analysis would demand the development of intensive image processing algorithms for realizing the results, the effect of surface wettability and the gas flow near the contact line can be addressed by such experiments. (2) The bubble nucleation on the functionalized nanoparticles (functionalized to enhance nucleation) is another important result from such experiments. The experiments can be performed by using nanoparticles with different sizes (curvature), and the results would help identify the critical nucleation radii for a known gas oversaturation present in the liquid.

List of Figures

Figure 1.1 Nanofluidics. (A) Various length scales at play in nanofluidics. Image adapted from [3] Copyright © Royal Society of Chemistry. (B) Illustration of the design concept of the rotating CNT membrane filter and its desalination mechanism. Image adapted from [6] Copyright © Nature. (C) Top view of a nanogap detector without top sealing plate along with the schematic for DNA detector. Image adapted from [7] Copyright © American Chemical Society. (D) Nanobubble-plugged nanopipette, nanobubble-free nanopipette, and air-filled nanopipette. Image adapted from [8] Copyright © Science. (E) Fabrication of 2nd generation graphene liquid cell (GLC) for nanoscale experiments. Image adapted from [9] Copyright © Cambridge university press...3

Figure 1.2 (A) Behaviour of the 100 nm air bubble in water at various oversaturation (ζ) conditions, using Epstein-Plesset formulation.[11] (B) Bubbles formed in sea water stable for 22 hours. Image adapted from [13] Copyright © Science. (C) Surface gas nanobubbles. Image scale: 2 μm × 2 μm × 40 nm. Image adapted from [18] Copyright © American Physical Society. (D) Bulk nanobubble imaged using TEM freeze fracture replica method. Scale bar 100 nm. Image adapted from [17] Copyright © MDPI. (E) Illustration for the generation a transient vapor plasmonic nanobubble. Image adapted from [16] Copyright © American Physical Society. (F) Vapor nanobubble nucleated in a nanopore using Joule's heating.............5

Figure 1.3 (A) Timeline of the major events in the surface nanobubbles' research. (B) The first speculation of surface nanobubbles in 1994 due to step-like features in the force-separation curve measured between two hydrophobic surfaces. Image adapted from [20] Copyright © American Chemical Society. (C) One of the first image of surface nanobubbles acquired using AFM. Image adapted from [22,39] Copyright © American Chemical Society. (D) Dynamic equilibrium theories: one of the earlier theories used to define the stability of nanobubbles. Image adapted from [26] Copyright © American Physical Society. (E) Image of a collapsing nanobubbles using in-situ liquid phase electron microscopy. Image adapted from [31] Copyright © IOP Science. (F) TIRF-Optical microscope applied to observe surface nanobubbles of radius 135 nm and above. Image adapted from [33] Copyright © American Physical Society. (G) Synchrotron based STXM systems used to understand the density of surface nanobubbles. Image adapted from [38] Copyright © American Chemical Society........................8

Figure 1.4 Characterising nanobubbles using AFM. (A) Schematic for the imaging of nanobubbles using AFM. Image adapted from [41]. (B) AFM image of the surface nanobubbles captured on HOPG substrate. Image scale 2 µm × 2 µm × 40 nm. Image adapted from [18] Copyright © American Chemical Society. (C) AFM-tip nanobubble interaction leading to ambiguous characterisation at different operating modes of AFM. Images adapted from [44] Copyright © Royal Society of Chemistry. 10

Figure 1.5 Optical microscopy of nanobubbles. (A) Simultaneous microscopy (AFM+OM) of nanobubbles nucleated by solvent exchange within a removable channel, along with the OM image and AFM image of the same feature. Images adapted from [46] Copyright © American Physical Society. (B) Setup for the laser scanning confocal microscopy and the nanobubbles observed at the hydrophilic and hydrophobic surfaces nucleated using ethanol-water exchange method. Images adapted from [45] Copyright © American Chemical Society...11

Figure 1.6 STXM imaging of surface nanobubbles. (A) Schematic of the configuration of zone-plate-based STXM, and the SF6 nanobubbles imaged using it. Image adapted from [47] Copyright © International Union of Crystallography. (B) Oxygen oversaturation in water and the gas concentration distribution map at 540 eV. Image adapted from [38] Copyright © American Chemical Society. 12

Figure 1.7 Schematic representation of (A) SiNx-LC, and (B) GLC. SiNx-LC offers better control over the liquid thickness and offers the possibility to accommodate MEMS devices, such as electrodes or heaters. GLC, on the other hand, offer higher spatial resolution. Image adapted from [61] Copyright © Royal Society of Chemistry. 14

Figure 1.8 TEM image of nanobubbles captured using (A) SiN_x-LC; and (B) GLC. 16

Figure 1.9 (A) Schematic of the pinned surface nanobubble. As $\theta > \theta e$, the nanobubble shrinks, and $\theta < \theta e$, the nanobubble grows. (B) Stable equilibrium θe for pinned surface nanobubble. (C) Unstable equilibrium Le for unpinned nanobubble. Image adapted from [68] Copyright © American Physical Society. 18

Figure 1.10 (A) Growth dynamics of a NB cluster stimulated via electron-beam radiolysis. (B) Scatter plot of the Knudsen number versus the density number ratio shows the dense nanobubbles. (C) Position-dependent growth of satellite nanobubbles. Image adapted from [35] Copyright © Royal Society of Chemistry. 19

Figure 1.11 (A) TEM images showing vanishing and stable nanobubbles and the Ostwald ripening and coalescence process in nanobubbles. Scale bar 5 nm. Image adapted from [37] Copyright © Nature Springer. (B) (top) Schematic of the nanobubble system confined within the rectangular box. (middle) Temporal evolution of the radius of the nanobubble obtained by solving the model developed in their work. (bottom) Temporal growth of nanobubble with initial radius 9 nm confined in the finite volume of the system, with length varying from 1000 nm to 20 nm. Image adapted from [71] Copyright © Nature Springer. 20

Figure 1.12 (A) Fresnel fringe method to determine the relative position of the bubble by varying the in-focus plane. Image adapted from [34] Copyright © Elsevier. (B) Heterogeneous and homogeneous nucleation in the upstream side of the electron beam observed. Image adapted from [72] Copyright © American Chemical Society. 21

Figure 1.13 (A) Silicon wafer with fabricated intricate features having critical dimensions in order of 10 nm (inset) for next generation electronics. IBM chip having embedded channels for thermal management. Image Copyright © ASML Holdings and IBM. (B) Early nucleation of bubble due to formation of nanobubbles after collapse of first bubble. The Y-axis here can be correlated with surface temperature. Image adapted form [78] Copyright © American Physical Society. (C) Bubble nucleus growing from possible ideal configurations of a vapor-trapping crevice via a pathway: without (left) and with surface nanobubbles. The solid curve shows the metastable nanobubbles already present at the surface. Image adapted form [79] Copyright © American Chemical Society. 23

Figure 1.14 Applications and technical relevance of surface nanobubbles. (A) Role of nanobubbles in separation of fine coal particles. Image adapted from [81] Copyright © Elsevier. (B) Role of nanobubbles in film rupture and microdroplet nucleation. Images adapted from [84,85] Copyright © American Chemical Society, American Physical Society. (C) Role of nanobubbles in cancer cell therapy. Image adapted form [96] Copyright © Theranostics. (D) Role of nanobubbles in inhibition of corrosion. Images adapted from [97] Copyright © Elsevier. 25

Figure 2.1 Experimental equipment for the nanobubble observation. (A) LPEM system: Poseidon Select, Protochips Inc. Scale bar: 2cm. (B) Magnified view of the tip of the LPEM system. Scale bar: 6 mm. Copyright © Protochips Inc., USA. (C) Representative images of e-chips used in the experiment. Image not to scale. (D) Large e-chip (grey triangle) and small e-chip (orange triangle) placed on a 1-Yen coin (∅ 20 mm). Scale bar: 5 mm. (E) Schematic image of the assembled liquid cell showing the encapsulated nanometre scale thin film between the e-chips. 33

Figure 2.2 Sequential snapshots of the nanobubbles' TEM image showing the results of various operation applied for the edge detection. (A) Raw image captured in RGB format. (B) RGB image converted to grey scale image. (C) Image contrast enhancement done using histogram equalisation. (D) Gaussian smoothening filter with standard deviation $\sigma = 10$ for noise reduction. (E) Detection of the nanobubbles' interfaces carried using Canny edge detection algorithm using sensitivity threshold $\vartheta = 0.4$. (F) Edge detected image and original image overlapping shows accurate edge detection. 35

Figure 2.3 (A) Schematic side view of the liquid cell used to observe nanobubbles and the region of view (top view) observed using TEM. (B) Schematic depicting the nanobubble nucleation pathway: heterogenous nucleation at the water-SiN_x interface due to the e-beam induced radiolysis and agglomeration of gaseous molecules at the solid surface. (C) The cumulative occurrence log of the nanobubbles observed during the experimentation. The improvement in the probability of occurrence due to the devised methodology can be seen after 9 attempts. (D) Snapshots of the nanobubbles observed during various experiments: (i) general view of the nanobubbles present on both the upper and the lower SiN_x window; (ii) excessive contamination observed in few experiments; (iii) nanobubbles exhibiting contrasting Fresnel fringes (dark and bright) due to their relative position with respect to the in-focus plane; (iv) isolated single nanobubble at least >150 nm away from the nearest nanobubble. Contaminations are also highlighted using yellow color in this frame. 37

Figure 2.4 (A) Representative image for nanobubbles nucleated using bright beam in the *Step 3* of the devised nucleation strategy. (B) Representative image for nanobubbles nucleated using dull beam in the *Step 3*. (C) Box plots for the nanobubbles' contact radii distribution for the exposure using high fluence beam and low fluence beam. The lower-upper quartile region is shown in the box. The mean radius for the observed nanobubbles using high fluence beam is ~19.5 nm, whereas, using low fluence beam, the mean radius is ~34.6 nm. 40

Figure 2.5 (A) TEM image showing the region of interest: nanobubbles A and B (in short: nbA and nbB). The initial distance between the three-phase contact lines of these nanobubbles is 20 nm. These surface nanobubbles are nucleated on the bottom SiN_x window. Few nanobubbles, present on the top SiN_x window, can also be seen in the TEM image. Red and blue bordered arrows are used to depict the bubbles at the bottom and top windows, respectively. (C) Side view representation of the TEM image in (B). The approximate focus plane during the imaging is also shown in the schematic. 41

Figure 2.6 Variation of mean radii of nanobubbles nbA and nbB during the complete observation of ~18 minutes. nbA exhibits high variations in its radius and is deemed as unpinned nanobubble. nbB has low variations due to the strong pinning of its contact line. Series of shrink-growth behavior of nbA were observed in the study, as depicted by dotted rectangles [I] – [V]. The merging of nanobubbles was observed at 1065 s. 42

Figure 2.7 Time sequence images demonstrating the interfacial interplay between nanobubbles observed using TEM. (A) TEM image showing the state of nanobubbles at t = 90 s. (B,C) The shrinking of nbA induces elongation in nbB, directed towards nbA. (D) The growth of nbA pushes the adjacent interface of nbB. (E,F) nbA and nbB demonstrating the pull-push phenomenon, induced due to the grow-shrink mechanism of nbA. Blue and Red arrows show the direction of the interface movement for nbA and nbB, respectively. (G) Temporal variation of nanobubble contact area for nbA and nbB. 44

Figure 2.8 Schematic of the observed nanobubble dynamics. (A) Due to the oversaturation, the bubble nbA and nbB grows. The gas flow direction is depicted by black arrows whereas the interface movement is depicted by red arrows. (B) The shrinkage in the nanobubbles in triggered by the cumulative effect of EDL, liquid thin film stability and the dynamic equilibrium of the nanobubbles. (C) As a reaction to the gas outflux in (B), the nanobubble starts to grow again after inhibiting further shrinkage. ..45

Figure 2.9 Anisotropic depinning of nanobubbles. (A) Temporal variation of circularity for nanobubble nbA and nbB. (B) Variation of the gap between the nanobubbles. (C) Feret angle and the angle formed by joining the centroids of nbA and nbB. The shaded region in (A), (B) and (C) highlights the directional deformation of the nbB induced due to nbA. 46

Figure 2.10 (A) Contact line of the nanobubbles traced for the first shrink-grow observation at the time: 111 s, 125 s and 137 s. nbA shows the pulsating behaviour, while the nbB shows depinning along edge adjacent to nbA and pinning along the opposite edge. (B) Contact line of nanobubbles for second shrink-grow observation at time: 155 s, 165 s and 175 s. Similar anisotropic depinning is observed in nbB. 48

Figure 2.11 (A) Schematic of the probable side view of the nanobubbles shows the shrinking of the nbA initiates the anisotropic depinning of nbB's three-phase contact line. (B) Role of increase in localized gas concentration in the anisotropic depinning of surface nanobubbles. The lighter blue region around the nbA shows the level of high gas concentration. 49

Figure 2.12 Time sequence snapshots of nbA and nbB for the time (A) 1014 s; (B) 1038 s; (C) 1065 s and (D) 1105 s. The blue and red arrows in (A) and (B) show the direction of the interface movement in nbA and nbB, respectively, whereas the pale markers in (C) shows the initiation of merging. The bubble merged after 18 minutes of observation. The shape of the bubble after merging verifies that the observed bubbles are surface nanobubbles. 51

Figure 2.13 (A) Variation of gap between the nanobubbles for time 0 s – 180 s (initial observation) and 950 s – 1065 s (before merging). The black arrow shows the increased gap due to the shrinking of nbA. The reduced repulsions between the interfaces have led to a decrease in the overall gap between the bubbles. (B) Variation of center-to-center distance between the nanobubbles for the complete 18 minutes of observation. The reduced repulsions between the nanobubbles due to the accumulative oversaturation increase are evident as the center-to-center distance decreases monotonically for the whole observation. 52

Figure 3.1 Schematic representation of (A) converging beam and (B) diverging electron beam irradiated on the sample using the TEM. 58

Figure 3.2 Sequential snapshots of the nanobubbles' TEM image showing the results of various operation applied for the edge detection. (A) Raw image captured in RGB. (B) RGB image converted to grey scale image. (C) Image contrast enhancement done using histogram equalisation. (D) Gaussian smoothening filter with standard deviation $\sigma = 12$ for noise reduction. (E) Efficient detection of the interface of the nanobubbles carried using canny edge detection algorithm. (F) The edge detected image fused with the Raw image for further analysis using image analysis package Fiji.[137]................59

Figure 3.3 (A) Schematic diagram of the liquid cell and the surface nanobubbles during the observation. The red-dashed line represents the region of interest i.e., the region between the adjacent interfaces of the nanobubbles. (B) Image frame from the TEM experiment showing nanobubbles P and Q. Scale bar: 20 nm...60

Figure 3.4 Time sequence of merging of nanobubbles observed using TEM for 220 s (A–L). Light Blue arrows show the bubble interface approaching during the initial phase. Light orange arrows show the increase in the local image intensity between the nanobubbles. Green arrow shows the increasing image intensity propagating in the plane parallel to the SiN_x window...62

Figure 3.5 (A) Image formed by overlapping the original RGB image with the edge detected binary image, showing the four specific segments: A, B, C, and D, where the distance was measured (B) Variation in the liquid film thickness between the nanobubbles P and Q measured at four distinguish segments. The highlighted region in each graph shows the fluctuations in the interfacial distance observed before merging. 63

Figure 3.6 Estimated profile of the region between the merging nanobubbles' interfaces based on the variation in the image intensity. The evolution of the intensity is shown for the line segments A, B, C and D (similar to **Figure**

3.5(A)) for the time 100–240 s. Inset in each plot shows the line segment along which the profile was plotted. 64

Figure 3.7 3D reconstruction of TEM phase contrast images. Dark region depicts the liquid phase, whereas the bright region depicts the gaseous phase. 3D reconstructions are shown for the TEM images present in presented in Figure 3.4. The light orange arrow in (F) highlights the initiation of gas layer formation, which then translates throughout the interfacial region, as depicted by the light blue arrows in (H). The gas layer then grows and completes the merging process, as depicted by green arrows in (L). 66

Figure 3.8 Pathway for the formation of a gas layer between two stable surface nanobubbles. (A) Electron beam increases the gas concentration of the irradiated region, leading to quasistatic expansion of the bubbles. (B) Gas molecules begin to accumulate at the solid surface between the two bubbles, forming an adsorbed layer. (C) Gas layer nucleates between the bubbles. (D) The nucleated gas layer grows while acting as a bridge between the two nanobubbles, thus completing the merging process. 68

Figure 3.9 Time sequence of merging process observed at higher electron intensity of ~2.8 A/cm^2. The nanobubbles have separate 3 phase contact line as highlighted by yellow arrow in (A). The initiation of the gas layer formation (C) and the successive merging was observed to be much faster when compared to the merging observed at a relatively weaker electron intensity of ~0.3 A/cm^2. 69

Figure 3.10 Time sequence imaging for the merging phenomenon in 5 adjacent nanobubbles imaged for 100 seconds. (A) The merging initiated by the formation of gas film between the nanobubbles. (B-E) The gas film grows, thus forming the flat nanobubble. (F-K) Slow evolution of the contact line during the interface relaxation of the merged nanobubble. (L) Interface evolution of the nanobubbles. Scale bar: 50 nm. 71

Figure 3.11 Schematic for the simultaneous merging of five nanobubbles. Merging process here resembles the merging in a nanobubble pair. The growth and evolution of gas layer leads to the formation of larger bubble having lower internal pressure. 72

Figure 4.1 Laser induced bubble assisted fabrication. (A) Bubble-pen lithography using plasmonic bubbles to form nanopatterns from colloidal particles. Image adapted from [195] Copyright © American Society of Chemistry. (B) High resolution bubble printing of quantum dots and patterning. Image adapted from [196] Copyright © American Society of Chemistry. (C) Ring structured fabrication of nanoparticles on gold surface using laser-induced micro-nanobubbles and the Marangoni convection and capillary flow around it. Image adapted from [197] Copyright ©

American Society of Chemistry. (D) Particle accumulation due to the convection flow around the continuous wave laser induced vapor bubble. Image adapted from [198] Copyright Royal Society of Chemistry. 77

Figure 4.2 Schematic for the liquid cell and beam-stage relative movement to nucleate and pattern nanobubbles. 79

Figure 4.3 TEM imagery showcasing the nucleation of nanobubbles during formation of patterns. (A) Opening of the TEM camera shutter. (B) Bubbles already nucleated by converging electron beam, prior to insertion of camera. (C) Evolution of bubbles began due to prolonged exposure. (D, E, F) Multiple nascent bubble nucleation. 80

Figure 4.4 (A) Schematic for the methodology to print nanobubbles on a surface using electron beam. (B) Dimensions of the initials of Kyushu University: KU written on the surface. (C) TEM image of the KU written from nanobubbles by controlling the sample using the TEM's trackball. 81

Figure 4.5 Stability of pattern in time due to nanobubble longevity. TEM images of small "n" nanobubble pattern at (A) Initial; (B) 29 s; (C) 984 s; (D) 1677 s; and (E) 3171 s. The information about the time of acquisition and magnification is embedded in the image frames. 82

Figure 4.6 Stability of nanobubbles in flow. The variation in the intensity of region pointed by the arrow is an indicator for flow. 83

Figure 4.7 Proposed applications for nanobubble patterns. (A) Template for nanofabrication by agglomerating nanoparticles at liquid-gas interfaces. (B) High ionic concentration domains formed due to agglomeration of ions around a nanobubble in an ionic liquid. (C) Corrosion inhibition and 3-D patterns formation due to the protection offered by nanobubbles due to their longevity and stability at numerous conditions. 84

List of Tables

Table 1.1 Comparison of characteristics of GLCs and SiN_x-LCs 15

Table 1.2 Comparison of various experimentation capabilities of techniques used for observing surface nanobubbles 17

Table 3.1 Effect of electron beam intensity on the nanobubble coalescence time 70

Supplementary Information

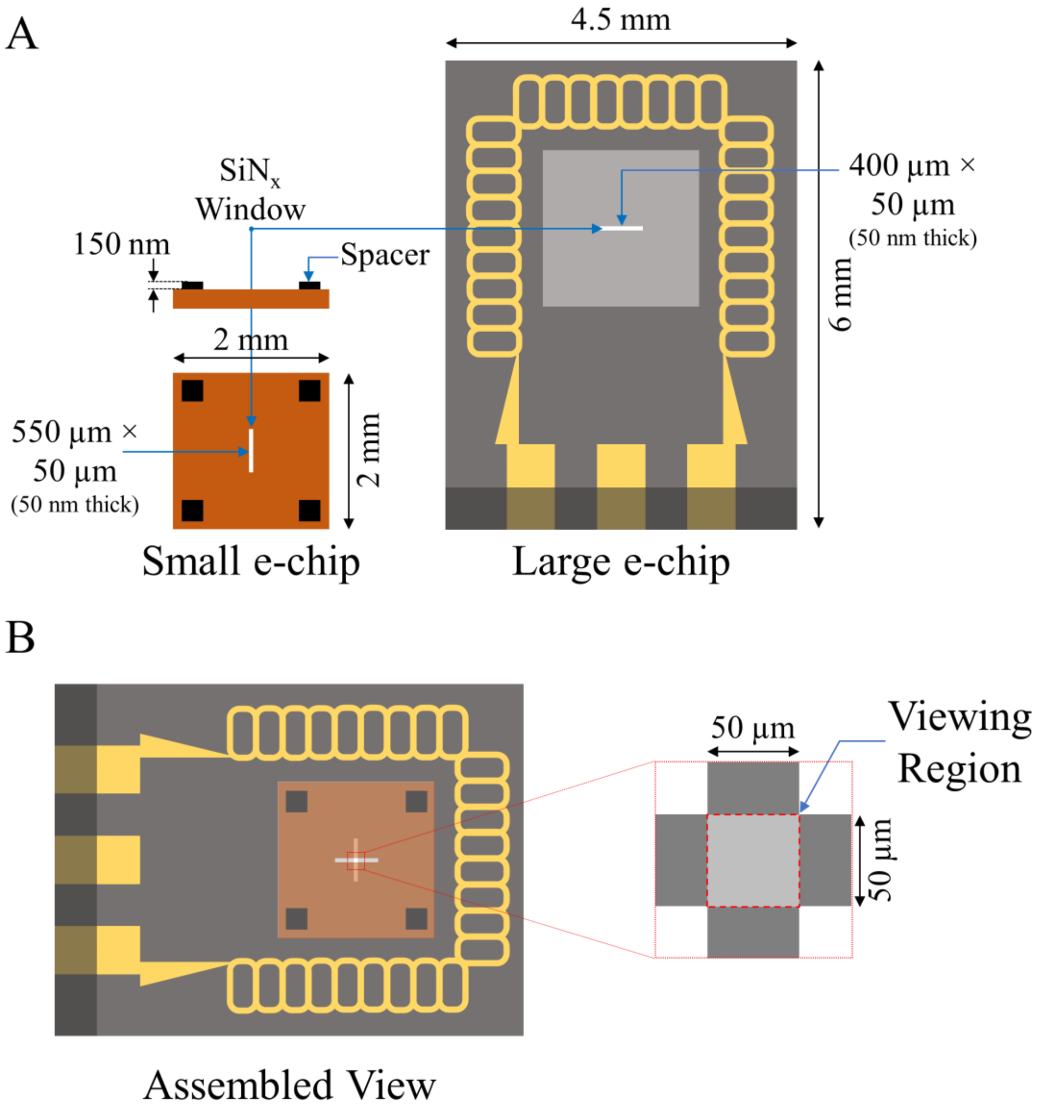

Figure S1 Detailed description of the e-chips used in the experiment. (A) Small e-chip (2 mm × 2 mm × 300 µm) and Large e-chip (4.5 mm × 6 mm × 300 µm). The suspended SiN$_x$ window is present at the central region of the e-chips. The dimensions of the SiN$_x$ windows are given in the figure. (B) Assembled view of e-chips. Due to the cross-alignment of windows, the viewing region in 50 µm × 50 µm.

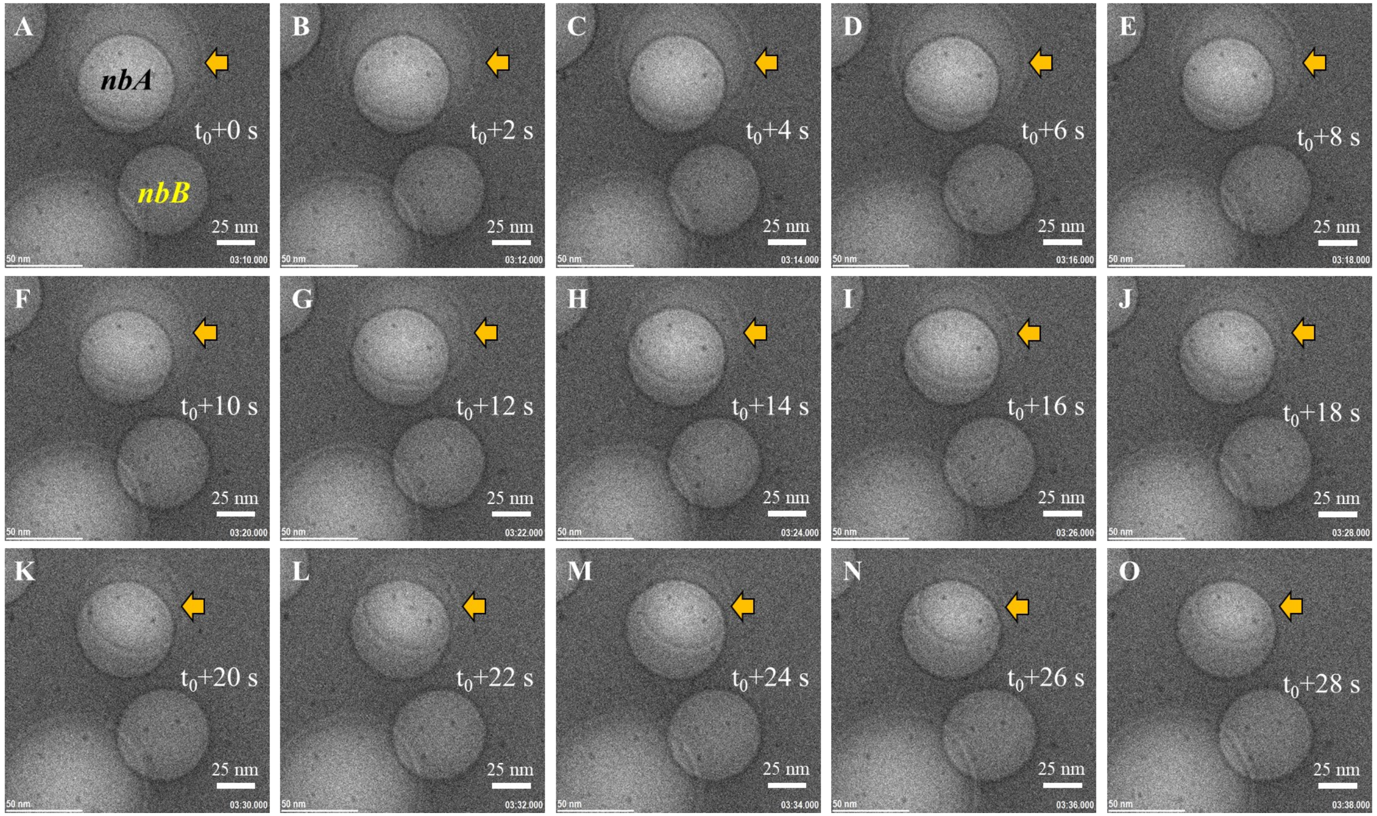

Figure S2 Time sequence TEM images of the nanobubbles nbA, nbB and the other nanobubbles (Chapter 2) observed on the adjacent SiN_x window. Yellow arrow marks the contact line of the nanobubble present on the top window. As this nanobubble shrinks, no changes were observed in the size of nbA. This demonstrates that the behaviour of the top bubble does not induce any remarkable size changes in nbA persistently, and the interactions between nbA and nbB are stronger due to lower interfacial distance.

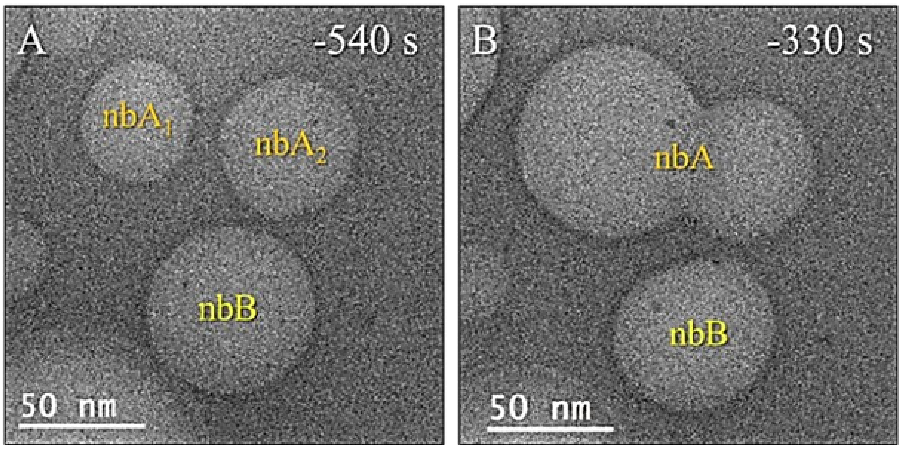

Figure S3 Time history of the nanobubbles A and B. (A) Nanobubble nbA was formed after the coalescence of nbA1 and nbA2. (B) nbA during the merging process of its two constituent nanobubbles. The shape formed by nbA during merging reverifies that the formed bubble is a surface nanobubble. nbB is a pinned surface nanobubble, exhibiting deformation induced due to its neighboring nanobubbles. Scale bar: 50 nm.

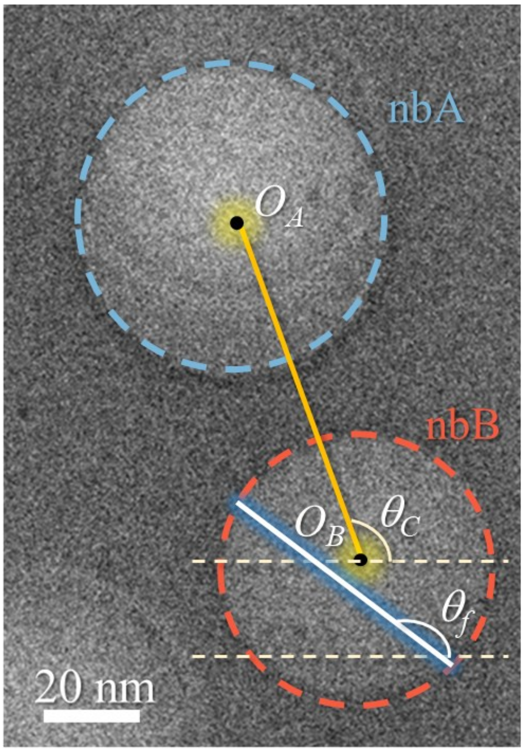

Figure S4 Reference image showing the measured parameters in **Figure 2.9**. OA and OB are the centroids of nbA and nbB, respectively. θ_f and θ_c are the feret angle and the centroid angle, respectively.

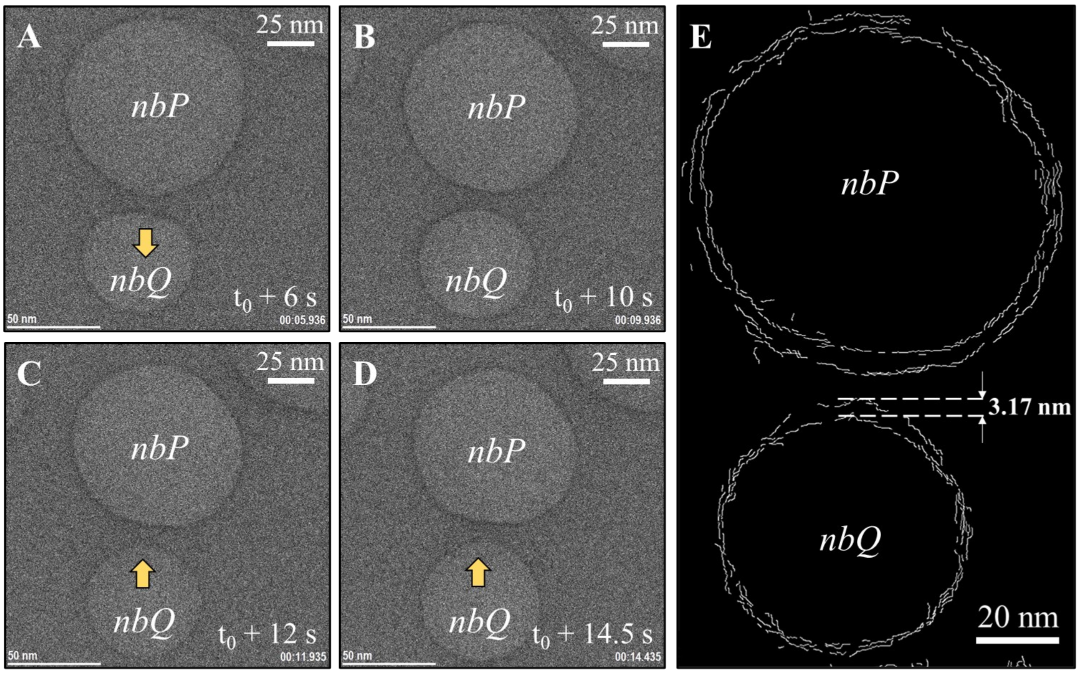

Figure S5 (A-D) Time sequence TEM images of the observed pull-push phenomenon observed in another nanobubble pair (nbP and nbQ). The yellow arrow shows the direction of the contact line's movement and distortion in nanobubble induced due to the growth and shrinking of the other nanobubble. The magnitude of the depinning in the bubble was observed to be less as compared to the results discussed in the manuscript, possibly due to the lower oversaturation. In the presented images, the electron beam intensity measured was ~0.32 A/cm^2, while for the images presented in the main manuscript, the electron beam intensity was ~1.03 A/cm^2. Scale bar: 25 nm. (E) Edge detected overlapped image of the nanobubbles observed at $t=t_0+10$ s and $t = t_0+14.5$ s. The extend of depinning is highlighted in the image. Scale bar: 20 nm.

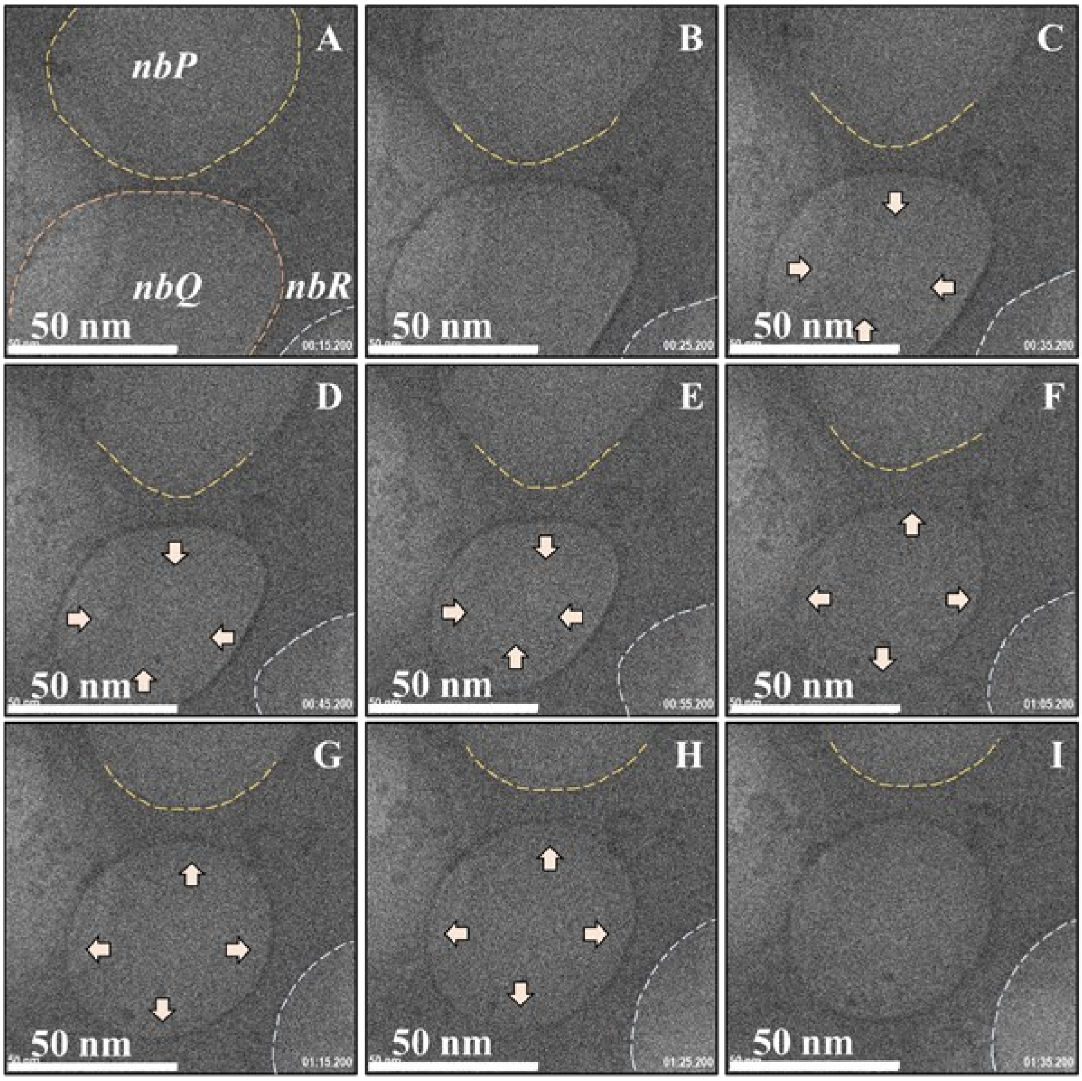

Figure S6 (A-I) Time sequence TEM images of three nanobubbles demonstrating anisotropic depinning. The time interval between each image frame is 10 s. The initial positions of the 3-phase contact lines of nanobubbles P,Q and R are shown in (A). Nanobubble Q begins shrinking, which leads to the distortion in the adjacent interfaces of nanobubble P and R, as shown in (C), (D) and (E). After ~ 50 s, nanobubble Q exhibits growth, as shown in (F-H), which increases the circularity of the 3-phase contact line of nanobubble P and R. Scale bar: 50 nm.

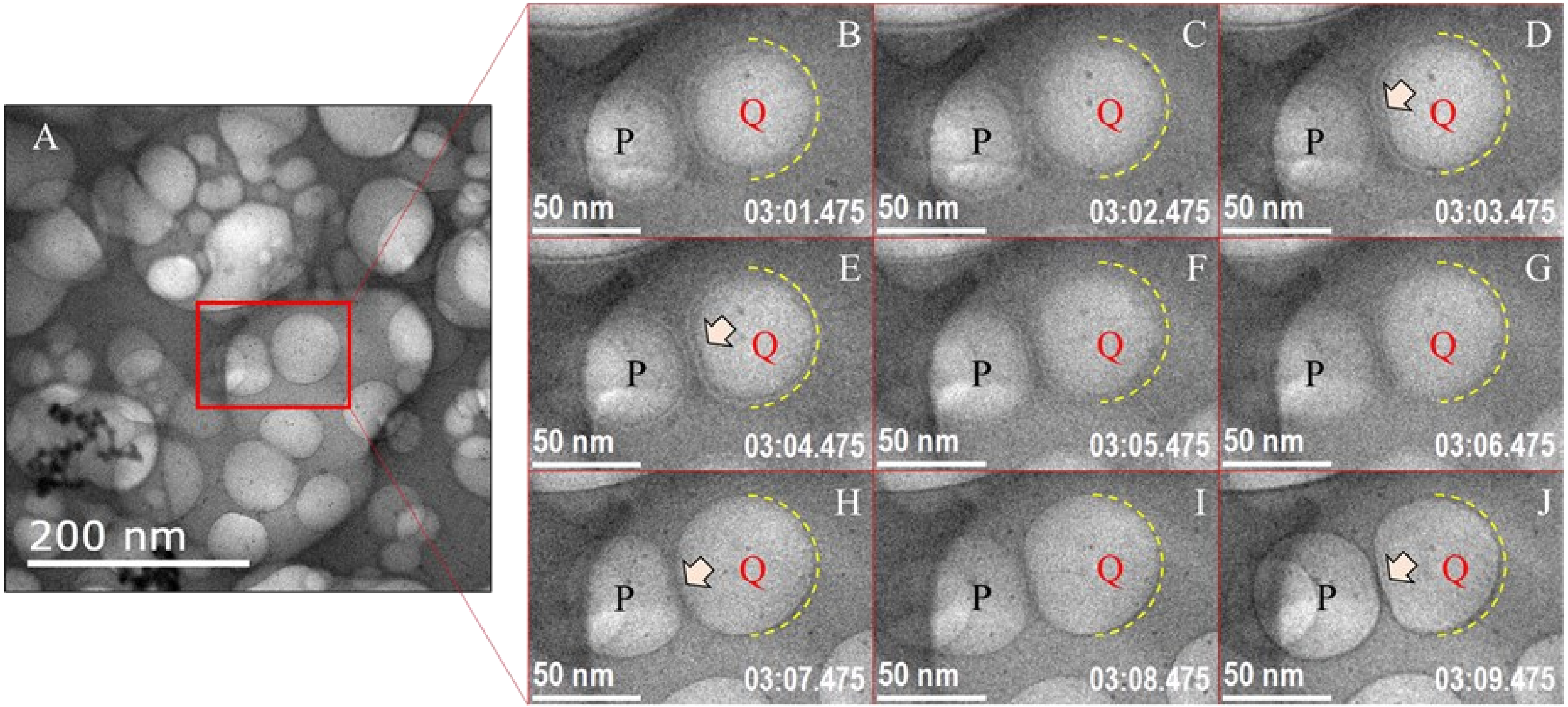

Figure S7 (A) TEM image of multiple nanobubbles nucleated in a single image frame. Scale Bar: 200 nm. (B-J) Time sequence TEM images of two nanobubbles (P and Q) exhibiting pull-push phenomenon. Images (B-G) are captured while the bubbles are over-focus (bright fringes around the bubble), whereas images (H-J) are captured while the bubbles are under-focus (dark fringes). The yellow dotted curve highlights the pinned three-phase contact line of nanobubble Q. Due to the size fluctuations of P, distortion in the three-phase contact line of nanobubble Q close to the nanobubble P is observed, which has been highlighted by an arrow in (D, E, H and J). Scale bar: 50 nm.

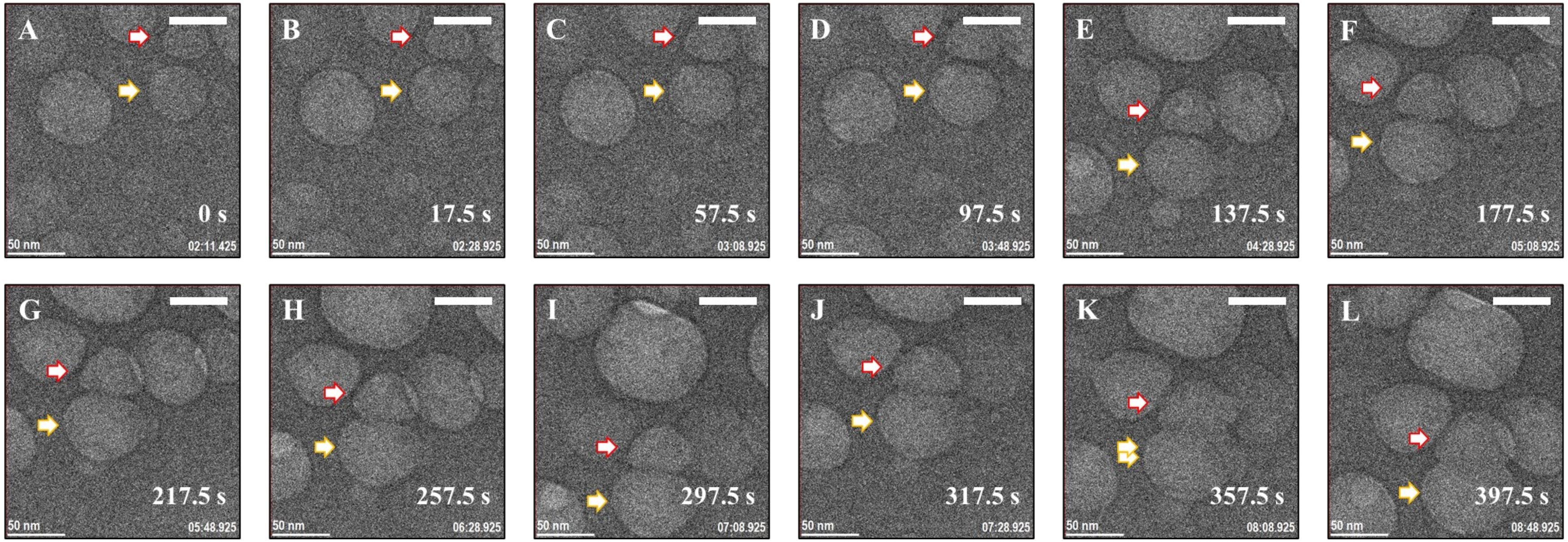

Figure S8 Gas layer mediate merging of surface nanobubbles observed at 0.07 A/cm^2 electron beam intensity. The nanobubbles of interest are highlighted by Red and Yellow arrows. The repulsions between the bubbles' interface flattens their respective contact lines (A-C) followed by the gas film formation (D-F), and gas film growth (G-J) before the merging is completed (K-L). The coalescence time for this observation was ~ 323±61 s due to the very low electron beam intensity.

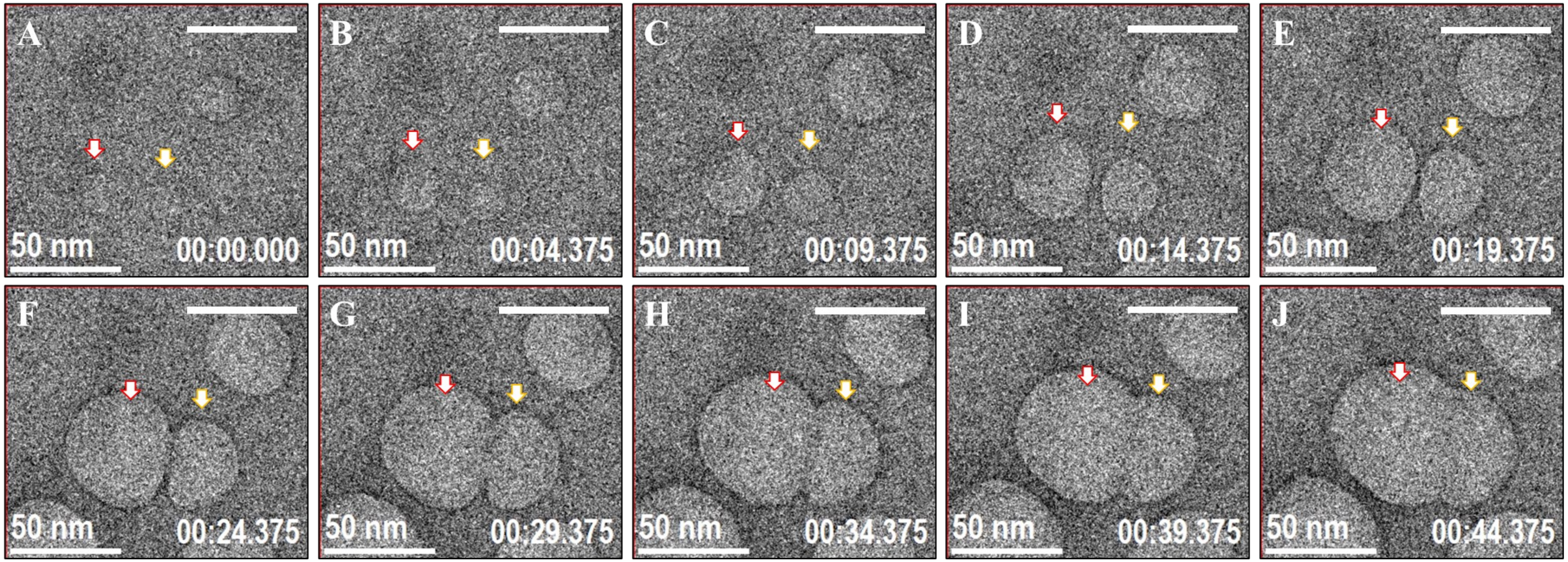

Figure S9 Gas layer mediate merging of surface nanobubbles observed at 0.87 A/cm^2 electron beam intensity. The nanobubbles of interest are highlighted by Red and Yellow arrows. As the size of the bubbles increase, the separation distance between the bubbles decrease (A-C). The repulsions between the bubbles' interface also becomes dominant and their contact line flattens (D) followed by the gas film formation (E-F), and gas film growth (G-I) before the merging is completed (J). The coalescence time for this observation was ~ 21±6 s.

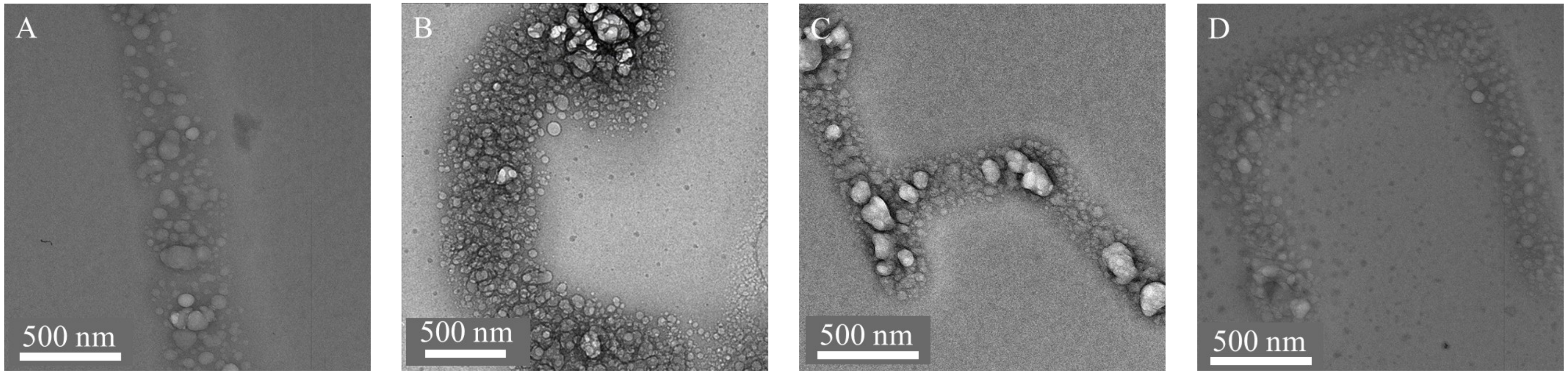

Figure S10 Nanobubble pattern made in the shape of English language letters (A) capital " I" ; (B) capital " C" ; (C) small " h" and (D) small " n" .

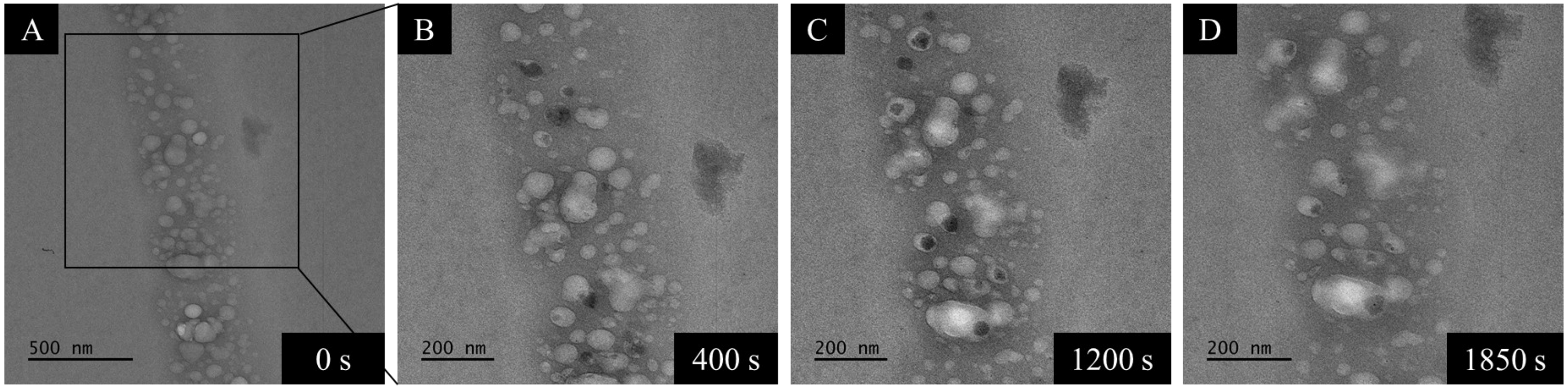

Figure S11 Stability of pattern " I" at time (A) Initial; (B) 400 s; (C) 1200 s; (D) 1850 s. Scale Bar: (A) 500 nm; (B,C,D) 200 nm.

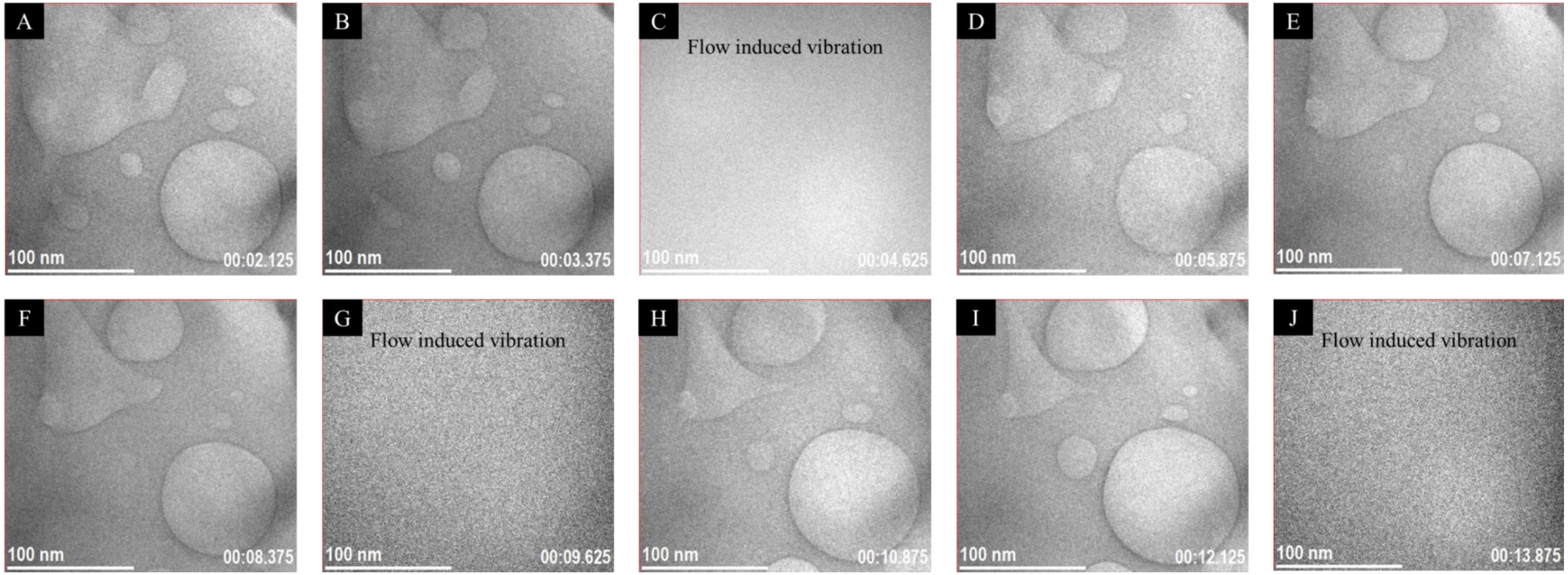

Figure S12 Stability of nanobubbles in presence of liquid flow. Frame (C, G & J) shows no imaging of nanobubbles possibly due to the vibration and momentrily increase in liquid thickness during the flow condition.

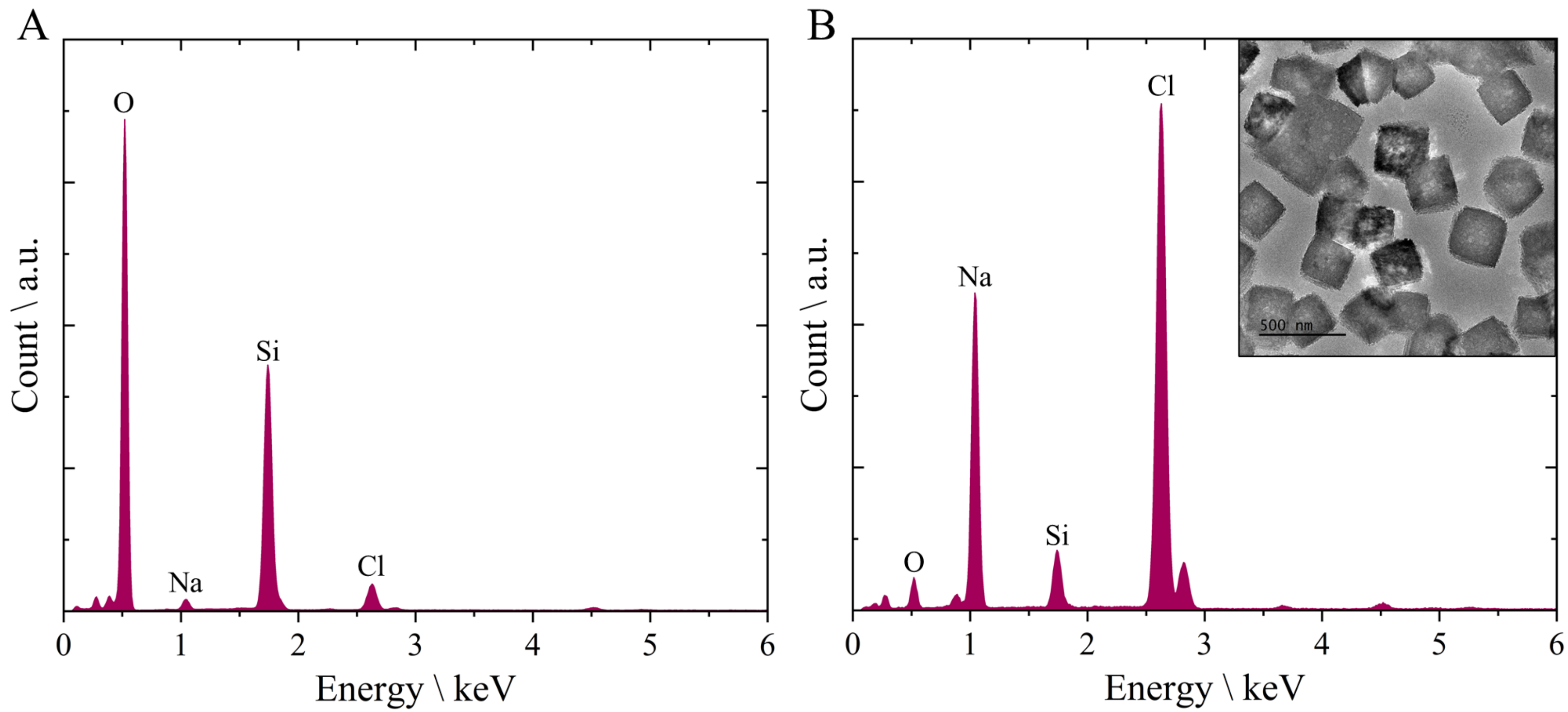

Figure S13 (A) EDS spectrum for NaCl solution encapsulated in the liquid cell. (B) EDS spectrum after the crystallisation of the salt (see inset) occurs. O peak in both the spectra depicts the presence of water.

Bibliography

1. Feynman, R. P. The Wonders That Await a Micro-Microscope. *The Saturday Review* 45–47 (1960).
2. The Nobel Prize in Physics 1986. *NobelPrize.org* https://www.nobelprize.org/prizes/physics/1986/summary/.
3. Bocquet, L. & Charlaix, E. Nanofluidics, from bulk to interfaces. *Chem. Soc. Rev.* **39**, 1073–1095 (2010).
4. Bocquet, L. Nanofluidics coming of age. *Nat. Mater.* **19**, 254–256 (2020).
5. Bocquet, L. & Tabeling, P. Physics and technological aspects of nanofluidics. *Lab Chip* **14**, 3143–3158 (2014).
6. Tu, Q., Yang, Q., Wang, H. & Li, S. Rotating carbon nanotube membrane filter for water desalination. *Sci. Reports 2016 61* **6**, 1–11 (2016).
7. Liang, X. & Chou, S. Y. Nanogap Detector Inside Nanofluidic Channel for Fast Real-Time Label-Free DNA Analysis. *Nano Lett.* **8**, 1472–1476 (2008).
8. Rabinowitz, J. *et al.* Nanobubble-controlled nanofluidic transport. *Sci. Adv.* **6**, 126–139 (2020).
9. Ross, F. M. Liquid Cell Electron Microscopy. in (Cambridge University Press, 2017). doi:10.1017/9781316337455.
10. Alheshibri, M., Qian, J., Jehannin, M. & Craig, V. S. J. A History of Nanobubbles. *Langmuir* **32**, 11086–11100 (2016).
11. Epstein, P. S. & Plesset, M. S. On the stability of gas bubbles in liquid-gas solutions. *J. Chem. Phys.* **18**, 1505–1509 (1950).
12. Degens, E. T., von Herzen, R. P., Wong, H.-K., Deuser, W. G. & Jannasch, H. W. Lake Kivu: structure, chemistry and biology of an East African rift lake. *Geol. Rundschau* **62**, 245–277 (1973).
13. Johnson, B. D. & Cooke, R. C. Generation of Stabilized Microbubbles in Seawater. *Science (80-.).* **213**, 209–211 (1981).
14. Thome, J. R. & Dupont, V. Bubble generator. (2007).
15. Paul, S. *et al.* Single-bubble dynamics in nanopores: Transition between homogeneous and heterogeneous nucleation. *Phys. Rev. Res.* **2**, 043400 (2020).
16. Lombard, J., Lam, J., Detcheverry, F., Biben, T. & Merabia, S. Strong and fast rising pressure waves emitted by plasmonic vapor nanobubbles. *Phys. Rev. Res.* **3**, 023231 (2021).
17. Uchida, T. *et al.* Effect of NaCl on the Lifetime of Micro- and Nanobubbles. *Nanomaterials*

6, 31 (2016).

18. Borkent, B. M., Beer, S. de, Mugele, F. & Lohse, D. On the Shape of Surface Nanobubbles. *Langmuir* **26**, 260–268 (2009).

19. Israelachvili, J. & Pashley, R. The hydrophobic interaction is long range, decaying exponentially with distance. *Nature* **300**, 341–342 (1982).

20. Parker, J. L., Claesson, P. M. & Attard, P. Bubbles, cavities, and the long-ranged attraction between hydrophobic surfaces. *J. Phys. Chem.* **98**, 8468–8480 (1994).

21. Ljunggren, S. & Eriksson, J. C. The lifetime of a colloid-sized gas bubble in water and the cause of the hydrophobic attraction. *Colloids Surfaces A Physicochem. Eng. Asp.* **129–130**, 151–155 (1997).

22. Naoyuki Ishida, Taichi Inoue, Minoru Miyahara, A. & Higashitani, K. Nano Bubbles on a Hydrophobic Surface in Water Observed by Tapping-Mode Atomic Force Microscopy. *Langmuir* **16**, 6377–6380 (2000).

23. Zhang, X. H., Maeda, N. & Craig, V. S. J. Physical Properties of Nanobubbles on Hydrophobic Surfaces in Water and Aqueous Solutions. *Langmuir* **22**, 5025–5035 (2006).

24. Borkent, B. M., Dammer, S. M., Schönherr, H., Vancso, G. J. & Lohse, D. Superstability of Surface Nanobubbles. *Phys. Rev. Lett.* **98**, 204502 (2007).

25. Sun, Y., Xie, G., Peng, Y., Xia, W. & Sha, J. Stability theories of nanobubbles at solid–liquid interface: A review. *Colloids Surfaces A Physicochem. Eng. Asp.* **495**, 176–186 (2016).

26. Petsev, N. D., Shell, M. S. & Leal, L. G. Dynamic equilibrium explanation for nanobubbles' unusual temperature and saturation dependence. *Phys. Rev. E* **88**, 010402 (2013).

27. Brenner, M. P. & Lohse, D. Dynamic Equilibrium Mechanism for Surface Nanobubble Stabilization. *Phys. Rev. Lett.* **101**, 214505 (2008).

28. Ducker, W. A. Contact Angle and Stability of Interfacial Nanobubbles. *Langmuir* **25**, 8907–8910 (2009).

29. Weijs, J. H. & Lohse, D. Why Surface Nanobubbles Live for Hours. *Phys. Rev. Lett.* **110**, 054501 (2013).

30. Zhang, X., Chan, D. Y. C., Wang, D. & Maeda, N. Stability of Interfacial Nanobubbles. *Langmuir* **29**, 1017–1023 (2013).

31. White, E. R., Mecklenburg, M., Singer, S. B., Aloni, S. & Regan, B. C. Imaging nanobubbles in water with scanning transmission electron microscopy. *Appl. Phys. Express* **4**, 055201 (2011).

32. Karpitschka, S. *et al.* Nonintrusive Optical Visualization of Surface Nanobubbles. *Phys. Rev. Lett.* **109**, 066102 (2012).

33. Chan, C. U. & Ohl, C.-D. D. Total-internal-reflection-fluorescence microscopy for the study of nanobubble dynamics. *Phys. Rev. Lett.* **109**, 174501 (2012).

34. Tomo, Y., Takahashi, K., Nishiyama, T., Ikuta, T. & Takata, Y. Nanobubble nucleation studied using Fresnel fringes in liquid cell electron microscopy. *Int. J. Heat Mass Transf.* **108**, 1460–1465 (2017).

35. Huang, T.-W. *et al.* Dynamics of hydrogen nanobubbles in KLH protein solution studied with in situ wet-TEM. *Soft Matter* **9**, 8856–8861 (2013).

36. Park, J. B., Shin, D., Kang, S., Cho, S. P. & Hong, B. H. Distortion in Two-Dimensional

Shapes of Merging Nanobubbles: Evidence for Anisotropic Gas Flow Mechanism. *Langmuir* **32**, 11303–11308 (2016).

37. Shin, D. *et al.* Growth dynamics and gas transport mechanism of nanobubbles in graphene liquid cells. *Nat. Commun.* **6**, 1–6 (2015).

38. Zhou, L. *et al.* Ultrahigh Density of Gas Molecules Confined in Surface Nanobubbles in Ambient Water. *J. Am. Chem. Soc.* **142**, 5583–5593 (2020).

39. Lou, S.-T. *et al.* Nanobubbles on solid surface imaged by atomic force microscopy. *J. Vac. Sci. Technol. B Microelectron. Nanom. Struct. Process. Meas. Phenom.* **18**, 2573 (2000).

40. Giessibl, F. J. Advances in atomic force microscopy. *Rev. Mod. Phys.* **75**, 949 (2003).

41. Teshima, H. 固液界面ナノバブルと吸着気体分子層に関する実験的研究. (Kyushu University, 2019).

42. Lohse, D. & Zhang, X. Surface nanobubbles and nanodroplets. *Rev. Mod. Phys.* **87**, 981 (2015).

43. Teshima, H., Takahashi, K., Takata, Y. & Nishiyama, T. Wettability of AFM tip influences the profile of interfacial nanobubbles. *J. Appl. Phys.* **123**, 054303 (2018).

44. Walczyk, W., Hain, N. & Schönherr, H. Hydrodynamic effects of the tip movement on surface nanobubbles: a combined tapping mode, lift mode and force volume mode AFM study. *Soft Matter* **10**, 5945–5954 (2014).

45. Ding, S. *et al.* New Insights into the Role of Surface Nanobubbles in Bubble-Particle Detachment. *Langmuir* **36**, 4339–4346 (2020).

46. Tan, B. H., An, H. & Ohl, C. D. Resolving the Pinning Force of Nanobubbles with Optical Microscopy. *Phys. Rev. Lett.* **118**, 054501 (2017).

47. Zhang, L. *et al.* Imaging interfacial micro-and nano-bubbles by scanning transmission soft X-ray microscopy. *J. Synchrotron Radiat.* **20**, 413–418 (2013).

48. Wang, S. *et al.* Force Spectroscopy Revealed a High-Gas-Density State near the Graphite Substrate inside Surface Nanobubbles. *Langmuir* **35**, 2498–2505 (2019).

49. Pan, G. *et al.* Nanobubbles at Hydrophilic Particle–Water Interfaces. *Langmuir* **32**, 11133–11137 (2016).

50. Ruska, E. Beitrag zur übermikroskopischen Abbildung bei höheren Drucken. *Kolloid-Zeitschrift 1942 1002* **100**, 212–219 (1942).

51. Ross, F. M. Opportunities and challenges in liquid cell electron microscopy. *Science (80-.).* **350**, (2015).

52. Parsons, D. F. Structure of Wet Specimens in Electron Microscopy. *Science (80-.).* **186**, 407–414 (1974).

53. Yang, J. *et al.* Amorphous-Phase-Mediated Crystallization of Ni Nanocrystals Revealed by High-Resolution Liquid-Phase Electron Microscopy. *J. Am. Chem. Soc.* **141**, 763–768 (2019).

54. Luo, B., Smith, J. W., Ou, Z. & Chen, Q. Quantifying the Self-Assembly Behavior of Anisotropic Nanoparticles Using Liquid-Phase Transmission Electron Microscopy. *Acc. Chem. Res.* **50**, 1125–1133 (2017).

55. Cepeda-Pérez, E. & de Jonge, N. Dynamics of gold nanoparticle clusters observed with liquid-phase electron microscopy. *Micron* **117**, 68–75 (2019).

56. Kashin, A. S. & Ananikov, V. P. Monitoring chemical reactions in liquid media using electron microscopy. *Nat. Rev. Chem.* **3**, 624–637 (2019).

57. Nakamuro, T., Sakakibara, M., Nada, H., Harano, K. & Nakamura, E. Capturing the Moment of Emergence of Crystal Nucleus from Disorder. *J. Am. Chem. Soc.* **143**, 1763–1767 (2021).

58. de Jonge, N. & Ross, F. M. Electron microscopy of specimens in liquid. *Nat. Nanotechnol.* **6**, 695–704 (2011).

59. Ghodsi, S. M. *et al.* Assessment of Pressure and Density of Confined Water in Graphene Liquid Cells. *Adv. Mater. Interfaces* **7**, 1901727 (2020).

60. Park, J. *et al.* Graphene Liquid Cell Electron Microscopy: Progress, Applications, and Perspectives. *ACS Nano* **15**, 288–308 (2021).

61. Liao, H. G., Niu, K. & Zheng, H. Observation of growth of metal nanoparticles. *Chem. Commun.* **49**, 11720–11727 (2013).

62. Yuk, J. M. *et al.* High-Resolution EM of Colloidal Nanocrystal Growth Using Graphene Liquid Cells. *Science (80-.).* **335**, 61–64 (2012).

63. Wang, H., Li, B., Kim, Y.-J., Kwon, O.-H. & Granick, S. Intermediate states of molecular self-assembly from liquid-cell electron microscopy. *Proc. Natl. Acad. Sci.* **117**, 1283–1292 (2020).

64. Hirokawa, S. *et al.* Pinning in a Contact and Noncontact Manner: Direct Observation of a Three-Phase Contact Line Using Graphene Liquid Cells. *Langmuir* (2021) doi:10.1021/ACS.LANGMUIR.1C01589.

65. Wu, H., Friedrich, H., Patterson, J. P., Sommerdijk, N. A. J. M. & Jonge, N. de. Liquid-Phase Electron Microscopy for Soft Matter Science and Biology. *Adv. Mater.* **32**, 2001582 (2020).

66. Schneider, N. M. *et al.* Electron-Water interactions and implications for liquid cell electron microscopy. *J. Phys. Chem. C* **118**, 22373–22382 (2014).

67. Parent, L. R., Gnanasekaran, K., Korpanty, J. & Gianneschi, N. C. 100th Anniversary of Macromolecular Science Viewpoint: Polymeric Materials by In Situ Liquid-Phase Transmission Electron Microscopy. *ACS Macro Lett.* **10**, 14–38 (2020).

68. Lohse, D. & Zhang, X. Pinning and gas oversaturation imply stable single surface nanobubbles. *Phys. Rev. E* **91**, 031003 (2015).

69. Tan, B. H., An, H. & Ohl, C. D. Stability, Dynamics, and Tolerance to Undersaturation of Surface Nanobubbles. *Phys. Rev. Lett.* **122**, 134502 (2019).

70. Choi, H., Li, C. & Peterson, G. P. Dynamic Processes of Nanobubbles: Growth, Collapse, and Coalescence. *J. Heat Transfer* **143**, (2021).

71. Kim, Qh., Shin, D., Park, J., Weitz, D. A. & Jhe, W. Initial growth dynamics of 10 nm nanobubbles in the graphene liquid cell. *Appl. Nanosci.* **1**, 1–7 (2018).

72. Tomo, Y., Li, Q. Y., Ikuta, T., Takata, Y. & Takahashi, K. Unexpected Homogeneous Bubble Nucleation near a Solid-Liquid Interface. *J. Phys. Chem. C* **122**, 28712–28716 (2018).

73. Bae, Y. *et al.* Nanobubble Dynamics in Aqueous Surfactant Solutions Studied by Liquid-Phase Transmission Electron Microscopy. *Engineering* **7**, 630–635 (2021).

74. Wen, R., Ma, X., Lee, Y. C. & Yang, R. Liquid-Vapor Phase-Change Heat Transfer on Functionalized Nanowired Surfaces and Beyond. *Joule* **2**, 2307–2347 (2018).

75. Ritchie, H. & Roser, M. Energy - Electricity Mix. *Our World in Data* https://ourworldindata.org/electricity-mix (2020).

76. Jones, N. How to stop data centres from gobbling up the world's electricity. *Nature* **561**, 163–166 (2018).

77. Tafani, D., Mouftah, H. T., Kantarci, B., McArdle, C. & Barry, L. P. Towards energy efficiency for cloud computing services. in *Communication Infrastructures for Cloud Computing* (eds. Mouftah, H. T. & Kantarci, B.) 306–328 (IGI Global, 2013). doi:10.4018/978-1-4666-4522-6.CH014.

78. Cavicchi, R. E. & Avedisian, C. T. Bubble nucleation and growth anomaly for a hydrophilic microheater attributed to metastable nanobubbles. *Phys. Rev. Lett.* **98**, 124501 (2007).

79. Zou, J. *et al.* Surface Nanobubbles Nucleate Liquid Boiling. *Langmuir* **34**, 14096–14101 (2018).

80. Gong, W., Stearnes, J., Fornasiero, D., Hayes, R. A. & Ralston, J. The influence of dissolved gas on the interactions between surfaces of different hydrophobicity in aqueous media Part II. A spectroscopic study. *Phys. Chem. Chem. Phys.* **1**, 2799–2803 (1999).

81. Li, C., Xu, M., Xing, Y., Zhang, H. & Peuker, U. A. Efficient separation of fine coal assisted by surface nanobubbles. *Sep. Purif. Technol.* **249**, 117163 (2020).

82. Temesgen, T., Bui, T. T., Han, M., Kim, T. il & Park, H. Micro and nanobubble technologies as a new horizon for water-treatment techniques: A review. *Adv. Colloid Interface Sci.* **246**, 40–51 (2017).

83. Etchepare, R., Oliveira, H., Azevedo, A. & Rubio, J. Separation of emulsified crude oil in saline water by dissolved air flotation with micro and nanobubbles. *Sep. Purif. Technol.* **186**, 326–332 (2017).

84. Stöckelhuber, K. W., Radoev, B., Wenger, A. & Schulze, H. J. Rupture of Wetting Films Caused by Nanobubbles. *Langmuir* **20**, 164–168 (2003).

85. Zhang, X., Lhuissier, H., Sun, C. & Lohse, D. Surface Nanobubbles Nucleate Microdroplets. *Phys. Rev. Lett.* **112**, 144503 (2014).

86. Shen, B. *et al.* Early Onset of Nucleate Boiling on Gas-covered Biphilic Surfaces. *Sci. Reports 2017 71* **7**, 1–15 (2017).

87. Forest, T. W. & Ward, C. A. Effect of a dissolved gas on the homogeneous nucleation pressure of a liquid. *J. Chem. Phys.* **66**, 2322 (2008).

88. Zhang, X. & Lohse, D. Perspectives on surface nanobubbles. *Biomicrofluidics* **8**, 1505 (2014).

89. Fan, Y. W. & Wang, R. Z. Submicrometer-Sized Vaterite Tubes Formed Through Nanobubble-Templated Crystal Growth. *Adv. Mater.* **17**, 2384–2388 (2005).

90. Hui, F., Li, B., He, P., Hu, J. & Fang, Y. Electrochemical fabrication of nanoporous polypyrrole film on HOPG using nanobubbles as templates. *Electrochem. commun.* **11**, 639–642 (2009).

91. Liu, G., Wu, Z. & Craig, V. S. J. Cleaning of Protein-Coated Surfaces Using Nanobubbles: An Investigation Using a Quartz Crystal Microbalance. *J. Phys. Chem. C* **112**, 16748–16753 (2008).

92. Wu, Z. H. *et al.* Cleaning using nanobubbles: Defouling by electrochemical generation of bubbles. *J. Colloid Interface Sci.* **328**, 10–14 (2008).

93. Steinfeld, A. Solar thermochemical production of hydrogen––a review. *Sol. Energy* **78**, 603–615 (2005).

94. Suslick, K. S. & Price, G. J. Applications of ultrasound to material chemistry. *Annu. Rev. Mater. Sci.* **29**, 295–326 (1999).

95. Halas, N. J., Lal, S., Chang, W.-S., Link, S. & Nordlander, P. Plasmons in Strongly Coupled Metallic Nanostructures. *Chem. Rev.* **111**, 3913–3961 (2011).

96. Huang, W. T., Chan, M. H., Chen, X., Hsiao, M. & Liu, R. S. Theranostic nanobubble encapsulating a plasmon-enhanced upconversion hybrid nanosystem for cancer therapy. *Theranostics* **10**, 782–796 (2020).

97. Aikawa, A., Kioka, A., Nakagawa, M. & Anzai, S. Nanobubbles as corrosion inhibitor in acidic geothermal fluid. *Geothermics* **89**, 101962 (2021).

98. Hatano, M. *et al.* NIL defect performance toward high volume mass production. in *Alternative Lithographic Technologies VIII* vol. 9777 31–36 (SPIE, 2016).

99. German, S. R. *et al.* Interfacial nanobubbles are leaky: Permeability of the gas/water interface. *ACS Nano* **8**, 6193–6201 (2014).

100. Qian, J., Craig, V. S. J. & Jehannin, M. Long-Term Stability of Surface Nanobubbles in Undersaturated Aqueous Solution. *Langmuir* **35**, 718–728 (2019).

101. Zhang, X. H., Quinn, A. & Ducker, W. A. Nanobubbles at the interface between water and a hydrophobic solid. *Langmuir* **24**, 4756–4764 (2008).

102. Zhang, X. H. *et al.* Detection of novel gaseous states at the highly oriented pyrolytic graphite-water interface. *Langmuir* **23**, 1778–1783 (2007).

103. Hirokawa, S. *et al.* Nanoscale Bubble Dynamics Induced by Damage of Graphene Liquid Cells. *ACS Omega* **5**, 11180–11185 (2020).

104. Tomo, Y. *et al.* Superstable Ultrathin Water Film Confined in a Hydrophilized Carbon Nanotube. *Nano Lett.* **18**, 1869–1874 (2018).

105. Ball, P. How to keep dry in water. *Nature* **423**, 25–26 (2003).

106. Singh, S., Houston, J., Van Swol, F. & Brinker, C. J. Superhydrophobicity: Drying transition of confined water. *Nature* **442**, 526 (2006).

107. Tyrrell, J. W. G. & Attard, P. Images of nanobubbles on hydrophobic surfaces and their interactions. *Phys. Rev. Lett.* **87**, 176104 (2001).

108. Attard, P., Moody, M. P. & Tyrrell, J. W. G. Nanobubbles: The big picture. *Phys. A Stat. Mech. its Appl.* **314**, 696–705 (2002).

109. Liu, H. & Cao, G. Effectiveness of the Young-Laplace equation at nanoscale. *Sci. Rep.* **6**, 1–10 (2016).

110. Craig, V. S. J. Very small bubbles at surfaces - The nanobubble puzzle. *Soft Matter* **7**, 40–48 (2011).

111. Jadhav, A. J. & Barigou, M. Bulk Nanobubbles or Not Nanobubbles: That is the Question. *Langmuir* **36**, 1699–1708 (2020).

112. Su, X., Wu, J. & Hinds, B. J. Nanoscale Bubble Valves on MWCNT Membranes for Chemical Energy Storage. *Adv. Mater. Interfaces* **2**, 1500102 (2015).

113. Hu, X. *et al.* Enhanced Peltier Effect in Wrinkled Graphene Constriction by Nano-Bubble Engineering. *Small* **16**, 1907170 (2020).

114. Zou, J. *et al.* Surface Nanobubbles Nucleate Liquid Boiling. *Langmuir* **34**, 14096–14101 (2018).

115. Lu, Y. Drag reduction by nanobubble clusters as affected by surface wettability and flow velocity: Molecular dynamics simulation. *Tribol. Int.* **137**, 267–273 (2019).

116. Fang, C. K., Ko, H. C., Yang, C. W., Lu, Y. H. & Hwang, I. S. Nucleation processes of nanobubbles at a solid/water interface. *Sci. Rep.* **6**, 1–10 (2016).

117. An, H., Tan, B. H., Zeng, Q. & Ohl, C. D. Stability of Nanobubbles Formed at the Interface between Cold Water and Hot Highly Oriented Pyrolytic Graphite. *Langmuir* **32**, 11212–11220 (2016).

118. Hain, N., Handschuh-Wang, S., Wesner, D., Druzhinin, S. I. & Schönherr, H. Multimodal microscopy-based identification of surface nanobubbles. *J. Colloid Interface Sci.* **547**, 162–170 (2019).

119. Bhushan, B., Pan, Y. & Daniels, S. AFM characterization of nanobubble formation and slip condition in oxygenated and electrokinetically altered fluids. *J. Colloid Interface Sci.* **392**, 105–116 (2013).

120. Dyett, B. P. & Zhang, X. Accelerated Formation of H2 Nanobubbles from a Surface Nanodroplet Reaction. *ACS Nano* **14**, 10944–10953 (2020).

121. Nag, S., Tomo, Y., Takahashi, K. & Kohno, M. Mechanistic Insights into Nanobubble Merging Studied Using in Situ Liquid-Phase Electron Microscopy. *Langmuir* **37**, 874–881 (2021).

122. Teshima, H., Nishiyama, T. & Takahashi, K. Nanoscale pinning effect evaluated from deformed nanobubbles. *J. Chem. Phys.* **146**, 014708 (2017).

123. Tortora, M. *et al.* The interplay among gas, liquid and solid interactions determines the stability of surface nanobubbles. *Nanoscale* **12**, 22698–22709 (2020).

124. Tan, B. H., An, H. & Ohl, C. D. Surface Nanobubbles Are Stabilized by Hydrophobic Attraction. *Phys. Rev. Lett.* **120**, 164502 (2018).

125. Guo, Z., Liu, Y., Xiao, Q. & Zhang, X. Hidden Nanobubbles in Undersaturated Liquids. *Langmuir* **32**, 11328–11334 (2016).

126. Guo, Z., Wang, X. & Zhang, X. Stability of Surface Nanobubbles without Contact Line Pinning. *Langmuir* (2019) doi:10.1021/acs.langmuir.9b00772.

127. Bull, D. S. *et al.* Contact Line Pinning Is Not Required for Nanobubble Stability on Copolymer Brushes. *J. Phys. Chem. Lett.* **9**, 4239–4244 (2018).

128. Meegoda, J. N., Hewage, S. A. & Batagoda, J. H. Application of the Diffused Double Layer Theory to Nanobubbles. *Langmuir* **35**, 12100–12112 (2019).

129. Tan, B. H., An, H. & Ohl, C. D. How Bulk Nanobubbles Might Survive. *Phys. Rev. Lett.* **124**, 134503 (2020).

130. Nirmalkar, N., Pacek, A. W. & Barigou, M. Interpreting the interfacial and colloidal stability of bulk nanobubbles. *Soft Matter* **14**, 9643–9656 (2018).

131. Carambassis, A., Jonker, L. C., Attard, P. & Rutland, M. W. Forces Measured between Hydrophobic Surfaces due to a Submicroscopic Bridging Bubble. *Phys. Rev. Lett.* **80**, 5357–5360 (1998).

132. Bunkin, N. F. *et al.* Formation and Dynamics of Ion-Stabilized Gas Nanobubble Phase in the Bulk of Aqueous NaCl Solutions. *J. Phys. Chem. B* **120**, 1291–1303 (2016).

133. Israelachvili, J. N. *Intermolecular and Surface Forces*. (Elsevier Inc., 2011). doi:10.1016/C2011-0-05119-0.

134. Poseidon Select : TEM Liquid Microscopy Cell. https://www.protochips.com/products/poseidon-select/.

135. Wu, H. *et al.* Mapping and Controlling Liquid Layer Thickness in Liquid-Phase (Scanning) Transmission Electron Microscopy. *Small Methods* **5**, 2001287 (2021).

136. Lu, J., Aabdin, Z., Loh, N. D., Bhattacharya, D. & Mirsaidov, U. Nanoparticle Dynamics in a Nanodroplet. *Nano Lett.* **14**, 2111–2115 (2014).

137. Schindelin, J. *et al.* Fiji: An open-source platform for biological-image analysis. *Nat. Methods* **9**, 676–682 (2012).

138. Grogan, J. M., Schneider, N. M., Ross, F. M. & Bau, H. H. Bubble and pattern formation in liquid induced by an electron beam. *Nano Lett.* **14**, 359–364 (2014).

139. Liu, Y. & Zhang, X. A unified mechanism for the stability of surface nanobubbles: Contact line pinning and supersaturation. *J. Chem. Phys.* **141**, 134702 (2014).

140. Teshima, H., Takata, Y. & Takahashi, K. Adsorbed gas layers limit the mobility of micropancakes. *Appl. Phys. Lett.* **115**, 071603 (2019).

141. Beattie, J. K., Djerdjev, A. M. & Warr, G. G. The surface of neat water is basic. *Faraday Discuss.* **141**, 31–39 (2008).

142. Takahashi, M., Chiba, K. & Li, P. Free-radical generation from collapsing microbubbles in the absence of a dynamic stimulus. *J. Phys. Chem. B* **111**, 1343–1347 (2007).

143. Reerink, H. & Overbeek, J. T. G. The rate of coagulation as a measure of the stability of silver iodide sols. *Discuss. Faraday Soc.* **18**, 74–84 (1954).

144. Fricke, G., Carpenter, R. & Battino, R. Effect of Various Gases on the pH of Water. *J. Phys. Chem.* **77**, 826–828 (1973).

145. Kowacz, M. & Pollack, G. H. Moving Water Droplets: The Role of Atmospheric CO2 and Incident Radiant Energy in Charge Separation at the Air–Water Interface. *J. Phys. Chem. B* **123**, 11003–11013 (2019).

146. Brotchie, A. *et al.* Acoustic bubble sizes, coalescence, and sonochemical activity in aqueous electrolyte solutions saturated with different gases. *Langmuir* **26**, 12690–12695 (2010).

147. Lide, D. R. & Kehiaian, H. V. *CRC Handbook of Thermophysical and Thermochemical Data*. (CRC Press, 2020). doi:10.1201/9781003067719.

148. Buffle, J., Zhang, Z. & Startchev, K. Metal flux and dynamic speciation at (Bio)interfaces. Part I: Critical evaluation and compilation of physicochemical parameters for complexes with simple ligands and fulvic/humic substances. *Environmental Science and Technology* vol. 41 7609–7620 (2007).

149. Lu, Y. H., Yang, C. W., Fang, C. K., Ko, H. C. & Hwang, I. S. Interface-induced ordering of gas molecules confined in a small space. *Sci. Rep.* **4**, 1–8 (2014).

150. Maheshwari, S., Van Der Hoef, M., Rodrĺguez Rodrĺguez, J. & Lohse, D. Leakiness of Pinned Neighboring Surface Nanobubbles Induced by Strong Gas-Surface Interaction. *ACS Nano* **12**, 2603–2609 (2018).

151. Chesters, A. K. & Hofman, G. Bubble coalescence in pure liquids. *Mech. Phys. Bubbles Liq.* 353–361 (1982) doi:10.1007/978-94-009-7532-3_33.

152. Katsir, Y. & Marmur, A. Rate of Bubble Coalescence following Quasi-Static Approach: Screening and Neutralization of the Electric Double Layer. *Sci. Rep.* **4**, 1–7 (2014).

153. Munro, J. P., Anthony, C. R., Basaran, O. A. & Lister, J. R. Thin-sheet flow between coalescing bubbles. *J. Fluid Mech.* **773**, 3 (2015).

154. Dees, D. W. & Tobias, C. W. Mass Transfer at Gas Evolving Surfaces: A Microscopic Study. *J. Electrochem. Soc.* **134**, 1702 (1987).

155. Stover, R. L., Tobias, C. W. & Denn, M. M. Bubble coalescence dynamics. *AIChE J.* **43**, 2385–2392 (1997).

156. Somorjai, G. A. & Li, Y. *Introduction to Surface Chemistry and Catalysis*. (Wiley, 2010).

157. Verhaart, H. F. A., de Jonge, R. M. & van Stralen, S. J. D. Growth rate of a gas bubble during electrolysis in supersaturated liquid. *Int. J. Heat Mass Transf.* **23**, 293–299 (1980).

158. Zhang, Z., Liu, W. & Free, M. L. Phase-Field Modeling and Simulation of Gas Bubble Coalescence and Detachment in a Gas-Liquid Two-Phase Electrochemical System. *J. Electrochem. Soc.* **167**, 013532 (2019).

159. Deng, J. *et al.* Review on effect of two-phase interface morphology evolution on flow and heat transfer characteristics in confined channel. *Heat Mass Transf. 2020 571* **57**, 13–39 (2020).

160. Takatoshi, T. *et al.* The Coalescence Mechanism of Multiple Slug Bubbles. *J. Nucl. Sci. Technol.* **36**, 671–682 (1999).

161. Serres, M., Maison, T., Philippe, R. & Vidal, V. A phenomenological model for bubble coalescence in confined highly porous media. *Int. J. Multiph. Flow* **105**, 134–141 (2018).

162. Chen, T. & Chung, J. N. Heat-Transfer Effects of Coalescence of Bubbles from Various Site Distributions. in *Mathematical, Physical and Engineering Sciences* 2497–2527 (Royal Society, 2003).

163. Soto, Á. M., Maddalena, T., Fraters, A., Meer, D. van der & Lohse, D. Coalescence of diffusively growing gas bubbles. *J. Fluid Mech.* **846**, 143–165 (2018).

164. Peercy, P. S. The drive to miniaturization. *Nature* **406**, 1023–1026 (2000).

165. Bocquet, L. & Tabeling, P. Physics and technological aspects of nanofluidics. *Lab Chip* **14**, 3143–3158 (2014).

166. Xie, L., Cui, X., Gong, L., Chen, J. & Zeng, H. Recent Advances in the Quantification and Modulation of Hydrophobic Interactions for Interfacial Applications. *Langmuir* **36**, 2985–3003 (2020).

167. Nazari, M. *et al.* Surface Tension Nanogates for Controlled Ion Transport. *ACS Appl. Nano Mater.* **3**, 6979–6986 (2020).

168. Yan, M. *et al.* Wetting state transition of a liquid gallium drop at the nanoscale. *Phys. Chem. Chem. Phys.* **22**, 11809–11816 (2020).

169. Bhushan, B., Wang, Y. & Maali, A. Coalescence and movement of nanobubbles studied with tapping mode AFM andtip–bubble interaction analysis. *J. Phys. Condens. Matter* **20**, 485004 (2008).

170. Liu, X., Deng, Y. D., Li, Z. & Su, C. Q. Performance analysis of a waste heat recovery thermoelectric generation system for automotive application. *Energy Convers. Manag.* **90**, 121–127 (2015).

171. Chan, C. U., Arora, M. & Ohl, C.-D. Coalescence, Growth, and Stability of Surface-

Attached Nanobubbles. *Langmuir* **31**, 7041–7046 (2015).

172. Williams, D. B. & Carter, C. B. *Transmission Electron Microscopy-A Textbook for Materials Science*. (Springer US, 2009). doi:10.1007/978-0-387-76501-3.

173. Nečas, D. & Klapetek, P. Gwyddion: An open-source software for SPM data analysis. *Cent. Eur. J. Phys.* **10**, 181–188 (2012).

174. Bowers, P. G., Hofstetter, C., Letter, C. R. & Toomey, R. T. Supersaturation limit for homogeneous nucleation of oxygen bubbles in water at elevated pressure: 'Superhenry's law'. *J. Phys. Chem.* **99**, 9632–9637 (1995).

175. Hill, T. L. *An Introduction to Statistical Thermodynamics*. (Dover Publications, 1986).

176. Guermeur, R., Biquard, F. & Jacolin, C. Density profiles and surface tension of spherical interfaces. Numerical results for nitrogen drops and bubbles. *J. Chem. Phys.* **82**, 2040–2051 (1984).

177. Yang, C. W., Miyazawa, K., Fukuma, T., Miyata, K. & Hwang, I. S. Direct comparison between subnanometer hydration structures on hydrophilic and hydrophobic surfaces via three-dimensional scanning force microscopy. *Phys. Chem. Chem. Phys.* **20**, 23522–23527 (2018).

178. Teshima, H., Li, Q. Y., Takata, Y. & Takahashi, K. Gas molecules sandwiched in hydration layers at graphite/water interfaces. *Phys. Chem. Chem. Phys.* **22**, 13629–13636 (2020).

179. Dammer, S. M. & Lohse, D. Gas enrichment at liquid-wall interfaces. *Phys. Rev. Lett.* **96**, 206101 (2006).

180. Wang, S. *et al.* Force Spectroscopy Revealed a High-Gas-Density State near the Graphite Substrate inside Surface Nanobubbles. *Langmuir* **35**, 2498–2505 (2019).

181. Pan, Y., He, B. & Wen, B. Effects of Surface Tension on the Stability of Surface Nanobubbles. *Front. Phys.* **0**, 494 (2021).

182. Li, C., Wang, S. P., Zhang, A. M. & Liu, Y. Dynamic behavior of two neighboring nanobubbles induced by various gas-liquid-solid interactions. *Phys. Rev. Fluids* **3**, 123604 (2018).

183. Yang, C. W., Lu, Y. H. & Hwang, I. S. Condensation of dissolved gas molecules at a hydrophobic/water interface. *Chinese J. Phys.* **51**, 174–186 (2013).

184. Luo, Q.-Q. & Yang, J.-M. Gas adsorption and accumulation on hydrophobic surfaces: Molecular dynamics simulations. *Chinese Phys. B* **24**, 096801 (2015).

185. Attard, P. Thermodynamic Stability of Nanobubbles. *arXiv:1503.04365 [physics.chem-ph]* (2015).

186. He, S. & Attard, P. Surface tension of a Lennard-Jones liquid under supersaturation. *Phys. Chem. Chem. Phys.* **7**, 2928–2935 (2005).

187. Wen, J., Dini, D., Hu, H. & Smith, E. R. Molecular droplets vs bubbles: Effect of curvature on surface tension and Tolman length. *Phys. Fluids* **33**, 072012 (2021).

188. Plesset, M. S. & Prosperetti, A. Bubble Dynamics and Cavitation. *Annu. Rev. Fluid Mech.* **9**, 141–185 (1977).

189. Ball, P. Feynman's fancy. *Royal Society of Chemistry: Chemistry World* 58–62 (2009).

190. Ito, T. & Okazaki, S. Pushing the limits of lithography. *Nature* **406**, 1027–1031 (2000).

191. Erik Edwards, B. W. *et al.* Precise Control over Molecular Dimensions of Block-

Copolymer Domains Using the Interfacial Energy of Chemically Nanopatterned Substrates. *Adv. Mater.* **16**, 1315–1319 (2004).

192. Peck, H., Gomez, I., Langer, S. & Brown, J. *Cymer Extreme Ultraviolet Light (EUV) Source (CRADA No. TC02195.0 Final Report)*. https://www.osti.gov/servlets/purl/1772694/ (2021) doi:10.2172/1772694.

193. Michalska, M. *et al.* Tuning antimicrobial properties of biomimetic nanopatterned surfaces. *Nanoscale* **10**, 6639–6650 (2018).

194. Onses, M. S. & Nealey, P. F. Tunable Assembly of Gold Nanoparticles on Nanopatterned Poly(ethylene glycol) Brushes. *Small* **9**, 4168–4174 (2013).

195. Lin, L. *et al.* Bubble-Pen Lithography. *Nano Lett.* **16**, 701–708 (2016).

196. Bangalore Rajeeva, B. *et al.* High-Resolution Bubble Printing of Quantum Dots. *ACS Appl. Mater. Interfaces* **9**, 16725–16733 (2017).

197. Fujii, S. *et al.* Fabrication and placement of a ring structure of nanoparticles by a laser-induced micronanobubble on a gold surface. *Langmuir* **27**, 8605–8610 (2011).

198. Zheng, Y. *et al.* Accumulating microparticles and direct-writing micropatterns using a continuous-wave laser-induced vapor bubble. *Lab Chip* **11**, 3816–3820 (2011).

199. Xie, Y. & Zhao, C. An optothermally generated surface bubble and its applications. *Nanoscale* **9**, 6622–6631 (2017).

200. Piner, R. D., Zhu, J., Xu, F., Hong, S. & Mirkin, C. A. 'Dip-pen' nanolithography. *Science (80-.).* **283**, 661–663 (1999).

201. Salaita, K., Wang, Y. & Mirkin, C. A. Applications of dip-pen nanolithography. *Nat. Nanotechnol.* **2**, 145–155 (2007).

202. Hewage, S. A., Kewalramani, J. & Meegoda, J. N. Stability of nanobubbles in different salts solutions. *Colloids Surfaces A Physicochem. Eng. Asp.* **609**, 125669 (2021).

Acknowledgement

First, I express my deepest gratitude to my thesis supervisor *Prof. Masamichi Kohno* for his guidance and support throughout my Ph.D. journey and for providing me with a healthy research-oriented atmosphere during my stay in his laboratory. He was very patient with me during my initial Ph.D. days and allowed me to be in the driver's seat of my Ph.D., for which I am extremely thankful to him. I also thank him for the numerous opportunities he introduced me to, which enabled me to maturate into an individualistic researcher. Thank you, *sensei*, for checking the span and timing of my steps that has helped me advance, both professionally and personally.

I would like to express my sincerest gratitude to *Prof. Koji Takahashi* for granting me access to the sublime facilities in his laboratory and for welcoming me to his prestigious CREST Research Team. Without his acceptance, this work would not have been possible. His encouragement and advice on my work has always motivated me to revamp my paths. I would also like to thank the members of his lab for their kind support throughout my tenure. Thank you, *sensei*, for allowing me the freedom to implement my experiments while working in your lab.

I am also thankful to my Doctoral committee members, *Prof. Koji Takahashi*, and *Prof. Shoji Mori*, for the time they have invested in evaluating my thesis and for their invaluable suggestions and comments.

I am thankful to *Dr. Yoko Tomo* and *Dr. Hideaki Teshima* for the support they have offered during my Ph.D., let it be professional or personal. They were very kind to always have time for discussions which helped me contemplate better on my work. Special thanks to *Mr. Tatsuya Ikuta*, the technical expert, for providing the necessary training for equipment use and for his support in any equipment-related issues. I am also grateful to *Mr. Sota Hirokawa* for always lending his hands for any help sought in experimental planning. I enjoyed our general discussions on the future of *nano-fluidics* and how we see this field converging with the industry in the coming years. Also, thank you so much for the translation of Conclusions section into the Japanese language.

I would also like to thank the research collaborators in the CREST Team, especially, *Prof. Yasutaka Yamaguchi* (Osaka Univ.), *Prof. Hiroki Ago*, *Dr. Qin-Yi Li*, *Dr. Pablo Solís-Fernández* (Kyushu Univ.) and *Dr. Takeshi Omori* (Osaka City Univ.) for their valuable inputs during our collaborative meetings.

I am grateful to my co-workers, especially *Sota Hirokawa, Yuzen Masame*, *Kuan-Ting Chen*, *Jinhan Hu,* and *Dawei Li,* who enriched my work life. I had a lot of fun while working with these guys. A big thanks to all present and already graduated lab-mates and technical staff for being very supportive of me. I would like to express my gratitude towards the laboratory's administrative staff: *Ms. Mikae Yamashita* and *Ms. Tomoko Kotake*, for their help in handling all the administrative affairs for me. I thank *Ms. Yasura Oiwa* and other administrative staff members of the school office and student's affair office, for support they have given me in my academic affairs.

Prior to my doctoral studies, lots of individuals have contributed to my development, both at the academic and personal level, and I would like to express my sincerest gratitude to all of them. I would like to thank my teachers back in India: my primary and senior schoolteachers, and my professors during my undergraduate and master's courses. *Prof. Anoop Kumar* from NIT Hamirpur taught me my first Fluid Mechanics course, from where I developed an interest in the Thermal-Fluid aspect of engineering. *Prof. Somesh Sharma*, my undergrad supervisor at NIT Hamirpur, introduced me to the field of engineering research. *Prof. Atul Dhar* from IIT Mandi played a huge role in grooming me as a young researcher and allowing me to implement my ideas and philosophy, in experiments as well as in writing, which helped me to bud into a young researcher. Special thanks and gratitude to *Mr. Navneet Sharma* for his support and encouragement through various journeys of my life. I am also thankful to *Dr. Harish Sivasankaran* (Univ. of Tokyo) for introducing me to my present workplace and for his steady guidance on academic life in Japan. I am thankful to my previous comrades and soon-to-be PhDs: *Hemant Thakur, Priybrat Sharma*, and *Sharey Deep Guleria*, who all, despite their busy schedules, never forget to ping me occasionally and continue to discuss science, technology, policies, and politics.

It was not easy being away from my loved ones, stuck in the pandemic. I am grateful to my friends and family for being my constant and sharing so much love over phone calls.

My friends, who have always been there in all the fun and rough times: *Aditya, Nalin, Nitin, Sukrit* and *Yash*; thank you for the phone calls and conversations we continue to have despite being busy in our lives and for recollecting the memories we have made together in our life. I am thankful to *Divyesh*, my flat mate in Japan, for his companionship, memories and for being my family in Japan. Special thanks to *Dakshita, Punit* and *Reetica* for checking on me from time to time and for some great conversations.

Neha, thank you for being that person with whom I could share all my rough and happy patches. Without your round-the-clock (*quite literally*) support and motivation, this would have been very so much difficult. Thank you for being a huge constant in my life and for providing sunshine to my gloomy days.

Finally, I would like to thank my parents, my grandparents, and my maternal and paternal family for their unconditional love and care. Among the numerous qualities I inherited from my parents, the most important was perseverance, to continue towards the goal with steadiness and patience, no matter how adverse the path may be. All these learnings have helped me to progress in my journey. I thank them for providing me with the best nest I could ever imagine growing in and for teaching me to fly fearlessly. This doctoral thesis is dedicated to my mother and father, *Rita* and *Anil Nag*.

I am thankful to the Japanese Society for the Promotion of Science (JSPS) KAKENHI grant number JP20J13061 and the Core Research for Evolutional Science and Technology project of the Japan Science and Technology Agency (JST-CREST) grant number JPMJCR18I1 for providing generous financial assistance to carry out this work. I am also thankful to the Japanese Society for the Promotion of Science (JSPS) DC2 Research Fellowship and the Japanese Government Scholarship (MEXT) for their financial support towards my living expenses throughout my research and doctoral studies.

It is impossible to put in words the efforts of all the people who have helped me reach here in their personal capacity. I sincerely apologize if I missed to acknowledged someone here.

Sarthak Nag
2022/01/12